Phantom Validation and Beam Line Characterization for Boron Neutron Capture Synovectomy Studies at McMaster University

Phantom Validation and Beam Line Characterization for Boron Neutron Capture Synovectomy Studies at McMaster University

By

Victor Kreft, B.Sc. (Hons.)

A Thesis

Submitted to the School of Graduate Studies

in Partial Fulfillment of the Requirements

for the Degree

Master of Science

McMaster University

MASTER OF SCIENCE (2005) McMaster University

(Medical Physics) Hamilton, Ontario

TITLE: **Phantom Validation and Beam Line Characterization for Boron Neutron Capture Synovectomy Studies at McMaster University**

AUTHOR: Victor A. Kreft, B.Sc. (Hons.)
(McMaster University)

SUPERVISOR: Dr. Fiona E. McNeill

NUMBER OF PAGES: xi, 91

Abstract

Rheumatoid arthritis is characterized by severe inflammation of the synovial tissue in the joint, which causes pain and degradation of the bone. The novel treatment boron neutron capture synovectomy (BNCS) utilizes the $^{10}B(n,\alpha)^{7}Li$ nuclear reaction to ablate the synovial tissue as an attempt to control these effects. The typical procedure involves intra-articular injection of a boronated compound followed by irradiation of the joint with a thermalized neutron beam. An anthropomorphic knee phantom has been designed and manufactured in a manner to display similar moderating and reactive properties to human soft tissue and bone. The intended use of such a phantom is the determination of RBE values of boron-compounds on several human cell types. Beam line characterization has been performed on the 3 MV KN single-ended accelerator at McMaster University using MCNP5. Testing was accomplished for neutron spectra produced by 2.00, 2.15, and 2.25 MeV protons on a thick lithium target. The maximum thermal flux through the interior cavity of the phantom was attained for moderator thicknesses of 3.25, 3.25, and 3.5 cm of high-density polyethylene (HDPE) at 2.00, 2.15, and 2.25 MeV, respectively, via MCNP5 for a phantom position 45° relative to the incident proton beam. Experimentally determined thermal flux maxima occurred using 1.75, 1.75 and 2.0 cm of HDPE for the corresponding energies. Causes for discrepancies were cited as phantom material inconsistencies, as well as possible errors in the analytical compilation of the MCNP5 source cards for the $^{7}Li(p,n)^{7}Be$ reaction. Experimentally, selecting a proton energy of 2.25 MeV showed little advantageous characteristics over 2.15 MeV. It is concluded that a Monte Carlo based code with charged particle transport capabilities may be desirable for further neutron dosimetry and standardized materials should be used whenever possible for manufacturing a "neutron phantom".

Acknowledgements

I wish to express my sincere thanks to my supervisor Dr. Fiona E. McNeill for her advice and guidance throughout this project. Her ability to listen, encourage, and envision are among but a few of her qualities to which I aspire. Thank you for your trust and faith in me as a student, and to the opportunities you have opened up for me. I look forward to working under your tutelage in my future studies.

I am grateful to the members of my supervisory committee, Dr. Joanne O'Meara, Dr. John Valliant, and Dr. Doug Boreham, whose insight into the multifaceted world of physics, chemistry, and biology that BNCS is, has been invaluable.

I would like to thank Dr. Soo Hyun Byun for his many hours of help both with undergoing my experiments and with his guidance of the world of MCNP. His experience and knowledge are true assets.

My thanks are also extended to Jason Falladown and Scott McMaster for there operation of the KN accelerator, John Cave for the machining of the phantom, Dr. Alice Pidruczny for her PGNAA verification of the copper foils, and Dr. Colin Webber for the use of the pQCT.

I have become well acquainted with many of the professors, staff, and fellow graduate students over the years I have been at McMaster. Thank you Ryan for your many years of leadership amongst us. Thank you all for your warmth and enthusiasm that make McIARS and the Medical Physics Department a wonderful place to work.

My heart goes out to the love of my life, Carolina. You have been there through it all; the good, the bad, and the ugly. I cherish your caring and compassion, and hope that I can show you even a tiny fragment of the abundance of love that I receive from you in my lifetime. I look forward to sharing my life with you as my wife. I love you, Carito.

Finally I wish to thank my parents for the years of love and trust invested in me. They have been there since the beginning, encouraging me to strive forward in my life. Words cannot express my gratitude for everything they have given me. This work is dedicated to them. Kocham was.

Table of Contents

List of Figures and Tables

Chapter 1. Introduction

1.1 Rheumatoid Arthritis: Epidemiology and Pathology

Rheumatoid arthritis (RA) is a chronic inflammatory disease which affects roughly 1% of the world's population.[1,2] Although its distribution is relatively uniform among populations, some exceptions exist. It affects women 2.5 times more frequently than men, is higher in prevalence among certain Native American Indian tribes, and has lower prevalence among certain tribes in Africa. Monozygotic twins show concordance rates in the range of 30-50% when one twin is positive for RA.[1,2] This is considerably higher than the rates for dizygotic twins (2-4%), which suggests a strong genetic susceptibility to the disease. However, given that the concordance is not 100% for monozygotic twins suggests an environmental component that is as of yet not understood. Although RA can affect patients of any age it generally affects those patients between 40 and 70 years of age. [1,2]

Despite years of thorough research, studies have failed to identify a root cause of RA.[1,3,4] It is generally accepted that the disease initiates via antigenic stimulation of CD4+ helper T cells. A strong correlation has been made between RA patients and the presence of HLA-DR4 class II major-histocompatibility-complex (MHC) antigens. The MHC molecules bind to the specific antigenic peptides and present the antigen to CD4+ helper T cells which can initiate immunologic response.[1,3,4] Although the search for the instigator of disease has focused on bacteria, viruses, and proteins that could be the source of the specific antigen, a culprit has yet to be identified.[1,3,4] Another possible cause for disease is hypothesized to be autoantigens such as heat-shock proteins and proteoglycans. Animal studies have shown that a variety of proteins can induce rheumatoid-like inflammatory responses when treated with these proteins.[1]

Rheumatoid arthritis is characterized by intense inflammatory arthritis of the diarthrodial (moveable) joints. Joint swelling is accompanied by pain and stiffness. Rapid-onset and prolonged joint destruction ultimately lead to deformity and loss of function of the hands and feet, and immobilization via arthritis of the knees, hips, wrists, and elbows. Subluxation of the cervical spine can contribute to immobilization, pain, and numbness. Extra-articular symptoms include rheumatoid nodules on bony prominences, pressure points, and tendon sheaths. Rheumatoid nodules can be moveable or fixed to tendons and bones. Compression neuropathy such as carpal and tarsal tunnel syndromes characterized by numbness of the hands, fingers, toes, and feet are typical. Pleuropulmonary disease is common in RA patients, which ranges from mild fibrosis to progressive interstitial lung disease. Systemic rheumatoid vasculitis, characterized by nail-hole infarcts, is among the most dreaded complications. Mortality rates of RA patients are higher and occur earlier than for the general population, although causes of death associated with RA are more or less the same as those of the general population.[1,2]

The articular joints are composed of several tissues including the synovium, muscles, bones, articular cartilage, ligaments, tendons, and subchondral bone. The joint itself has two compartments, the joint capsule and the joint cavity. The joint capsule is composed of largely fibrinogenous material that connects the two separate bones that meet at the joint. The joint capsule, along with the associated ligaments, is responsible for limiting the range of movement of the joint. The muscles attach via tendons to the respective bones of the joint. The joint cavity separates the two bones and is filled with a small amount of viscous emollient called synovial fluid. The ends of the two bones are covered by cartilage, which is intimate with the synovial fluid. The primary purpose of the synovial fluid is to permit smooth articulation of the bones, as well as provide nutrients to the articular cartilage and shock absorption. The tissue between the joint capsule and the cavity is called the synovium. The synovium itself is divided into three components: the synovial (intimal) lining, the subintimal stroma, and the vasculature. The synovial lining is composed of macrophage-like type A synoviocytes and fibroblast-like

type B synoviocytes. The synovial lining in normal articulating joints is generally 1 to 3 cells deep. Although the functions of the two cell types overlap, it is generally recognized that type A synoviocytes are phagocytic and provide a means for clearing of particulates from the synovial fluid. Type B synoviocytes produce hyaluronic acid, extracellular-matrix proteins, and lubricin, among other products. Hyaluronic acid and lubricin are critical components of the synovial fluid that enable minimal friction during articulation of the cartilaginous surfaces. Beneath the synovial lining lies the subintimal stroma, which contains a various array of fibroblasts, lymphocytes, adipocytes, and blood vessels. The subintimal stroma becomes increasingly fibrous as depth from the cavity increases until it becomes indistinguishable from the joint capsule. The vasculature of the synovium provides for vital nutrients and gas exchange throughout the lining and stroma. The vasculature approaches closely the cavity fluid in many areas allowing for nutrition and gas exchange of the synovial fluid. This is vital in that the articular cartilage lacks its own blood supply.[1,3,5]

In patients with rheumatoid arthritis, the joint tissues become chronically inflamed. The synovium exhibits extreme hyperplasia (cell proliferation). The synovial lining increases in thickness up to 15 cells in depth. As mentioned above, the CD4+ T cells initiate immunologic response once activated via a specific antigen. The response is rapid and strong. Monocytes and macrophages are stimulated to produce the cytokines (messenger proteins) interleukin-1 (IL1), interleukin-6 (IL6), and tumor-necrosis-factor-α (TNF-α) via CD4+ T cells. These cytokines in turn stimulate various immunologic responses. The result is a large influx of leukocytes. The synovial linings cells are induced to proliferate. The subintimal stroma is dramatically altered containing T cells, B cells, macrophages, and plasma cells. CD4+ T cells stimulate osteoclastogenesis. TNF-α and IL1 also stimulate synovial fibroblasts, osteoclasts, and chondrocytes to release matrix metalloproteinases. Matrix metalloproteinases act as powerful enzymes that degrade cartilage and bone. Leukocytes eventually release their degradative enzymes into the synovial fluid. Angiogenesis is stimulated via a variety of lymphocytes, macrophages,

and synoviocytes. The increase in vasculation results in an increased presence of macrophages and T-cells. The end result is the production of pannus, a highly erosive tissue composed of mononuclear cells and synovial fibroblasts. The evolution of pannus from the early stages of RA through to the later stages results in joint destruction and remodeling of the joint characterized by deformation, immobilization, and pain in the afflicted joints.[1,2,4,5]

1.2 Rheumatoid Arthritis: Therapy

Although no cure for rheumatoid arthritis exists at present, advances in molecular biology have contributed greatly to new therapeutic agents. The RA treatment pyramid generally begins with non-steroidal anti-inflammatory drugs (NSAIDs). These drugs include aspirin (acetyl salicylic acid), ibuprofen, naproxen, and celexocib. Prostaglandins, hormone-like fatty acids that help to mediate the inflammatory response, are produced via cyclooxygenase enzymes, COX-1 and COX-2. These enzymes are induced by the cytokines TNF-α and IL1. NSAIDs act by inhibiting the role of both COX-1 and COX-2 or COX-2 alone, thereby reducing the inflammatory response.[1] Prescribed doses of these drugs are considerably higher than for analgesic purposes. Side effects include gastrointestinal toxicity, inhibited platelet function, and kidney toxicity.[1]

Generally if the patient has not experienced reduced swelling and/or pain relief, or is showing aggressive joint erosion on radiograph, the next line of defense is disease-modifying antirheumatic drugs (DMARDs). Although the use of these drugs has been historically effective, the means by which their affectivity takes place is poorly understood.[2] The most common second-line agent is the folic acid inhibitor methotrexate.[1,2,3] The likely mechanism of action is via inhibition of IL1 production. This mechanism has been shown in animal testing.[1] Studies have shown that methotrexate improves RA symptoms clinically and radiographically and is considered the staple drug for RA.[1,2] Other long used DMARDs are gold salts including gold sodium thiomalate and

aurothioglucose. The antimalarial drug hydroxychloroquine is also a popular choice among physicians.[1] Side effects of these drugs include gastrointestinal toxicity, hepatotoxicity, allergic pneumonitis, leukopenia, thrombocytopenia, cataractogenesis, and blindness. Each drug has its own gamut of side effects and patients who are prescribed these drugs are under close physical monitoring, as well as blood and liver monitoring.[1,2] The average duration of an effective regimen of monotherapy is approximately 5 years, although some patients can find symptomatic relief for up to 10 years.[1,2] The latest trend by physicians is to prescribe a combined therapy of two or more DMARDs. The benefits are generally greater and the toxic effects of the drugs are reduced under this type of regimen. With the advent of standardized physical and radiographical benchmarking, such as the Disease Activity Score (DAS) in Europe and the American College of Rheumatology (ACR) response, physicians are better able to grade the clinical presentation of RA.[2] Since the awareness of the swiftness with which RA can destroy the synovium, articular cartilage, and bone, the trend among physicians is increasingly becoming to use DMARDs as the first line of defense.[1,2]

The past decade has seen the advent of biological response modifiers (BMRs). Etanercept is a cytokine-receptor protein that binds to TNF-α and TNF-β.[1,2,4] Infliximab is another BMR that binds strictly to TNF-α.[1,2,4] By reducing the specific cytokines that are expressed in the RA synovium, these drugs act to halt the inflammatory response. Etanercept is injected twice weekly and has a estimated yearly cost of $12000 USD.[2] Infliximab is administered at weeks 0, 2, 6, and at every 8 weeks and has an estimated cost of $9000 USD.[2] Neither of these two drugs is a cure for the disease and patients must be watched carefully for development of serious infection, dyspnea, and hypotension.[2] Studies have shown that therapeutic response is most successful when these drugs are combined with methotrexate.[1,2] Another group of drugs currently under investigation are cytokine-receptor blockers. Recombinant interleukin-1 receptor antagonist and interleukin-6 receptor antibodies both compete for receptor positioning against the cytokines IL1 and IL6.[4] The disadvantage of these drugs is the half-life in vivo, as well as

the necessity to overload the tissue in order to be effective at blocking the specific receptors.[4]

Once the use of NSAIDs and DMARDs has been exhausted by the patient the mode of treatment quickly escalates to powerful immunosuppressive agents. Azathioprine and leflunomide likely act as nucleic-acid metabolic inhibitors, while chlorumbucil and cyclophosphamide act as alkylating agents.[1,2] Side effects include renal and hepatotoxicity and increased risk of malignancy.[1] Corticosteroids are a powerful family of anti-inflammatory drugs related to the adrenal steroid hormone cortisol. Oral prednisone and intra-articular injection of tiaminoclone are two of a variety of glucocorticoids used in RA treatment. Corticosteroids function by blocking inflammatory mediators such as prostaglandins.[6] However, a side effect of this action is to reduce the ability of leukocytes to engage in normal function leaving the body exposed to rampant infection.[1,6]

The final line of treatment for RA symptoms is operative surgery of the joint. This is most often the option when all but one joint are responsive to drug therapy. Joint replacement, as well as synovial ablation via standard and arthroscopic surgeries, is the most frequently performed procedure.[1] Synovial ablation by intra-articular injection of beta emitting radiocolloids (such as colloids of Yttrium-90) has also been widely used throughout the world.[7,8,9] This method, however, has not been used greatly in the United States for concern over leakage of the radionuclide away from the synovial cavity.[5] Radio-safety issues are also of concern since a highly active aqueous solution of radionuclide must be transported and handled in order to attain significant ablation of the synovial tissue. Synovial ablation must often be re-performed every 2 to 5 years due to the re-emergence of arthritic symptoms in the treated joint.[5]

1.3 Boron Neutron Capture Synovectomy (BNCS)

One of the first papers to document a novel application of the $^{10}B(n,\alpha)^{7}Li$ nuclear reaction for synovectomy was that of Yanch et al. (1999) entitled, "Boron neutron capture synovectomy: Treatment of rheumatoid arthritis based on the $^{10}B(n,\alpha)^{7}Li$ nuclear reaction." [5] The idea for boron neutron capture synovectomy (BNCS) treatment arose from a novel therapy presently in clinical trials for glioblastoma multiforme, a class of high-grade brain tumours for which the normal prognosis is very poor.[5,11] Central to the role of this therapy is the high thermal neutron capture cross section of ^{10}B. When a ^{10}B atom captures a thermal neutron (one having energies comparable to thermal kinetic motion), the atom fissions, emitting two reaction products with high linear energy transfer (LET); a ^{7}Li atom and an alpha particle. Additionally, 94% of the time a 477 keV gamma ray is emitted concomitantly.[11] These high LET particles have a range of 12-13 μm,[11] on the order of cellular dimensions.[12] Particles with high LET have higher relative biological effectiveness (RBE) such that the biological damage is greater per unit physical dose than lower LET ionizing radiations such as X-rays. Thus, if the target cell, be it a cancerous cell or an RA synoviocyte, were to be bombarded with thermal neutrons in the presence of substantial quantities of ^{10}B, the effectiveness of apoptosis (programmed cell death) would be higher than for an equivalent physical dose from high energy photons. Moreover, if the ^{10}B can be loaded preferentially into the target cells via a boronated biochemical or antibody, so too can there be targeted cell killing, while delivering a minimal dose to surrounding healthy tissue.[11] The current limit to the success of this so called boron neutron capture therapy (BNCT) is the lack of effective drugs.[11] Of critical matter is the leakiness of the blood-brain barrier, which prevents targeted compounds from accumulating in target tissue.[11] The result is effective cell killing in the target with mutually high cell killing of healthy tissue. Although compounds have proved unsuccessful in BNCT, research suggests that large concentrations of ^{10}B can be loaded into the synovium, the likely target for BNCS.[5] The clear advantage in BNCS is the fact that the boronated compound can be injected directly into the intra-articular cavity. Thus,

BNCS could accomplish the same endpoint as radiation synovectomy described above. The advantage, however, is that the therapeutic compound has no radioactivity before or after irradiation, eliminating concerns over radioactive toxicity in the body and handling of a radiocolloid.

The fact that BNCT and BNCS have different target tissues also means that the two treatments have different neutron requirements. BNCT target tissues are several centimeters below the thick skull bone. Surrounding the tumour are several critical tissues including the skin, brain, eyes, occipital nerve, and cervical spinal chord. To ensure a high thermal neutron flux at the tumour tissue, the neutron energy is generally selected to be in the epithermal (slightly above thermal) range.[11] To avoid skin erythema (reddening) initial thermal neutrons must be filtered out using a compound containing an isotope such as ^{6}Li. Fast neutrons have very high RBE values and should also be reduced to a minimum. Thus, an optimal amount of moderation via compounds with large quantities of light nuclei, such as hydrogen or deuterium, reduce the fast neutron flux to useful epithermal energies.[11] The synovium, on the other hand, is located within 2 cm of the skin surface.[5] Therefore, moderation requirements differ for BNCS from those of BNCT. An increased thermal neutron component must be present in the neutron spectrum and, therefore, less moderation will be required. Various sources of neutrons have been investigated in the past several decades including reactor beam ports, charged particle accelerators, and ^{252}Cf sources.[11] Each source has its own unique neutron spectrum and, as such, has its own moderating and design requirements to optimize the thermal flux to the tissue of interest.

Despite the differences between BNCT and BNCS treatments, the physical dose components to be considered during dose planning are the same. Dose components that should be plotted separately on a treatment plan are: fast neutron dose, photon dose, thermal neutron dose, ^{10}B dose in target, ^{10}B dose in non-target, total target, and total non-target (for various critical healthy tissues).[11] Each component must be multiplied by

its associated RBE value. Photons arise from several interactions including source photons, beam line structure photons via capture or scattering, and in vivo capture reactions including oxygen, carbon, nitrogen, sodium, chlorine, and especially hydrogen. Additionally, protons arise from the nitrogen capture reaction $^{14}N(n,p)^{14}C$. [11] Therefore, a highly developed particle transport code such as Monte Carlo N-Particle (MCNP) [22] or GEANT [23] is required for tracking of dose components to accomplish accurate dosimetry.

1.4 Literature Review: Paper 1

In the Yanch et al. (1999)[5] paper listed above, the primary goal was to determine the potential of BNCS as a viable treatment option for rheumatoid arthritis. The preliminary study described was of ^{10}B uptake measurements ex vivo using a salt of the polyhedral closo boronate ion, $K_2B_{12}H_{12}$, available from Strem Chemical, Ipswich, MA. In order to perform these measurements synovial and cartilage tissue samples were obtained from RA patients undergoing synovectomy or joint replacement surgery. Samples were minced and incubated for at least 7 days. The samples were then incubated along with unenriched $K_2B_{12}H_{12}$ containing 1000 ppm ^{10}B for one hour. After the hour period samples were rinsed in saline and incubated in fresh medium for 0, 30, 60, and 120 min intervals. Samples were then rerinsed and tested for ^{10}B concentration in a prompt gamma neutron activation analysis (PGNAA) facility. After initial washout, synovial tissue samples that were not reincubated in fresh medium (i.e. 0 min) showed ^{10}B concentrations between 1000 and 2000 ppm. With reincubation in fresh medium results showed that 75% of the boron compound left the sample. Cartilage samples showed uptake levels between 210 and 140 ppm after 1 hour and 24 hours of incubation, respectively. These values are roughly 10% or less that of the synovial tissue, showing that cartilage uptake is favorable to a reduced $^{10}B(n,\alpha)^{7}Li$ dose component.

In vivo ^{10}B uptake was studied by injecting the $K_2B_{12}H_{12}$ compound into the knees of New Zealand rabbits. These rabbits had been previously made arthritic via antigen induction. The ^{10}B concentration chosen for the in vivo studies remained the same as for the ex vivo studies at 1000 ppm. Animals were sacrificed at 0.25, 1, 4, and 24 h intervals and samples of the synovium, synovial fluid, patella, patellar tendon, ligaments, cartilage, bone, and bone marrow were obtained. In addition samples of blood, urine, and several body organs were taken. ^{10}B uptake analysis was performed at the MIT PGNAA facility. Concentrations for the synovial boron decreased rapidly from 265-950 ppm after 15 min to 30-50 ppm 1 h after injection. Yanch et al. commented, however, that concentrations within the 15 min were more than sufficient to provide a therapeutic dose to the synovium.

Neutron beam optimization began by examining the ideal energy for BNCS. A symmetrical cylindrical phantom for Monte Carlo simulations was designed based on the knee, since the knee is the joint most often selected for synovial ablation. From magnetic resonance images of a human rheumatoid arthritic knee, the phantom diameter was selected to be 8.70 cm. Tissue thicknesses were designated from exterior to interior as follows: 1 cm for the skin and fat layer, 0.3 cm for the subsynovium, 0.15 cm for the synovial lining, 0.2 cm for the synovial fluid, 0.2 cm for the articular cartilage, and 5 cm for the bone. Two ratios were used to compare the optimal neutron energy for BNCS. Although dose to the synovium is to be maximized, tissues of concern are the skin dose and the bone dose. Dose effects to the skin are deterministic. The limiting dose to the skin was set as 800 cGy, the threshold for skin reddening. From radiation synovectomy data for beta emitters, Yanch et al. have estimated that a biological dose of 10000 RBE-cGy must be delivered to successfully ablate the synovial tissue. Thus the minimum synovium to skin dose was determined to be 12. It was cited that the International Commission on Radiological Protection considers the bone surface as a critical tissue and that the dose to it should be minimized. Radiation effects to the bone are stochastic and, therefore, the bone dose was to be maximized over the range. Assuming a synovial ^{10}B concentration of

1000 ppm, and a healthy tissue concentration of 1 ppm, all dose contributions to the tissues in the model phantom were accounted for including thermal neutron, fast neutron, initial and induced photon, and $^{10}B(n,\alpha)^{7}Li$ reaction product doses. Neutron, photon, and reaction fluxes were modified by fluence-to-dose conversion factors. Since RBE values do not exist for BNCS radiation components, values used in clinical trials of BNCT were used: 4.1 for ^{10}B reactions products, 4.0 for all neutrons, and 1.0 for all photons. Yanch et al. showed that the best synovium to skin and synovium to bone dose ratios were achieved with monoenergetic neutrons ranging from 0.025 eV to roughly 0.5 or 1.0 keV. The same optimal energy range was found when bone ^{10}B concentrations were increased to 10 ppm.

In addition to the knee phantom, a model was also created for the human finger. In this case the finger was embedded in a 2.2 cm thick slab of water to imitate the presence of the remaining fingers. The same cylindrical geometry was adopted for the finger as that of the knee with correspondingly smaller dimensions. With the two phantoms available for Monte Carlo simulations, Yanch et al. studied several accelerator beam-target reactions that would produce a favorable neutron spectrum to give similar results as those of the monoenergetic beams simulated above. Heavy water, D_2O, was selected as the thermalizing moderator to avoid additional photon induction via the $^{1}H(n,\gamma)^{2}H$ that arises in standard water. The length of the moderator was fixed at 30 cm with a fixed reflector configuration to investigate reflector materials. Graphite showed to give better therapeutic ratios and time characteristics over lead, $^{7}Li_2CO_3$, and D_2O, and was chosen for future research. The thickness of graphite was optimized to be 18 cm. Of the five different reactions available $^{7}Li(p,n)$, $^{9}Be(p,n)$, and $^{9}Be(d,n)$ beams were shown to be the most suitable for BNCS. $^{7}Li(p,n)$ showed the best dose ratio values at several ^{10}B concentrations in healthy tissues for a ^{10}B concentration of 1000 ppm in the synovium. $^{7}Li(p,n)$ also showed improved therapy times over the beryllium reactions with less moderation, for concentrations ranging from 500-2500 ppm in the synovium. Additionally, improved synovium to skin dose ratios were attained when using parallel

opposed beams versus a single beam. For the knee joint phantom, using the ^{7}Li(p,n) beam at 2.5 MeV with 15 cm of heavy water moderator, 10 cm of graphite back reflector, and an assumed 265 ppm ^{10}B synovium concentration, therapy time for parallel opposed beams was 26 min per mA. If the ^{10}B concentration in the synovium was increased to 950 ppm that time was decreased to 8.4 min per mA. With all variables the same the therapy times for the finger joint phantom were 13 min and 4 min for 265 ppm and 950 ppm ^{10}B synovium concentrations, respectively.

Although the ^{7}Li(p,n) reaction provided suitable therapeutic parameters, Yanch et al. cited the preference of beryllium as a target of choice due to favorable thermal, mechanical, and chemical properties. Between the two possible beryllium reactions the ^{7}Be(d,n) reaction was chosen over ^{7}Be(p,n) for its short therapy times and lower accelerator beam energy. It was concluded that BNCS showed promising physical characteristics to be a viable alternative treatment for RA patients. Further investigation into testing and optimization of boron compounds, the optimal treatment dose, and experimental testing in the animal model were listed as future considerations.

1.5 Literature Review: Paper 2

In the follow up to the publication outlined above, Gierga, Yanch, and Shefer (2000) published another paper entitled, "Development and construction of a neutron beam line for accelerator-based boron neutron capture synovectomy." [10] Studies for the human knee and human finger were performed with the same models as in their previous publication. A rabbit knee model was created with similar geometries to the human knee and finger but adjusted to the proper dimensions. RBE values were taken as 4.0, 3.8, and 1 for ^{10}B reaction products, neutrons, and photons, respectively. Charged particle reactions studied included ^{9}Be(p,n) at proton energies of 4.0 and 3.7 MeV, ^{9}Be(d,n) at deuteron energies of 2.6 and 1.5 MeV, and ^{7}Li(p,n) at proton energy 2.5 MeV. Heavy

water moderator lengths chosen were 23, 20, 15, 15, and 15 cm for the corresponding reaction-energy combinations listed. The D_2O geometry was selected as cylindrical with a diameter of 9 cm. The D_2O moderator was surrounded by 18 cm thick graphite reflector. In addition to moderator and target reflector optimization, Gierga et al. studied the effects of various materials and corresponding thicknesses for side and back reflectors for the MCNP models used. Using a 2.6 MeV $^{9}Be(d,n)$ neutron source, side and rear reflector graphite was found to be superior in terms of performance and cost over lead and beryllium. The dimensions of the rear reflector were shown to be optimal at 45 cm in the lateral direction with a thickness of 10 cm. The side reflector thickness was set by the limiting size of the knee phantom at 8.7 cm of graphite. The width of the reflector was set to 10 cm which was chosen based on the optimal rear reflector thickness. The height of the side reflectors was varied and found to show little improvement in treatment parameters at dimensions greater than 30 cm. Thus, 30 cm was chosen as the height. For a single beam the addition of a rear reflector showed therapy parameter improvements of a factor of 2, while adding side reflectors increased the parameters by a further 20-30%. The total improvement was a factor of 2-3 increase for a single beam while it was 1.5-2 for parallel opposed beams.

For the human knee with optimized beam line design, including rear and side reflectors, based on 1000 ppm synovial ^{10}B uptake, 1 ppm healthy tissue ^{10}B uptake, and a 1 mA current, the 2.5 MeV $^{7}Li(p,n)$ reaction showed the best therapy parameters of the reactions chosen. Therapy time for parallel opposed beam irradiations was 7 min. The skin dose was 129 RBE cGy, which was considerably lower than the limit chosen to be 800 cGy. The bone ratio was calculated to be 108. The next best therapy parameters of 10 min, 190 RBE cGy skin dose, and bone dose ratio of 79 were achieved using the 3.7 MeV $^{9}Be(p,n)$ reaction. In addition to these optimization studies, Gierga et al. examined the effect of a thermal neutron fliter, ^{10}B concentration in the synovium, and the overall whole body dose from an irradiation. A ^{6}Li thermal neutron filter of 0.02, 0.1, and 0.5 cm thickness was found not to be beneficial as these thermal neutrons are therapeutically

useful. ^{10}B concentration improved therapy time up to roughly the studied limit of 20000 ppm where it began to plateau. Gierga et al. cited that $K_2B_{12}H_{12}$ concentrations of up to 19000 ppm have been measured in vivo 30 minutes post-injection. The ^{10}B concentration threshold to achieve less than an 800 RBE-cGy skin dose was found to be 300-400 ppm in the synovium. The MCNP model of the beam line and phantom was used along with the anthropomorphic human body phantom based sources including MIRD [46] and the Visible Man Project [47] to determine the whole body dose. Without optimization, a 15 cm lithium carbonate shield was added from the upper leg to the upper torso. The leg not being treated was assumed to be positioned out of the beam vicinity. Using ICRP 60 methodologies for critical organs, the whole body dose for the 2.6 MeV $^{9}Be(d,n)$ reaction was 3.6 rem (36 mSv) based on a ^{10}B concentration of 1000 ppm in the synovium. This value decreased to 0.75 rem (7.5 mSv) if that concentration was increased to 19000 ppm. It was commented that 3.6 rem is less than the yearly dose limit for a radiation worker.

Finally, aside from the MCNP assessment studies, Gierga et al. described a method for experimental validation of the MCNP in-phantom dose rates using mixed field dosimetry in a simplified head water phantom used in BNCT studies. The technique involved using two ionization chambers, one tissue equivalent ion chamber (Far West IC-18) which was sensitive to fast neutrons and photons, while the other graphite ion chamber (Far West IC-18G) was sensitive to photons alone. In this manner the fast neutron and photon fluxes were separated and ascertained. In addition to the dual ionization technique, bare and cadmium covered ^{197}Au foils were used to determine the thermal flux. Cadmium has a high thermal neutron capture cross section. By determining the total neutron flux with and without cadmium, the thermal neutron flux was extrapolated. Experiments and simulations were performed using the 1.5 MeV $^{9}Be(d,n)$ reaction with a 22 cm heavy water moderator at a 26 μA current on target. Measurements were taken at depths ranging from 1 cm through 10 cm in the phantom. All radiation component fluxes were converted to dose values using fluence-to-kerma factors. Gierga et al. cited that the experimental depth dose curve agreed with MCNP simulations. The

values of the experimental dose were within the factor of 3 neutron yield range found in literature for the $^{9}Be(d,n)$ reaction.

Overall these two papers outlined that BNCS was a viable treatment for RA patients assuming $K_2B_{12}H_{12}$ could be used as a compound, and that a current on target of the order of milliamperes could be achieved for the neutron source reactions. Future research included increased testing of compounds, RBE value determination for such compounds, and improved validation in the animal model to determine a sufficient dose to ablate the synovial tissue.

Chapter 2. Phantom Design and Manufacture

2.1 Study Proposal

Despite the feasibility of BNCS shown by Yanch et al. (1999) and Gierga et al. (2000) as published, BNCS has not been adopted as a useable treatment for rheumatoid arthritis symptoms. Of primary concern has been the toxicity of the boron compound used in these studies.[13] Yanch et al. (1999) showed that 75% of the $K_2B_{12}H_{12}$ compound left the sample tissue within 30 minutes during ex vivo studies. While in vivo studies were carried out at ^{10}B concentrations of 1000 ppm, this represented an intra-articular injection of 5000 ppm elemental boron, since the natural abundance of ^{10}B is roughly 20%. The egression of compound within the first 15 minutes was from 5% up to 73.5%. To attain the optimal ^{10}B uptake level of 20000 ppm shown by Gierga et al. (2000) more than 100000 ppm elemental boron would have to be administered, a significant percentage of which would be washed out into the body within minutes. The $K_2B_{12}H_{12}$ compound, having acute health effects listed in the MSDS as "redness and pain in eyes, sore throat, twitching of facial muscles, convulsions, cyanosis, coma, and death" [14], was not a suitable boron compound for such a treatment.

Rather than using an inorganic boronated salt, Valliant et al. (2000) showed that an organically based corticosteroid-carborane ester could be synthesized.[15] Given that corticosteroids have been widely used and shown to accumulate in arthritic synovial cells, this compound could show promise for BNCS treatment.[15] However, the corticosteroid-carborane esters synthesized by Valliant et al. have since not been tested in or ex vivo. In addition to such in vivo and ex vivo studies, RBE value determination of such compounds must be performed. As stated in Chapter 1, Yanch et al. and Gierga et al. had assumed RBE values for the boron reaction products based on data available from

BNCT trials. However, given that RBE values can vary for tissue type as well as compound, the validity of these assumptions should be established.

Accelerator beam and reactor neutron source applications have been widely studied at the McMaster Institute for Applied Radiation Sciences (McIARS), McMaster University, Hamilton, Ontario, Canada.[15-21] Until recently, the sole accelerator source for neutron production has been the 3 MV Van de Graff type (KN) accelerator. Due to design and target constraints maximal current levels of this accelerator are restricted below 80 μA. This value is significantly lower than the therapeutic current proposed by Yanch et al. of 1 mA. Presently testing is underway on a newly installed high power tandem accelerator at McIARS, capable of currents up to 1 mA. With advancements in lithium target performance, studies at treatable current levels may be attained. The long term hope is to develop a functioning BNCS/BNCT treatment centre at McIARS. The purpose of this study was to perform initial experimental and simulation analysis at McIARS to prepare for RBE value determination and compound feasibility studies in vitro. These studies are to be performed using the corticosteroid-carborane esters developed by Valliant et al., along with several cell lines significant to rheumatoid arthritis. The development and manufacture of a phantom in which cell cultures could be irradiated at the KN accelerator is described below. Experimental and simulation comparative analysis for validating the phantom composition is performed in the chapters that follow.

2.2 Phantom Geometry

The goal in creating an anthropomorphic phantom was to design one that would show similar geometrical shape and dimensions of a life size leg. The leg was chosen for the same reasons that it was chosen by the MIT Laboratory for Accelerator Beam

Applications, namely the frequency with which knee joint synovectomy is performed, as well as the overall size and location of the leg relative to the rest of the body. Manufacturing a detailed phantom of the knee joint similar to that modeled in MCNP by Yanch et al. would be extremely difficult and was beyond the scope of the intended study. The idea was to utilize simple shapes that could be easily modeled in MCNP and create a contrasting material composition within the phantom. Geometrical definitions within MCNP are for the most part restricted to simple shapes such as cubes, rectangular boxes, and spheres. Intersections and unions of such shapes allow one to create sample cells of more intricate nature. Curvatures such as those that exist in the body can be created with complex computer coding but this too was beyond the scope of the present study, since the main purpose of study was to essentially create an irradiation cavity for cell cultures. The surroundings of the cavity were desired to resemble those of the synovial cavity of the knee joint, both in structure and composition. Cells can be cultured in several types and sizes of flasks, including sealable tubules, rectangular flaskettes with caps, and petri dishes. Since the cylindrical nature of the human synovial cavity was realized, and agreed with the model proposed by Yanch et al. (1999), the petri dish was selected as the flask of choice for further biological studies. The dimensions of the petri dish were initially chosen to be 60 mm in diameter with a height of 15 mm, which had nearly the diameter of the combination of bone, cartilage, and synovial fluid selected by Yanch et al.. However, after further investigation the close resemblance of a 35 mm diameter by 10 mm high petri dish to the actual synovial volume was established.[25-27] Despite the relatively small size of the petri dish, millions of cells can be cultured in a flask of this size that would provide a more than sufficient sample size for acceptable statistics during future biological testing.[27] Such petri dishes are widely available in sterile form from scientific product suppliers at a low cost. Although they lack an intrinsic cap, when sealed with lab wrap along the sides the lid provides a sterile environment which minimizes the possibility of cultural infection.

Once an overall simple cylindrical shape was chosen for the phantom, the tissues to be included were selected. Tissue types were divided into two categories according to density: soft tissue and boney tissue. Outside the articular joint capsule lie various layers of skin, fat, muscle, and blood and lymph vessels. All were categorized as soft tissue material. The joint capsule transcends into the cartilage, which is intimate with the cortical bone tissue of the adjacent bones. Since these tissues are radiographically denser than soft tissue they were categorized as boney tissue. As described in Chapter 1, the synovial cavity is intimate with the synovial lining. The synovial fluid has a density close to that of water and soft tissue, and therefore it, along with the synovial lining were also categorized as soft tissue. Thus, the phantom was to be composed of three compartments: soft tissue exterior to the bone, bone, and soft tissue within the synovial cavity. However, since the phantom was designed such that the synovial lining and synovial fluid were to be resembled by the cellular substrate within the petri dish, these were not to be modeled in the phantom itself. A diagram of the coronal cross section of an initial phantom design for which the petri dish size was 60 mm in diameter and 15 mm in height is shown in Fig. 1.

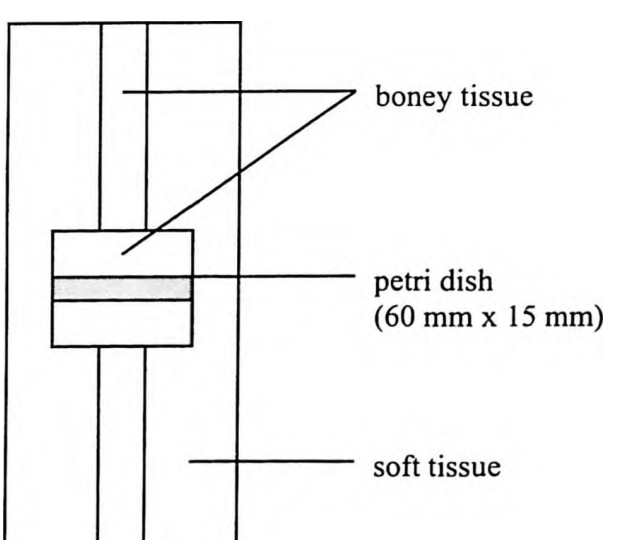

Figure 1 Coronal cross section of initial phantom design proposal.
N.B.: Diagram not to scale.

The design shown in Fig. 1 was modified to allow for a more realistically sized petri dish (35 mm diameter by 10 mm height) to represent the synovial cavity. This in turn resulted in a more realistic representation of the boney tissue which surrounds the synovial cavity. In reality, the lower human leg contains two long bones that attach to the knee joint, the tibia and the fibula. Thus, the fibula was added to the lower leg of the phantom design shown in Fig. 1.

The next step in the design process was to assign dimensions to the phantom tissues chosen. The "Report of the Task Group on Reference Man" ICRP Publication 23 is widely used by medical physicists to determine values of interest with respect to the composition, mass, and size of tissues, organs, and the overall body of the human species for physical purposes.[28] The title gives data pertaining to each tissue of the body separated largely by sex. Since rheumatoid arthritis is prevalent more frequently in women, it was decided that the phantom would take on dimensions based on data available for the female subject. Little information, however, was available for the dimensions of the bones and tissues of the leg. The circumference of the thigh as a percent of total body length was found to increase slowly with age in females beyond the age of 10 years.[28] The circumference of the thigh at 20 years of age is approximately 35% of the total body length. Given that the total body length for a female in ICRP 23 is 160 cm, the diameter of the thigh is roughly 17.83 cm. This was regarded as a relatively large dimension to represent the diameter of the leg in the joint region, which was measured on several women to be in the 10-11 cm range. It should be noted, however, that the value provided by ICRP 23 was for a measurement, "just below the gluteal fold and approximately in the horizontal plane".[28] Since the diameter of the leg decreases in the distal direction, the value of 10 cm was chosen for the phantom's outer diameter. Any underestimations in the amount of neutron scattering from the lack of tissue material in the upper leg portion of the phantom would likely be compensated for by the increase in material in the lower leg portion of the phantom. Aside from this data, it was determined that no other information regarding the average female leg dimensions existed.[25,29]

In order to gain further insight to establish the additional dimensions required, a computer-aided tomographic image of a 38 year old female leg was obtained using a STRATEC XCT-2003 pQCT imaging system. This system is used widely at the McMaster University Hospital for bone density scans. Three scans were obtained of the lower left leg. The axial scans were taken at distances of 30.40, 23.56, and 12.92 cm from the knee-joint and are shown in Fig. 2.

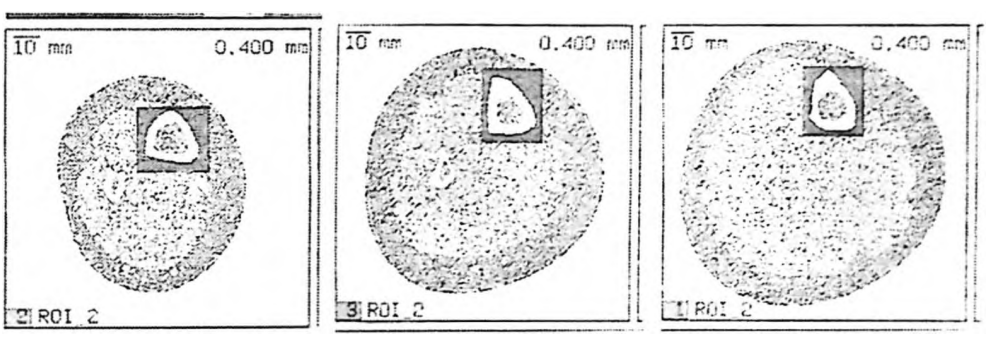

Figure 2 pQCT axial scans of the lower left leg of a 38 year old female a) 30.40 cm from the knee b) 23.56 cm from the knee and c) 12.92 cm from the knee.

Image (a) shows that the leg at 30.40 cm from the knee has a diameter of roughly 7 cm. The diameter increases to 9 cm at 23.56 cm shown in (b). At the most proximal position (c) (12.92 cm from the knee), the diameter is roughly 10 cm. This distance from the knee represents the thickest part of the lower leg where the calf muscle is located. Since this thickness is roughly that of the thickness of the leg at the knee, it was further established that a 10 cm diameter of the phantom was adequate. The diameter and positioning of the bones of the lower leg was also obtained from the image in scan (c). The fibula is roughly 1 cm in diameter and located approximately 1 cm off axis towards the outermost side of the leg. The tibia is somewhat larger with a diameter of 2 cm. It is positioned roughly 2.5 cm off axis towards the anterior side of the body and roughly 1 cm off axis towards the innermost side of the leg. The bones are surrounded largely by muscle tissue with about 1

cm thick layer of skin and subcutaneous fat. The tibia is located approximately 1 cm below the skin in the front part of the leg.

Additional measurements for the femur and tibial plateau were determined with some insight from dimensions listed by artificial bone maker Synbone AG, Switzerland.[30] The tibial plateau (proximal end of the tibia) width from the Synbone catalogue for model legs is given as 74 mm. The condular (distal end) width of the femur is listed as 86 mm. Since the ends of the two bones are somewhat irregular, a diameter of 60 mm was chosen to represent the width of both bones at the knee joint. The Synbone catalogue gives a femur canal diameter of 10 mm. A conservative thickness of 10 mm of cortical bone was added to this value to produce a phantom femur diameter of 30 mm. Although no data could be obtained for the height of the ends of the bones, from visualization of a dried femur bone available at McIARS, it was determined that the height of the ends was about the same as the width of the femur. Therefore this value was selected as 30 mm. With all the dimensions necessary to complete a phantom design a final schematic was prepared using AutoCADD 2000. The three views of the phantom are given in Fig. 3, 4, and 5 on the following two pages.

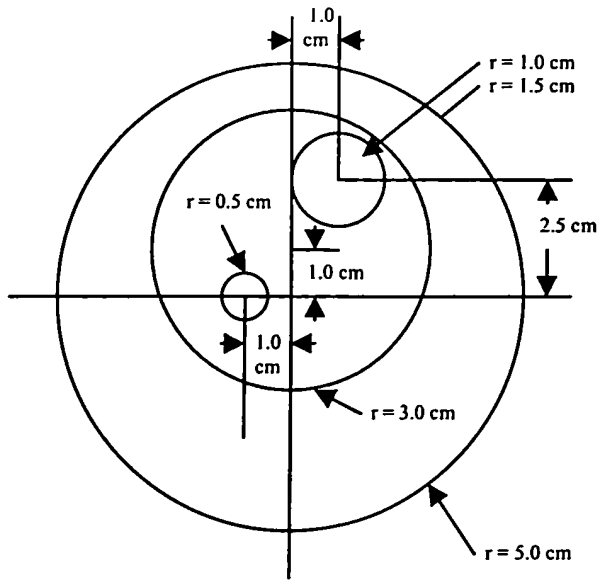

Figure 3 Bird's eye view of phantom lower leg showing tibia, fibula, and tibial plateau. N.B.: Diagram not to scale.

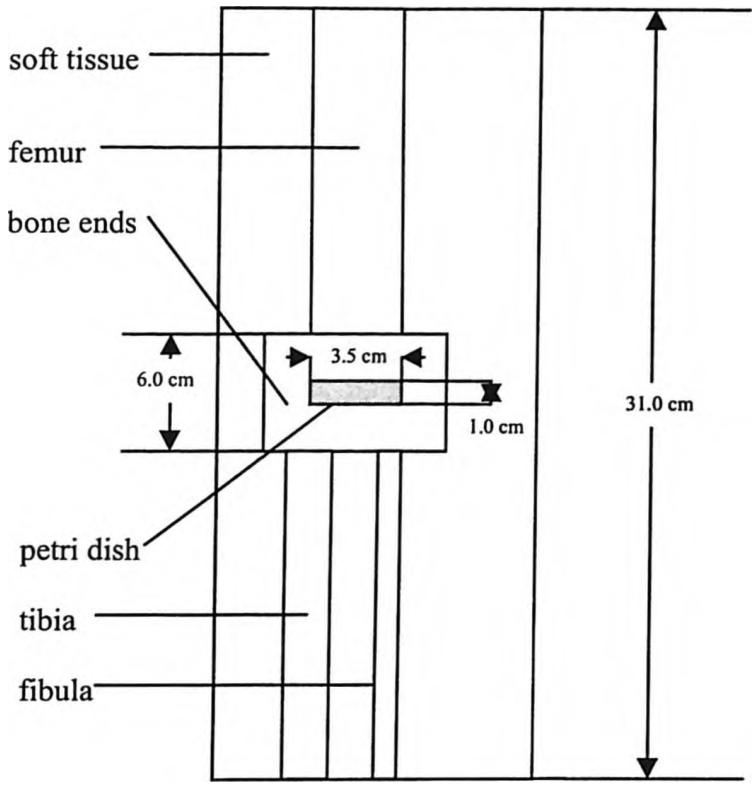

Figure 5 Side view projection of the total phantom leg showing femur, tibia, fibula, tibial and femoral plateaus (combined), and petri dish.
N.B.: Diagram not to scale.

2.3 Phantom Composition

Having a phantom design prepared, the materials used to represent soft tissue and bone were determined. Popular amongst clinicians and researchers alike, A-150 soft tissue equivalent plastic and B-100 bone equivalent plastic are often used for building irradiation phantoms. However, these materials are termed tissue equivalent with respect to high energy photons. Although present in the radiation field during neutron beam line

production, the photon flux was not the primary radiation component of interest for these studies. In order to produce a phantom that would be tissue equivalent with respect to neutrons it should have the same neutron effects as those present in both soft tissue and bone. That is, inelastic scattering, elastic scattering, and capture reactions to name but a few. Of these, elastic scattering of the neutron flux is primarily responsible for shifting the spectrum towards the thermal region. Classically, the neutron energy loss per collision will be high when the mass of the target is the same or close to that of a neutron. Thus, hydrogen is the principle element within any material that moderates the neutron flux. Water is the most common widely available source of large amounts of hydrogen for moderation, containing roughly 11% hydrogen by weight. Considering that the body consists of more the 60% water by mass it is no surprise that it is often used as a tissue equivalent material for neutrons.[28] Gierga et al. (2000) used a head phantom composed largely of water for their depth-dose verification. In the case of the anthromorphic phantom for cell culture irradiation, the use of water as the main phantom material was regarded as technically inappropriate. The petri dish could not be submerged, nor would it be a simple task to manufacture a phantom with compartments of water having varying elemental concentrations around the petri dish. Other phantom materials used at McIARS for In Vivo Neutron Activation Analysis (IVNAA) in the past have included Plaster of Paris, paraffin wax, and hardened polyester resin. Paraffin wax hardens quickly while being poured into molds and was not used due to considerations that the phantom could have a non-homogeneous composition. Of the three, polyester resin was chosen as the primary tissue component. Polyester resin is a branched chain polymer with a repeating molecular structure shown in Fig. 6 below.[31] Assuming the elemental composition of the resin is based on a high proportion of this repeating molecule, the resin contains 57.1429% carbon, 38.0952% oxygen, and 4.7619% hydrogen by weight. The density of the hardened polyester resin was measured to be 1.02 ± 0.05 g/cm^3, which is comparable to the ICRP 23 female total body specific gravity, 1.04 (g/cm^3).[28]

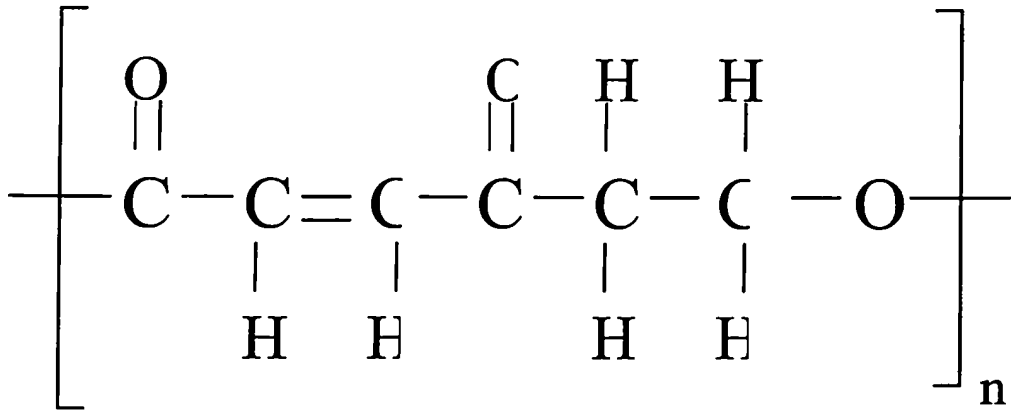

Figure 6 Repeating molecular structure of polyester resin chain.[31]

Of the four major components of soft tissue that are present in the human body, the only addition necessary to the polyester resin was nitrogen. ICRP 23 lists the total soft tissue mass for a male as 60 kg. The nitrogen content of this soft tissue mass is given as 1.5 kg for a total nitrogen composition by weight of 2.5%.[28] Bone tissue, too, contains high levels of the basic organic elements: hydrogen, carbon, oxygen, and nitrogen. Bone mineral is composed largely of hydroxyapatite, $Ca_{10}(PO_4)_6(OH)_2$.[28] Therefore, in addition to the four basic organic elements, calcium and phosphorus were considered essential in the phantom composition due to the potential impact on the neutron flux by these elements. Bone can be subdivided into two general categories, cortical (dense bone) and trabecular (spongy bone). The shaft of the long bones is composed of mainly cortical boney tissue while the ends of the bones contain larger amounts of trabecular boney tissue. Additionally, the bones contain blood vessels, nerves, bone marrow, and cartilage to name a few. While the modeling of all these tissues within the phantom was beyond the scope of this study, ICRP 23 listed elemental data for skeleton. The skeleton was considered the all encompassing tissue from which the phantom bone material data was derived. The total mass of the skeleton is given in the publication as 10 000 g. The nitrogen content of the skeleton was listed as 300 g, while calcium and phosphorus

content is listed as 1000 g and 700 g, respectively.[28] These values give corresponding proportions of 3%, 10%, and 7% by weight for nitrogen, calcium, and phosphorus. The specific gravity of the skeleton is given as 1.4 in ICRP 23.[28]

In order to manufacture the phantom, the polyester resin was first mixed with an addition of urea. Urea, NH_2CONH_2, is a widely available organic salt with a nitrogen composition of 46.7% by mass. Since the urea salt would not dissolve in the polyester resin, the salt was finely powdered using a mortar and pestle so that the powder would be suspended as homogeneously throughout the resin as possible. The powdered urea was then sifted slowly into a large amount of free flowing resin being mixed at a constant rate. The resin was then mixed for 3 minutes, until any sign of powdered urea was gone. The peroxide catalyst was then added and stirred continuously for another 2 minutes. The resin was then poured into cylindrical 3 l molds which had a length greater than 14 cm and a diameter greater than 12 cm. Details for the additions and volumes are given in Table 1 (next page).

The resin was then allowed to harden for 24 hours. The molds were removed and the cylindrical pieces of hardened resin were then machined to an outer diameter of 10 cm. The pieces were cut in the transverse direction so that the length was 16 cm. This created a total phantom leg length of 32 cm, which was considered adequate for neutron in-scattering. The cylindrical holes were then drilled into the each phantom piece. The top portion representing the upper leg was drilled first with a hole of 3 cm diameter throughout the cylinder, followed by a hole of 6 cm diameter to a depth of 3.5 cm. Both holes were drilled offset from the central axis by 1 cm. The bottom portion of the phantom representing the lower leg was drilled first with a hole of 2 cm in diameter offset 2.5 cm in the y-direction and 1 cm in the x-direction. Another hole with a 1 cm diameter was drilled offset 1 cm in the opposite x-direction. Finally, a hole 6 cm in diameter was drilled to a depth of 3.5 cm.

TABLE 1 Calculation of elemental fraction by weight and density for phantom soft tissue material.

UREA: 227.5272 g	N	H	C	O
Fraction by weight in urea	0.466460	0.067134	0.199994	0.266411
Total weight in urea	106.13234 g	15.27481 g	45.50407 g	60.61575 g
POLYESTER RESIN : 3800 mL x 1.01567 g/mL 3859.4966 g	N	H	C	O
Fraction by weight polyester resin	0	0.047619	0.571429	0.380952
Total weight in polyester resin	0 g	183.78537 g	2205.42828 g	1470.28295 g
Total weight combined	106.13234 g	199.06018 g	2250.93235 g	1530.89870 g
Total weight	4087.02357 g			
Total volume	3900 mL			
Total density	**1.047954762 g/cm^3**			
Total fraction by weight	**0.025968125**	**0.048705415**	**0.550751008**	**0.374575452**

The bone tissue was then prepared by adding powdered calcium hydrogen phosphate ($CaHPO_4$), calcium nitrate ($CaNO_3$), and urea. The salts were powdered again using a mortar and pestle, and sifted into the resin at a slow rate while constantly mixing. As the resin was visibly altered, a significant amount of catalyst was added in order to ensure hardening. The resin-salt mixture was then poured into the hollowed phantom. The phantom was then allowed to harden for 1 week. Details for the additions and volumes are given in Table 2 (next page). Once the phantom had hardened, 0.5 cm was removed from each bone-end side of the phantom pieces, ensuring a smooth bone-end surface. This reduced the phantom length to 31 cm in total. Grooves were created within the phantom such that the two pieces mated when placed together, ensuring a tight fitting

structure that would be free from unwanted movement. A hole 4.2 cm in diameter was drilled to a depth of 0.7 cm into the centre of each bone-end to create a space for the petri dish. Although the interior dimensions of the petri dish selected were 35 mm in diameter

TABLE 2 Calculation of elemental fraction by weight and density for phantom boney tissue material.

UREA: 18.32535 g	N	H	C	O	Ca	P
Fraction by weight in urea	0.466460	0.067134	0.199994	0.266411	0	0
Total weight in urea	8.54804 g	1.23025 g	3.66496 g	4.88208 g	0 g	0 g
CALCIUM HYDROGEN PHOPHATE: 97.05767 g	N	H	C	O	Ca	P
Fraction by weight in $CaHPO_4$	0	0.007408	0	0.470372	0.294567	0.227653
Total weight in $CaHPO_4$	0 g	0.71900 g	0 g	45.65321 g	28.58999 g	22.09547 g
CALCIUM NITRATE: 100.55375 g	N	H	C	O	Ca	P
Fraction by weight in $CaNO_3$	0.137209	0	0	0.470188	0.392602	0
Total weight in $CaNO_3$	13.79688 g	0 g	0 g	47.27937 g	39.47760 g	0 g
POLYESTER RESIN : 550 mL 1.01567 g/mL = 558.61135 g	N	H	C	O	Ca	P
Fraction by weight in polyester resin	0	0.047619	0.571429	0.380952	0	0
Total weight in polyester resin	0 g	26.60051 g	319.20673 g	212.80411 g	0 g	0 g
Total weight combined	22.34492 g	28.54976 g	322.87169 g	310.61877 g	68.06759 g	22.09547 g
Total weight	774.5482 g					
Total volume	690 mL					
Total density	**1.122533623 g/cm^3**					
Total fraction by weight	**0.0288489**	**0.0368599**	**0.4168516**	**0.4010322**	**0.0878804**	**0.0285269**

and 10 mm in height, the polystyrene material increased the overall dimensions of the hole. Therefore, the hole had to be drilled to a diameter large enough to accommodate the petri dish. The hole was also needed to be large enough such that a 0.5 mm thick activation foil could be inserted between the outer petri dish wall and the inner wall of the phantom bone. The final diameter of the petri dish cavity was 42 mm. A coordinate system was drawn onto each bone-end to identify the front (positive y-direction) and back (negative y-direction) so that the two pieces could be aligned centrally along the axis of the bone ends. Furthermore, the two pieces were identified for simple verification during experiments that the top and bottom pieces were in fact in their respective positions.

Chapter 3. Methodology

3.1 Phantom Validation

Characterizing a radiation field passing through an object or subject is most frequently performed using a depth-dose curve. Experimentally, the flux of ionizing radiation can be measured using semiconductor detectors, ionization chambers, and/or activation foils at various depths in the material/tissue to determine the change in field spectrum and intensity. Converting this data to dose via fluence-to-dose factors and plotting against the depth in material/tissue provides valuable information to the medical physicist. Simulations can be executed with an advanced particle transport code such as MCNP5, and field values of interest are scored using tallies at the corresponding depths in material/tissue. These values can then be compared against experimental data to determine whether the field has been modeled accurately, or, as in the case of this study, whether in fact the phantom modeled is a close estimate of that simulated. Gierga et al. (2000) performed in-phantom radiation field measurements using mixed field dosimetry techniques as described in Chapter 1. However, these techniques were performed in a head phantom composed solely of water. This allowed for the placement, positioning, and removal of ionization chambers and foils at will throughout the phantom. With a fixed structure phantom, as was the case in this study, such freedom was not afforded. Ionization chambers could not at all be used without boring large holes into the phantom structure. Such inhomogeneities would alter the radiation field beyond negligible effect, modifying the intent of study. Activation foils could be used, however, the element of choice was of some contemplation.

Neutron flux measurement via activation foils is widely used as a method of neutron dosimetry. The saturated activity, A_∞, of an activation foil irradiated by a neutron flux is given in Equation 1 below. [32]

$$A_\infty = \int \varphi(v)\sigma_a(v)NVdv = \int n(v)v \frac{v_0}{v} \sigma_0 NVdv = n_t v_0 \sigma_0 \theta \frac{m}{M} N_a \quad (1)$$

where:

φ: neutron flux per unit area, v: neutron velocity

σ_a: velocity dependant reaction cross section N: number density of target isotope

V: volume, v_0: thermal velocity, σ_0: thermal cross section

n_t: total neutron density, θ: isotopic abundance of target isotope

m: mass of activation foil, M: atomic mass of activation element, N_a: Avogadro's number

The thermal neutron flux, φ_{th}, can then be extracted by the following relation: [32]

$$\varphi_{th} = n_t v_0 = \frac{A_\infty M}{m\theta\sigma_0 N_a} \quad (2)$$

The saturated activity is achieved for infinite irradiation time. The actual activity of the sample is related to the saturated activity as shown in Equation 3.[32]

$$A_0 = A_\infty(1-e^{-\lambda t_r}) \quad (3)$$

where:

λ: decay constant of the radioactive isotope, t_r: time of irradiation

The activity of the activation foil is measured via scintillation or semiconductor detector. The activity, A_0, can be derived from the area of the counting peak, A_p, for the gamma ray energy of interest as follows:[32]

$$A_0 = \frac{\lambda \quad A_p}{(e^{-\lambda t1} - e^{-\lambda t2})\ \varepsilon\Gamma} \tag{4}$$

where:

t_1: cooling time after end of irradiation, t_2: cooling time + true time

ε: full peak energy efficiency, Γ: emission probability of gamma ray per decay

The thermal flux can, therefore, be arrived at from the peak area of the foil by combining Equations 2 through 4:[32]

$$\varphi_{th} = \frac{\lambda A_p M}{(e^{-\lambda t1} - e^{-\lambda t2})(1-e^{-\lambda tr})\varepsilon\Gamma m\theta\sigma_0 N_a} \tag{5}$$

Of consideration in choosing the element with which to perform such activation analysis are the available target isotopes that will produce detectable gamma rays, as well as the decay constant (i.e. half life). The half life of the resulting isotope should be neither too long nor too short. On any given day of experimentation many thicknesses of moderator would be added in front of the phantom and the resulting change in neutron flux measured. Since this procedure would require a considerable length of time, an element having a short half life was sought. An activation foil with a long half life would take very long irradiation times to approach the saturated activity level, which is highly desired. However, a half life that was too short would not allow for sufficient time for transfer and counting to produce acceptable peak counts above background (i.e. good statistics). It was found that copper was readily available and provided properties that were amenable to this study. Copper is composed of 69.17% ^{63}Cu and 30.83% ^{65}Cu.[33] ^{65}Cu undergoes a neutron capture reaction, producing ^{66}Cu, followed by delayed gamma emission, when bombarded with neutrons. The thermal neutron cross section for the reaction is 2.168 barns.[34] ^{66}Cu undergoes β^- decay with emission of a 1.039 MeV gamma ray at a yield of 9.23%.[35] The half life for the decay is 5.120 min.[35] A decay scheme is provided in Fig. 7.

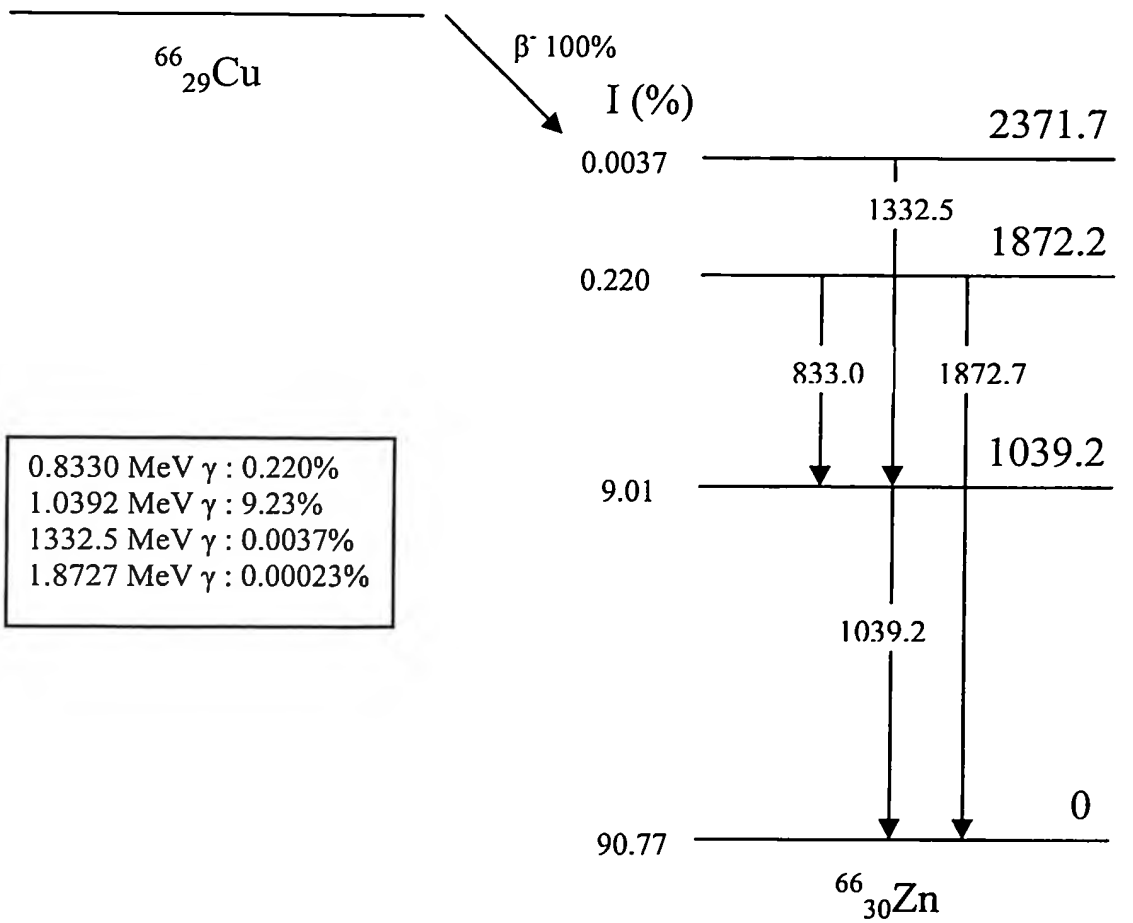

Figure 7 Decay scheme of ^{66}Cu. Only major transitions are shown. Energy levels, intensities, gamma rays emitted, and yields are listed in the diagram.[35]

In order to perform phantom validation, the positions of the foils were selected strategically. The design of the phantom did not allow for any activation foils to be inserted into the dense polyester resin itself. The thermal flux in the vicinity of the petri dish was of critical concern. Therefore, as described in Chapter 2, the hole in which the petri dish was located was widened to accommodate a foil placed next to it. The foil was selected to be quite thin at 0.5 mm. The foil length, therefore, had to be selected large enough so that the activity was adequate for statistical counting purposes. The length was

selected to be half the outer circumference of the petri dish, 12.65 cm. The height was that of the cavity, 1.4 cm. These dimensions allowed for the foil to cover roughly half of the surface area along the sides of the petri dish when intimate. The foil was located beside the posterior half of the petri dish. This sizing and placement also allowed for an unobstructed incident neutron flux. The foil provided neutron flux information with respect to the inner cavity of the phantom and was thus dubbed the "inner foil". A second foil was added at the back side of the leg phantom on the outer surface of the phantom.

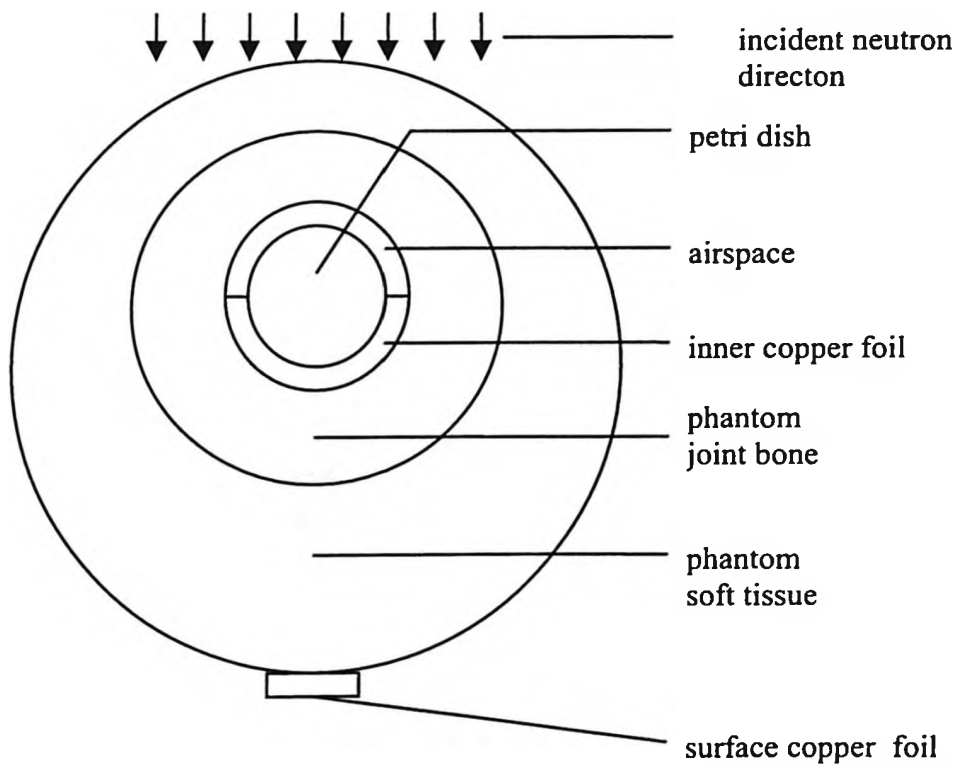

Figure 8 Cross sectional view of phantom at midplane showing the relative positions of both inner copper foil and surface copper foil within the phantom. N.B.: Diagram not to scale.

The position corresponded to the mid-plane of the phantom in both the x- and z-planes with respect to the phantom coordinate system described in Chapter 2. The shape of the foil was square with dimensions 2 cm by 2 cm by 2.323275 mm thick. This foil would provide exit thermal flux information and would give additional data with which to compare simulation flux values and was dubbed the "surface foil". A cross sectional view of the foil positions within and without the phantom is given in Fig. 8 above.

Now since the positions of the foils were stationary, a depth dose curve could not be performed. However, an alternative solution that would provide similar information to that of a depth dose curve was to add increasing thicknesses of moderator material in front of the phantom. This type of study would also determine the optimal thickness of moderator required to produce the maximum thermal flux in the vicinity of the cavity. Although Yanch et al. and Gierga et al. selected D_2O as the moderator of choice for their simulations, it was concluded that varying the dimensions of a container to increase the thickness of D_2O moderator was impractical. Instead, adding thin slabs of high density polyethylene (HDPE) would act equally well for neutron moderation. Since minimizing unnecessary dose to the phantom was beyond the scope of this study, the photon flux created via hydrogen-neutron interactions in the HDPE moderator, passing through the phantom, was of no concern. If in the future the use of polyethylene was in fact warranted, a perturbation study could be performed on the effect of the photon and neutron fluxes by the addition of a thin slab of lead positioned between the moderator and phantom faces. Polyethylene is widely used as a neutron moderating material in many neutron applications and has been shown to be a particularly desirable moderator for near-surface tumours in BNCT studies.[36]

3.2 Radiation Detection: NaI(Tl) System

The activity of the foils was measured following each phantom irradiation using an in-house built quasi-4π NaI(Tl) detector array.[37] This detection system was initially optimized to attain high efficiency detection of low level gamma rays for In Vivo Neutron Activation Analysis (IVNAA) at McIARS. Since NaI(Tl) crystals have higher detection efficiency than hyper-germanium (HPGE) crystals, and peak resolution was of lesser concern in this particular study, this type of detector system was selected. NaI(Tl) detection arrays also allow for improved cost, lower maintenance, and greater availability than their HPGE counterparts. The detector array is made up of square type NaI(Tl) crystals with dimensions 10.2 cm by 10.2 cm by 40.6 cm long. The crystals are housed in a steel casing 1 mm thick. When a gamma ray interacts with the crystal material a result is the emission of a pulse of light. Each crystal is coupled to a photomultiplier tube (PMT) that converts the light emitted within the NaI(Tl) crystal into an electronic pulse. A high voltage bias is applied to the eight crystals from a single high voltage supply. The signals from the PMTs are summed and then shaped using a bipolar shaping amplifier. The summed signal is then fed into a timing spectroscopy amplifier (TSCA: Harshaw, NA-23) and an analog to digital converter (ADC: Northern NS623). Concurrently, the eight TSCA signals are fed into a coincidence unit built locally (double width NIM module). The spectral data is then analyzed by a commercially available multichannel analyzer (MCA). Although this unit is designed to accommodate both coincidence and anti-coincidence counting modes, given the single detectable gamma ray emission of ^{66}Cu, the unit was operated in singles mode for the purpose of this study. Since the PMT gain of each detector unit shows time-dependent gain drift, the unit requires regular tuning for the stability of peak position. The actual solid angle subtended by the detector geometry is 3.83π sr, providing a 95% probability for gamma ray flux across the surface of the array.[37] The full peak energy efficiency for the gamma ray of interest has been measured to be 57.3%.[38] A schematic of the detector array is shown in Fig. 9 above. A block diagram of the signal processing electronics is shown in Fig. 10 (p. 39).

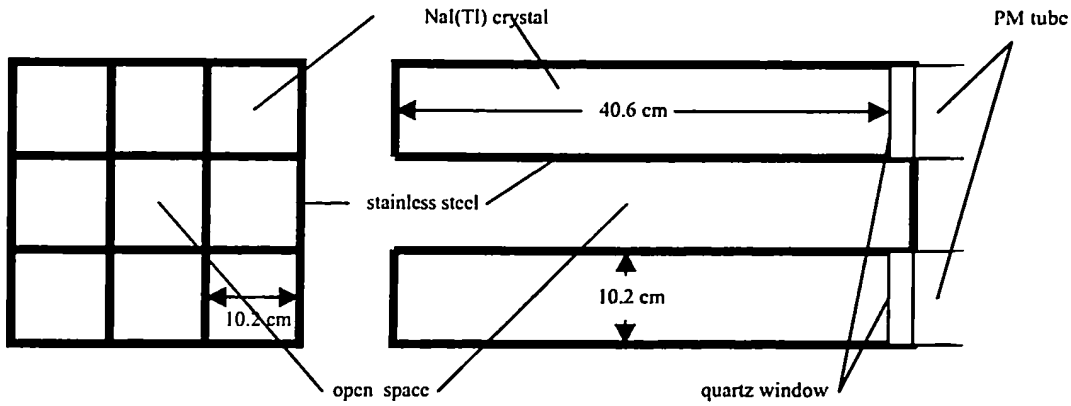

Figure 9 Cross sectional views of the NaI(Tl) quasi-4π gamma detector array. N.B. Diagram not to scale.[37]

In order to attain adequate counting statistics on each foil, the foils were counted for 120 s. Each inner foil was inserted within the detector array onto a foil holder fashioned out of thin cardboard. The inner foils were positioned onto their side, due to their curved shape. The foil holder suspended the foils approximately in the centre of the detector array. It has been shown that even a 5 cm shift in foil position relative to the long axis of the detector array in either direction of centre results in efficiency fluctuations less than 5%.[37] The surface foils were laid flat onto the foil holder at the centre of the detector array. Activities of all foils were kept to levels which resulted in dead times well below 10% in all cases.

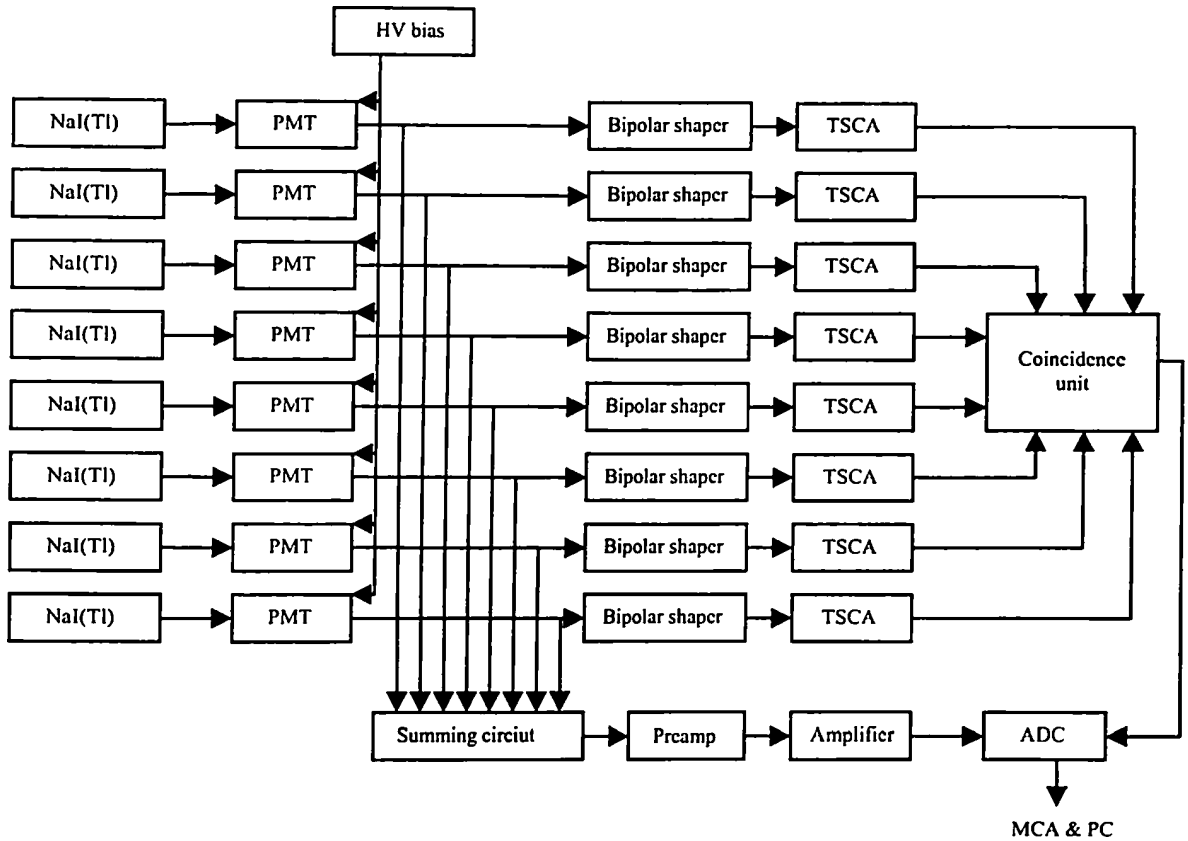

Figure 10 Block diagram of electronic setup for NaI(Tl) quasi-4π gamma detector array.[37]

The resultant energy spectra attained from the NaI(Tl) detection system were then analyzed using Microcal Origin.[39] The peak area of the gamma ray energy of interest was determined using the built-in Levenberg-Marquardt non-linear curve fitting routine for a Gaussian peak on a linear background given initial estimates of the critical parameters listed below. The equation used for fitting is given below:[40]

$$y = y_0 + sx + \frac{A}{w(\pi/2)^{1/2}} \exp[-2(\frac{x-xc}{w})^2] \qquad (6)$$

where:

y_0: y-intercept of linear background, s: slope of linear background, A: peak area

w: standard deviation of peak, xc: peak centre channel, x: channel

The fitting routine was repeated until chi-squared values could not be further reduced. This reduction, in general, lead to chi-squared values less than 1.5. The error associated with the counted peak area was dependant on the peak area itself, where the larger the activity the lower the error for low dead-time counts. Thus, inner foil count error was generally less than 2% for 2.00 MeV protons on target and less than 1% for 2.25 MeV protons on target, due to the increased neutron yield at higher incident proton energies (discussed below). The surface foil count error was generally less than 10% for 2.00 MeV protons on target and less than 4% for 2.25 MeV protons on target. An example of a copper spectrum obtained from an inner foil with its corresponding peak fit is provided in Fig. 11.

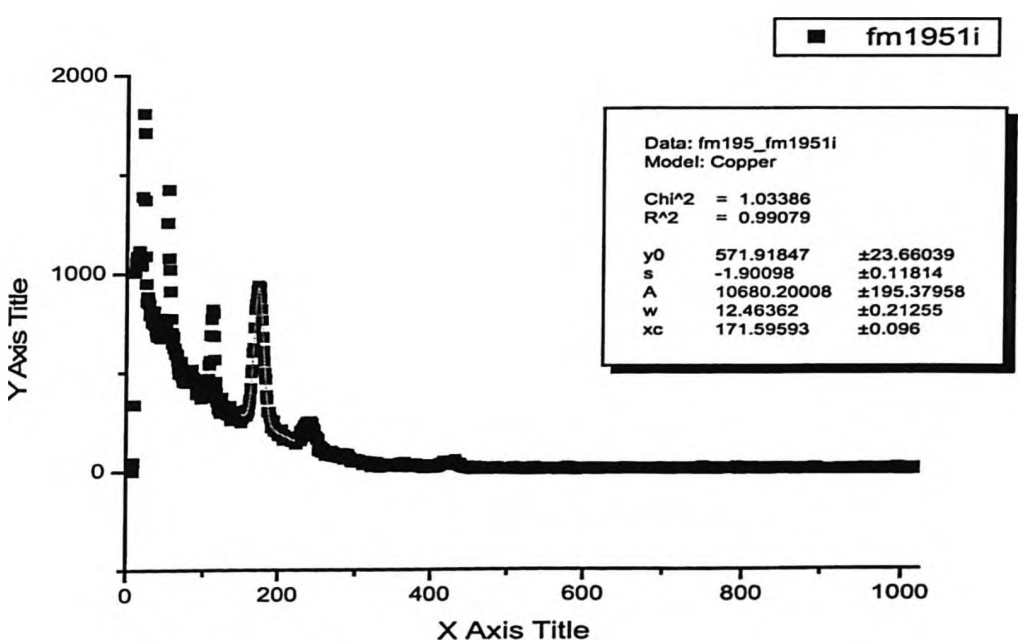

Figure 11 Typical ^{66}Cu decay spectrum measured using quasi-4π NaI(Tl) detector with fitted parameters.

3.3 Radiation Detection: Long Counter and Remmeter

Apart from the activation foils used to directly measure the neutron flux within and without the phantom, two additional measurements were made throughout each irradiation cycle. Both measurements were made using BF_3 counters, although the function of each counter was different. The "long counter", as it is commonly known, contains a long, thin cylindrical BF_3 counter with its long axis positioned horizontally, surrounded by HDPE moderator.[41] A schematic of the long counter used in this study is provided in Fig. 12.

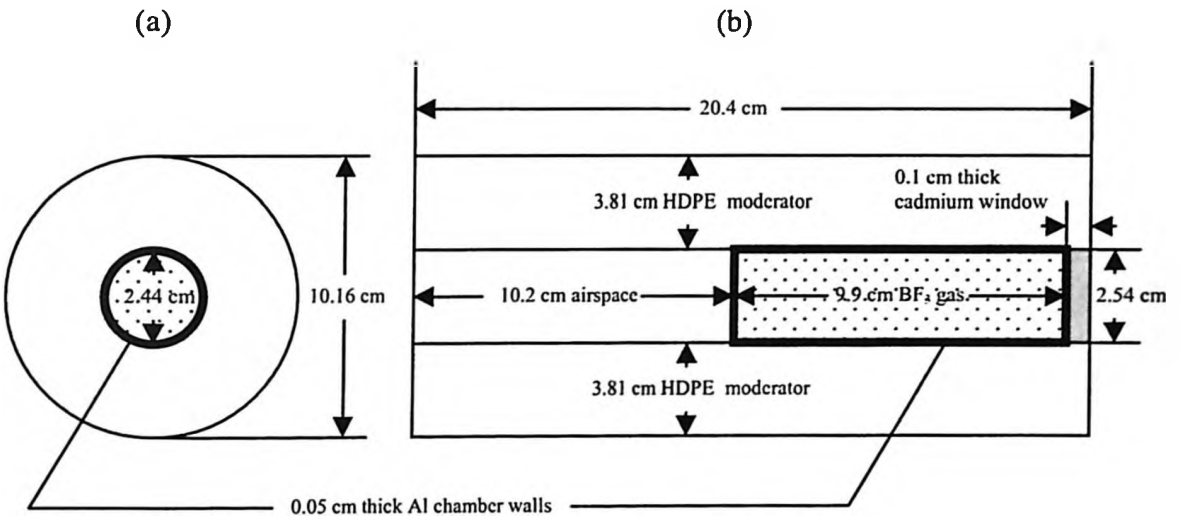

Figure 12 Schematic diagram of long counter a) transverse cross sectional view of long counter through BF_3 sensitive volume b) longitudinal cross section of long counter through BF_3 sensitive volume.

The long counter has a nearly flat neutron response function in the energy region 0.02 to 6 MeV. This detector is designed to respond specifically to neutrons incident on the front circular face. Typically a boron oxide shell within the long counter prevents

neutrons from directions other than the front face to be detected.[41] This long counter relied solely on the over-moderation of scattered neutrons from directions other than those incident on the front face. Thermal neutrons incident on the front face are filtered out by the cadmium window. Epithermal and fast neutrons incident on the front face are moderated by the HDPE layer and absorbed by the BF_3 gas. The airspace was included to prevent backscattering of neutrons into the sensitive volume after passing through it. The emission of the heavy charged particles via the same $^{10}B(n,\alpha)^7Li$ reaction as for BNCS allows for the deposition of nearly all the reaction energy within the counter volume. The long counter used in this study was developed in-house and the pulses arising in the sensitive volume were fed to a digital counter located in the accelerator control room, providing an integrated total neutron count for each irradiation.

The second neutron monitoring device used during irradiations was a portable Anderson and Braun remmeter (Tracerlab SNOOPY, Model NP-1).[42] The SNOOPY

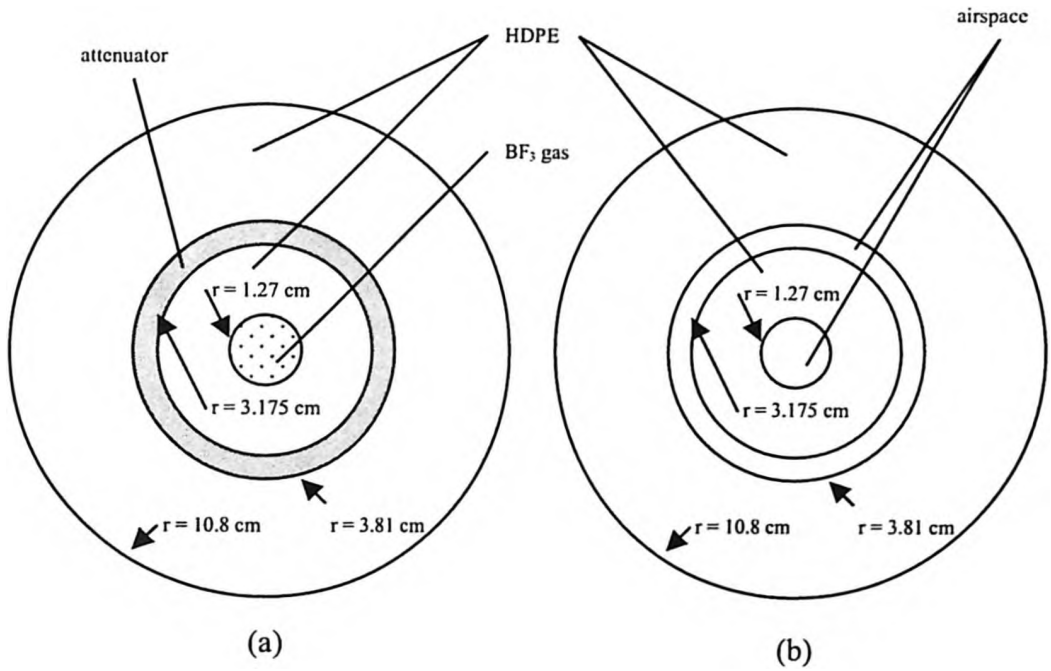

Figure 13 Cross sectional view of SNOOPY neutron remmeter through a) 11 cm from bottom face of detector b) 5 cm from bottom face of detector. N.B. Diagram not to scale.

remmeter has a BF_3 counter housed within HDPE and an attenuator composed of boron-10, carbon, hydrogen, silicon, and oxygen, in atomic ratios 0.398:2:6:1:1, respectively. The density of the attenuator is 1.2877 g/cm^3. The attenuator is placed strategically in alternating rings about the BF_3 sensitive volume. The SNOOPY counter is designed such that the sensitivity and reading are equivalent to human body dose in units of rem.[42]

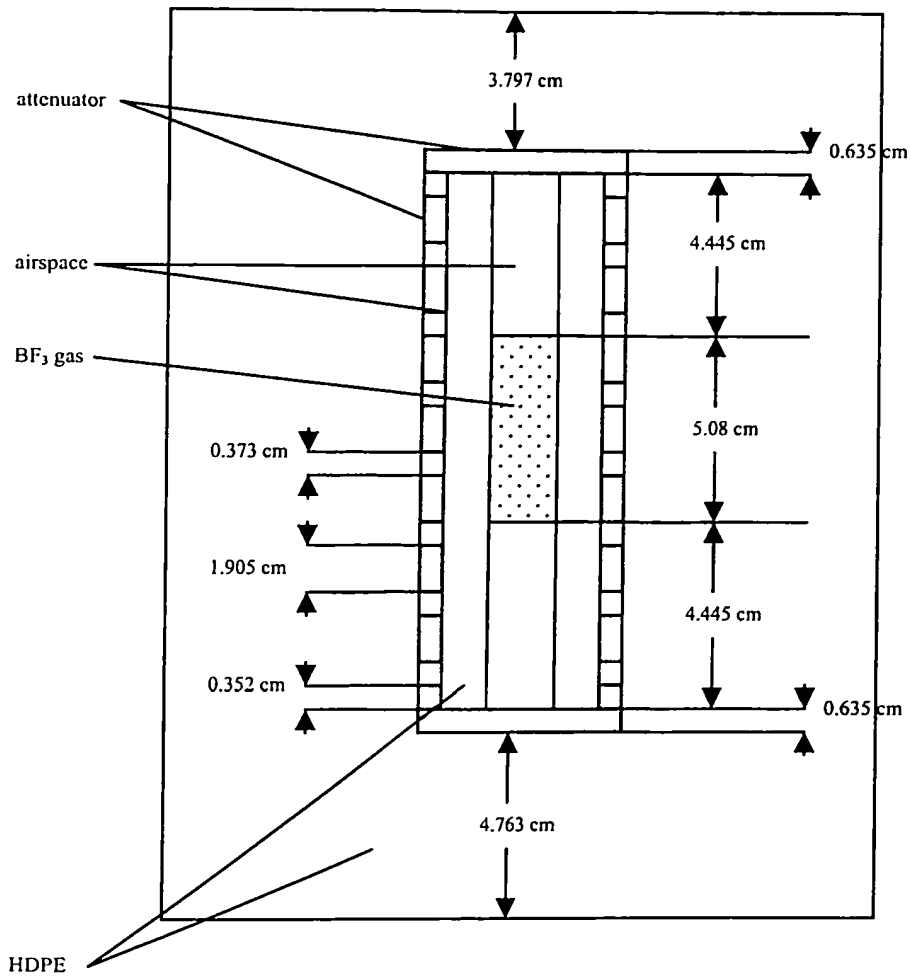

Figure 14 Longitudinal cross sectional view of SNOOPY neutron remmeter. N.B. Diagram not to scale.

The SNOOPY counter has, "high sensitivity and accuracy at low dose rates..." with a listed sensitivity of 9000 counts per mrem.[42] Opposed to the long counter, the SNOOPY counter was used as a real-time neutron count rate monitor. Schematic diagrams of the SNOOPY counter used are shown in Fig. 13 (p. 42) and 14 (p. 43). A block diagram of the electronic circuitry within the remmeter is shown in Fig. 15.

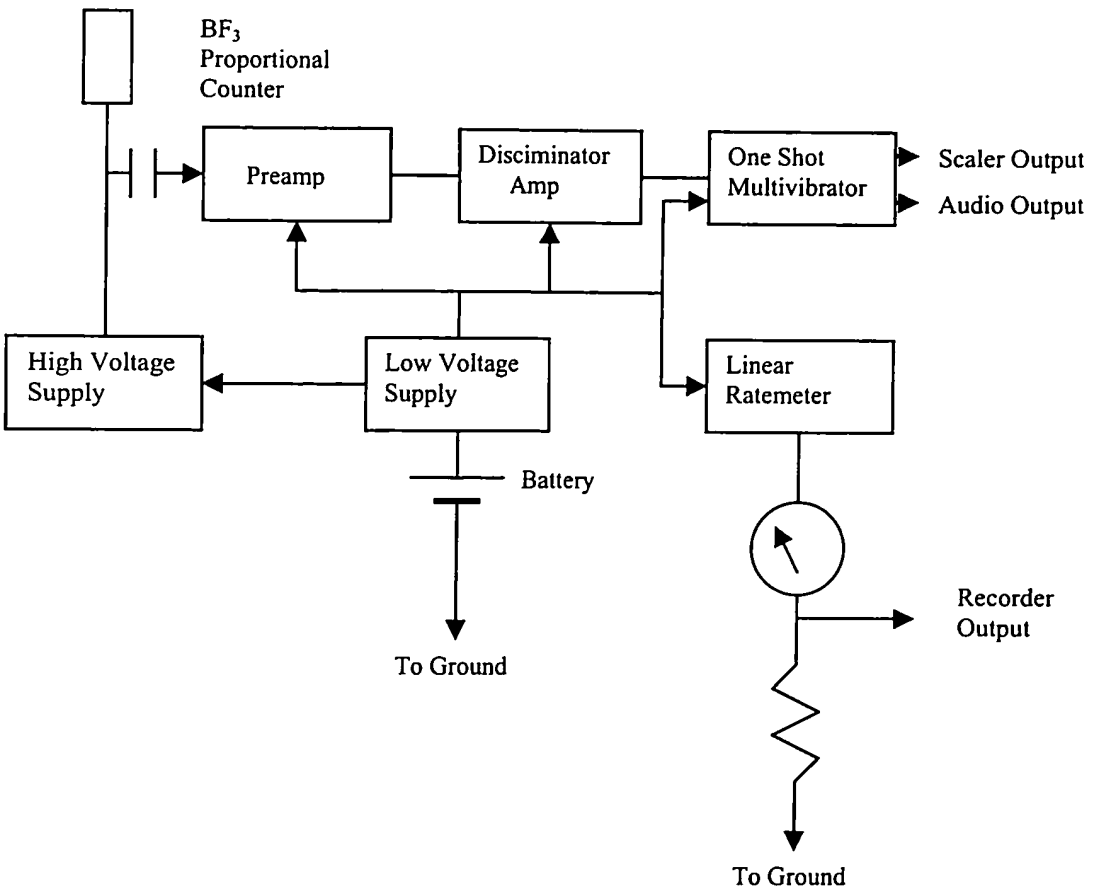

Figure 15 Block diagram of electronic circuitry of Tracerlab SNOOPY, Model NP-1.[42]

3.4 Neutron Source

The neutron source for the study at hand was a 3 MV Van de Graff type accelerator at the McMaster University Accelerator Laboratory (MAL). The fundamental basis on which this accelerator functions is the high electric potential difference produced

under vacuum. The potential difference is created via the transfer of positive static charge from a moving belt to a conductor plate. A hydrogen tank located within the accelerator unit provides the proton source for neutron production. As the protons enter the electric field they are accelerated due to the high electric potential difference between the supply and ground. At the far end of the unit the protons having high kinetic energy are steered down a beam duct via bending magnets. At the end of the beam duct is mounted a target. The target consists of a target holder and, in the case of this study, lithium metal (99.9% ^{7}Li). The "thick" lithium targets for this study were prepared by placing a weighed amount of lithium metal into an aluminum cup (holder) and depressing the metal into the target holder to 6895 kPa.[43] The thickness of lithium targets was between 1 and 3 mm, far greater than the proton range in lithium of 50 μm at the maximal proton energy studied.[43] The target holder is then mounted onto a brass beam cap that is electrically grounded. The target is cooled by channeled water (≈10°C @ 0.0063 m^3/s)[43] to prevent overheating which can result in lithium vaporization and vacuum failure. Although the lithium target diameter was dependent on the inner diameter of the aluminum cup (1.56 cm), the actual neutron source diameter was dependent on the beam diameter, which has been reported to be roughly 1 cm.[43] A cross-sectional diagram of the target holder is provided in Fig. 16 (next page).

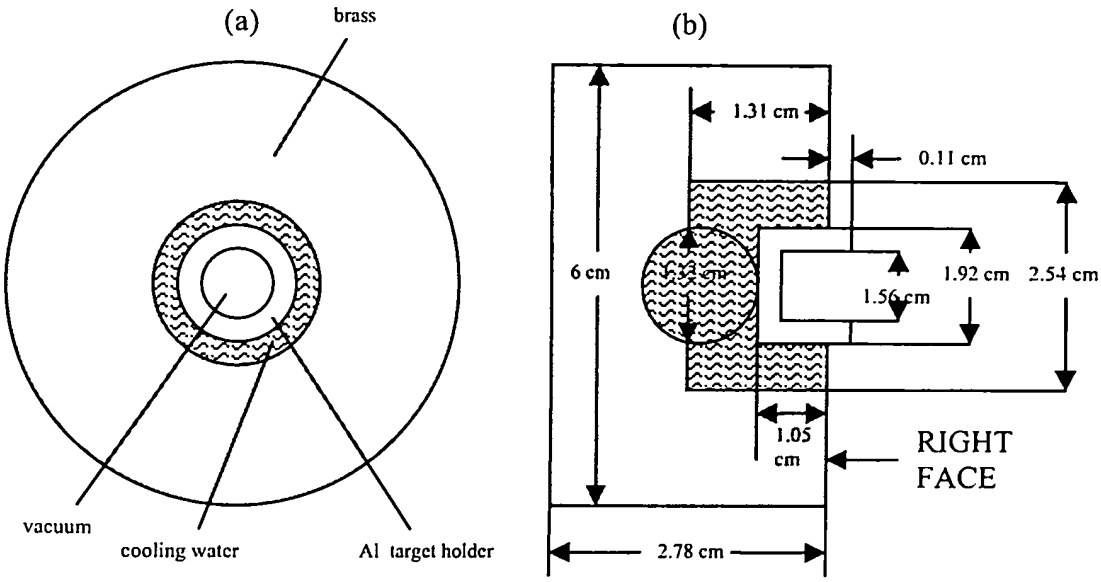

Figure 16 Schematic diagram of ^{7}Li target holder a) transverse cross sectional view through target holder 0.5 cm from right face b) longitudinal cross sectional view through midplane. N.B. Diagram not to scale.

Neutrons are produced via the ^{7}Li(p,n)^{7}Be reaction. The threshold for this reaction is 1.88 MeV. Due to the continuous slowing down of protons in the lithium metal a continuous spectrum of neutron energies is produced with an angular dependence at energies higher than threshold. The mean energy of the neutrons emitted in the forward direction increases with increasing incident proton energy. An additional result of increasing proton energy is the increase in total neutron yield per unit proton current. As mentioned in Chapter 2 the present current limitation on this accelerator unit is 80 μA. However, since the total duration of irradiations on any given day was 90 min, the current used in these studies was maintained at levels below 60 μA to preserve the target performance. With sufficient time and heating, the performance of the lithium target (i.e. neutron yield) degrades due to the loss of target from melting and vaporization, as well as the formation of an oxide layer from impurities in the vacuum beam line. A fresh lithium

target was replaced the day before each irradiation set in order to ensure maximal target performance. The accelerator unit was then pumped overnight to attain acceptable vacuum levels. Irradiations were carried out for 5 min intervals ($\approx t_{1/2}$). Although initial studies encompassed irradiations from 1.95 to 2.25 MeV protons in 0.05 MeV intervals, later studies focused on proton energies of 2.00, 2.15, and 2.25 MeV and are discussed in the following chapter.

3.5 Monte Carlo Simulation Modeling

Thermal flux values attained experimentally for the inner and surface foils for varying moderator thickness and proton energy were compared with particle transport simulations. The particle transport code used for this study was Monte Carlo N-Particle Version 5 (MCNP5).[44] MCNP5 is considered to be an advanced level code that can transport neutrons, photons, and electrons whether emitted directly from a source or as resulting from atomic interactions during transport. Three dimensional geometrical shapes called "cells" are created using the union and intersection of directionally specific surfaces. Surfaces are restricted to planes, infinite cylinders, and spheres, limiting the cell geometries to parallelepids, cylinders, and spheres, as well as intersections and unions of these volumes. Using complex programming advanced curvatures can be created, but was beyond the scope of this study. Materials are created using known atomic compositions in the "material card" portion of the code. Materials are then assigned numbers. Each cell is specified a material number and density according to its real composition. The "source card" defines the position, size, shape, energy spectrum, and angular distribution of the radiation source. A "mode card" selects the type of radiations to start and track throughout transport. Finally, a variety of tallies are available that can determine surface flux, surface current, cell averaged flux, flux at a point, cell averaged energy deposition, cell averaged fission energy deposition, and energy distribution within a cell (photons and electrons only). The typical MCNP code is run for hundreds of thousands to hundreds of millions of starting source particles and takes minutes to days to execute

depending on starting source particle number and computer performance. The actual number inputted by the user depends on the size and complexity of the geometry. The MCNP5 output lists critical statistical data for each tally entered. The MCNP5 manual lists recommendations of statistical performance for which a tally value can be deemed acceptable: the relative error for a tally should be less than 10% (5% for a point detector), the slope greater than 3 (10 ideal), the figure-of-merit (FOM) be nearly constant throughout the history, and the relative variance of the variance (VOV) should decrease inversely with the number of particles (N). The number of starting particles chosen by the user should be great enough to achieve most, if not all, of the above statistical criteria. Many variance reduction techniques are available to the MCNP5 user, but should be exercised with caution.

The irradiation area in the vicinity of the experimental phantom set-up would be extremely complex to model in MCNP5. Apart from the beam line wiring, cooling equipment, and infrastructure, there are many objects in the irradiation room such as a plywood table atop of concrete blocks, concrete walls, floors, etc. In order to limit the complexity and number of geometrical structures within the code, only those deemed to have critical effect on the neutron flux in proximity to the phantom and detectors were modeled. The phantom geometry and composition itself, as well as the petri dish and copper foils were modeled. The long counter, SNOOPY detector, HPDE moderator, wooden stand and table on which the phantom was placed, walls, and surrounding air were also modeled. The target holder, cooling water, and brass end cap were modeled in MCNP5, however, the rest of the beam line components were not. This was considered an acceptable exclusion since the neutrons are emitted in a highly forward direction.[45] All geometries listed above were modeled in the same manner as they have been presented in their corresponding figures throughout this paper. The position of the ^{7}Li target for the source card was positioned on the surface of the aluminum target holder and defined as the origin. The source cards used had been previously developed by Arnold et al.

(2000).[45] A sample of source energy spectra and angular distributions is provided in Fig. 17 (next page).

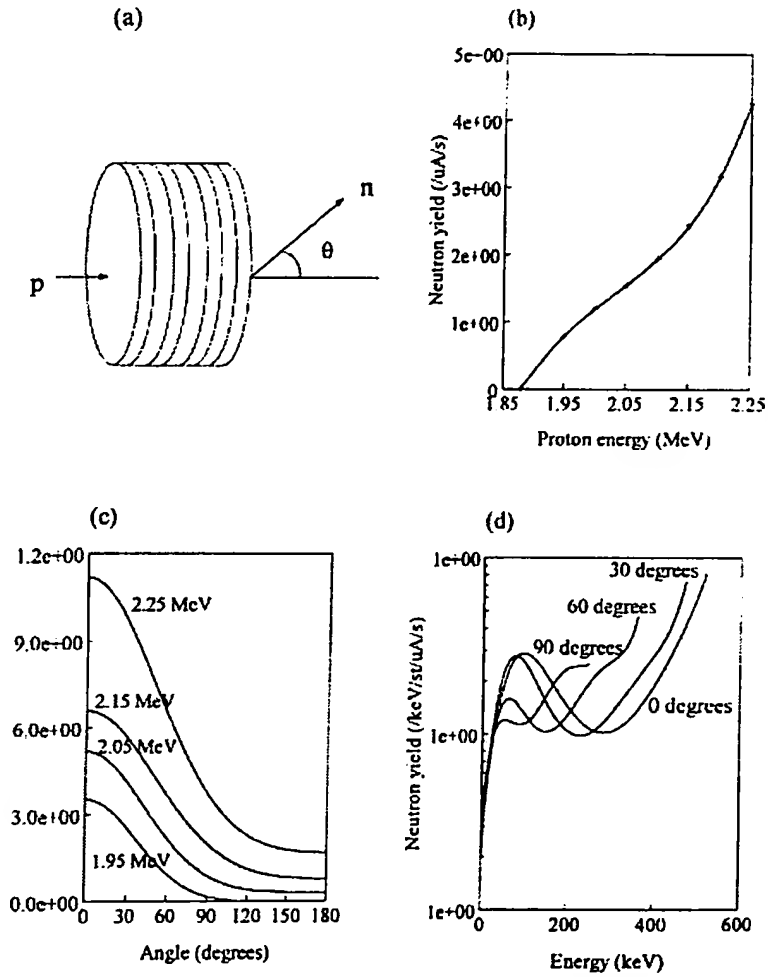

Figure 17 Modeling of the $^{7}Li(p,n)^{7}Be$ source a) The thick target represented by summing many thin targets with decreasing incident proton energy b) Neutron yield as a function of proton energy c) angular distribution of neutrons for the four proton energies d) Sample neutron spectra for a proton energy of 2.25 MeV, spectra for the proton energies can be obtained by truncating these spectra at the appropriate neutron energies.[58,45]

Typically, an "F4" tally can be used to determine the cell averaged neutron flux passing through a cell of interest. However, this neutron flux includes all components of the spectrum: thermal, epithermal, and fast neutrons. Experimentally, the thermal flux is

normally arrived at by using the "cadmium difference method".[41] This technique involves irradiating the activation foil in the neutron field twice, once wrapped in a cadmium sheath, and again bare. The cadmium difference method was determined to be difficult to implement in this study with the large number of foils irradiated at each proton energy studied. Since the performance of the target was of concern there was little that could be done to exactly mimic the experimental parameters attained on a given day. This condition would have to be satisfied to perform the cadmium difference method. Another option was to perform a similar extraction of the thermal flux from the total number of reactions, as was performed above from the activity of the foil. The total number of (n,γ) reactions (per unit proton current) occurring in each of the copper foils during a given irradiation is equal to the decay-corrected activity (per unit proton current) of the copper foils. That is to say that while in reality the total number of reactions occurs over a duration, t_r , and the number of detectable gamma rays changes with time, MCNP5 contains no temporal tracking. The total number of reactions, n_R, for each case is given in Equations 7 and 8 below.

$$n_R \{MCNP\} = N\sigma\varphi_{MCNP} \tag{7}$$

where:

N: total number density of the target isotope, σ: total reaction cross section

φ_{MCNP}: Monte Carlo transported neutron flux

$$n_R \{Experiment\} = \frac{N\sigma\varphi_{exp}(1-e^{-\lambda t_r})}{\lambda} \tag{8}$$

where:

N: total number density of target isotope, σ: total reaction cross section

φ_{exp}: actual neutron flux, λ: decay constant of product isotope, t_r: time of irradiation

The thermal flux within the copper foils can be arrived at from the MCNP5 number of reactions by taking the inverse of Equation 7 and substituting the thermal neutron cross section of ^{65}Cu for the total neutron cross section:

$$\varphi_{th}\{MCNP\} = \frac{n_R\{MCNP\}}{N\sigma_{th}} \quad (9)$$

The number of n,γ reactions is tallied by MCNP5 by specifying the material of interest (copper), the atomic density, and the reaction of interest (n,γ) in the "FM4 card" attached to the F4 tally. MCNP5 normalizes the output tally value by the number of starting source particles and must be multiplied by the actual neutron yield produced. This value cannot be arrived at directly but is taken from the literature based on theoretical calculations of the total thick target neutron yield per unit proton current.[43] The accelerator beam line is wired to measure the constant proton current at the final coupler located at the end of the beam line. The final equation used to convert the MCNP5 number of reactions to thermal flux is given in Equation 10.

$$\varphi_{th}\{MCNP\} = \frac{n_R\{MCNP\}\ V\ M\ A\ Y}{m\ \theta N_A\sigma_{th}} \quad (10)$$

where:

V: volume of foil, M: molar mass of copper, A: proton current,
Y: theoretical neutron yield per unit proton current, m: mass of foil
θ: isotopic abundance of ^{65}Cu, N_A: Avogadro's number

The MCNP5 thermal neutron flux determined by Equation 10 will be equivalent to the experimentally calculated thermal flux assuming the actual neutron yield produced by the accelerator for the known proton current is equal to that of the inputted MCNP5 neutron yield. Fluctuations of the actual neutron yield from the theoretical neutron yield have been reported as high as a factor of 7 difference.[43] Causes for the neutron yield discrepancies have been cited as presence of oxides in the target material, as well as

target material loss due to melting and vaporization.[43] The final experimental setup, as relevant to the MCNP5 modeling is shown in Fig. 18 (p. 53). Results and discussion of both experimentally determined and MCNP5 thermal flux values for the copper foils of the phantom at each thickness and proton energy are given in the following chapter.

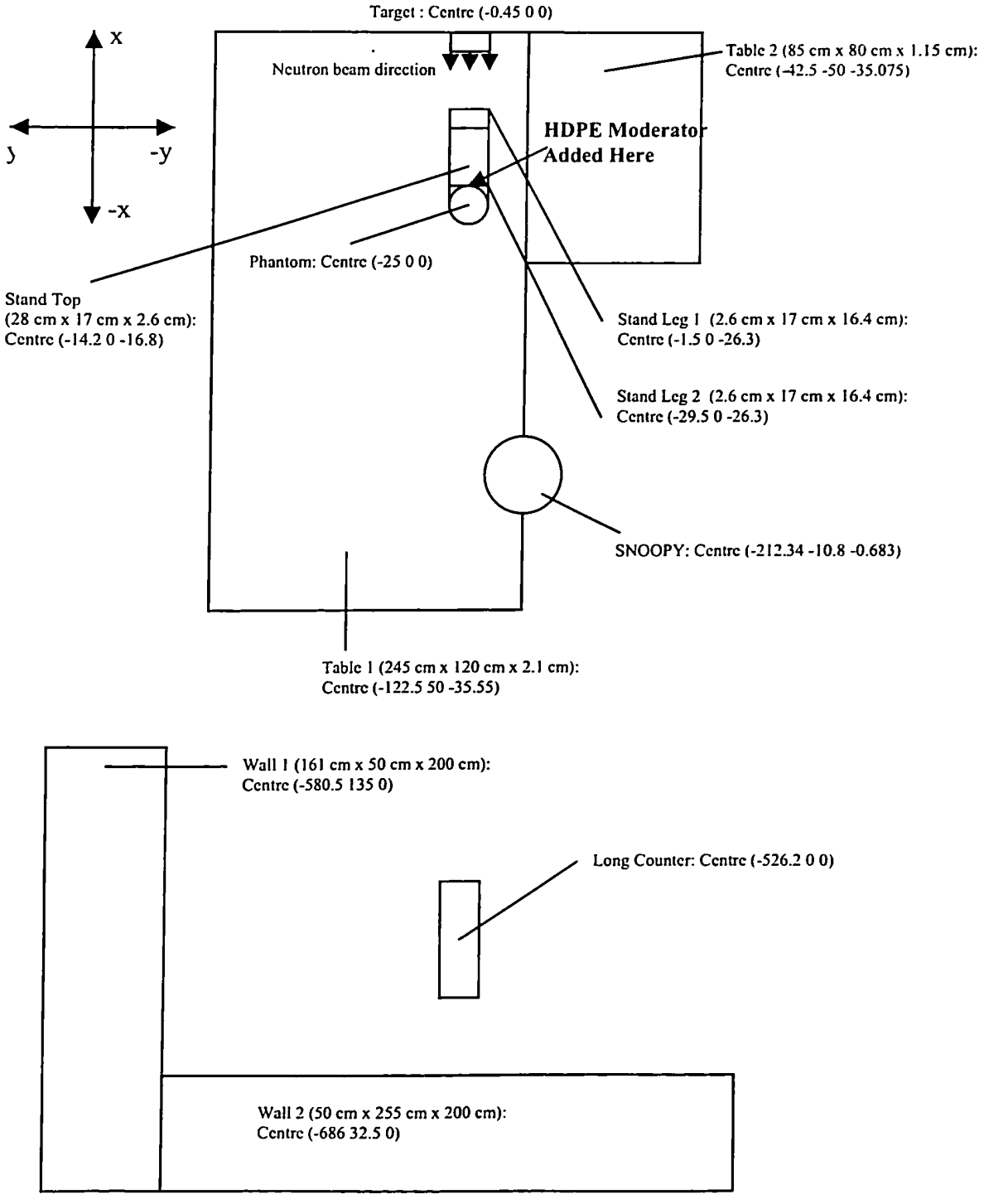

Figure 18 Bird's eye view of experimental irradiation room and setup. All positions are relative to MCNP coordinate system and are in units of centimeters. N.B. Diagram not to scale.

Chapter 4. Results and Discussion

4.1 Initial Data Comparison

It became apparent early in the study that the experimental setup as shown in Fig. 18 of the previous chapter was not suitable for the validation of the phantom. Initial comparisons of the thermal flux trend versus moderator thickness (length) for both experimental and MCNP cases were drastically different for the inner foils as can be seen in Fig. 19.

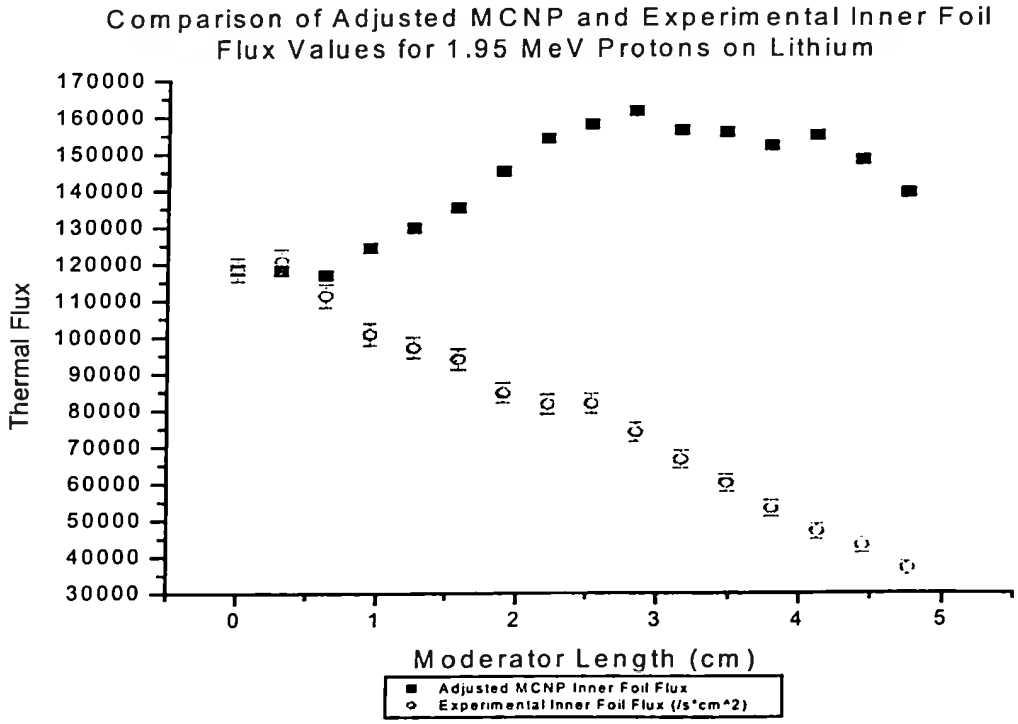

Figure 19 Graph showing inner foil experimental thermal flux and adjusted MCNP thermal flux with increasing HDPE moderator length for 1.95 MeV protons on ^{7}Li target. MCNP thermal flux values have been normalized to the 0 cm moderator length experimental flux value for comparison purposes.

In addition to the differing trend in each case, the MCNP5 thermal flux values obtained were a factor of 100 greater than the experimental values. This factor difference was significantly greater than the factor of 7 neutron yield fluctuations in the literature.[43] For ease of comparison, the MCNP data was normalized to the experimental thermal flux value for the 0 cm moderator length. The surface foil trend was not as drastically different as for the inner foil case, however, again a factor of 100 difference existed between the experimental and Monte Carlo derived values. The adjusted comparison for the surface foils is presented in Fig. 20. It should be noted that the errors shown were

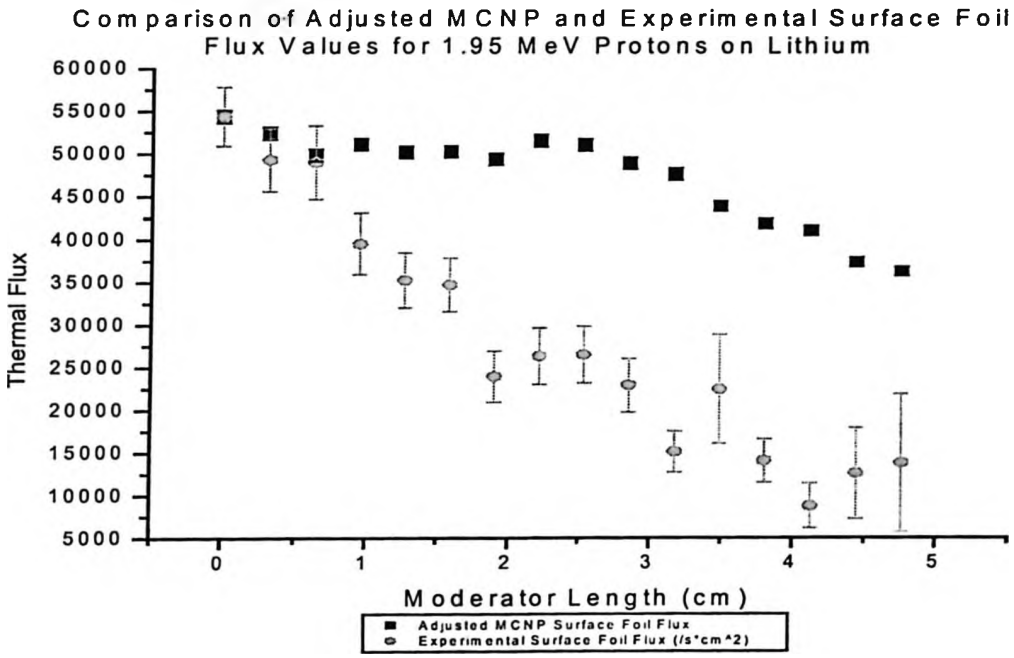

Figure 20 Graph showing surface foil experimental thermal flux and adjusted MCNP thermal flux with increasing HDPE moderator length for 1.95 MeV protons on ^{7}Li target. MCNP thermal flux values have been normalized to the 0 cm moderator length experimental flux value for comparison purposes.

less than 1% and less than 5% for the MCNP5 and experimental data for the inner foil, respectively. The MCNP5 data for the surface foil was less than 2%, but the experimental error ranged from less than 12% for the first eleven slabs of moderator to 28-59% for the remaining points (with increasing moderator length). This large relative error was due the low activity of the surface foils at large moderator length.

4.2 Possible Causes for Inconsistencies

Hypotheses as to the nature of the differences between these values included impurity of the copper foils used, incorrect density of HDPE moderator, errant MCNP5 ^{65}Cu cross section data, loss of neutron yield due to lithium target melting and oxidation, errant input source cards, and phantom inconsistencies (original unknown). In typical IVNAA studies performed at MAL, the trace element concentration of interest is varied in a set of phantoms while moderator length is fixed. Thus, the SNOOPY remmeter can be used as a real time neutron yield monitor allowing the accelerator operator to adjust the proton beam spot to an unaltered target area, maintaining a constant neutron yield (i.e. constant neutron dose). During analysis, the long counter output for each sample can be used to normalize each corresponding data value. In the case of this study the addition of HDPE moderator varied the thermal flux within the phantom but, due to the positioning of both the SNOOPY and the long counter, also varied the fluxes at these detectors. Hence, the accelerator operator could no longer ensure constant neutron production. The only reference by which the operator could attempt to maintain the neutron yield was by sustaining a constant proton current. However, this by no means is a figure of merit for keeping a steady neutron production rate. The SNOOPY remmeter output, as well as the long counter output, also deviated greatly from the MCNP5 predicted output. The resulting issue was a difficulty in ensuring that the data comparisons were valid even upon normalization with the long counter or the SNOOPY. A target performance test, in which the moderator length remained the same but all 16 foil sets were irradiated in the same manner as before, was undergone. The test showed that the neutron yield from the

target, without adjusting the neutron beam spot, did in fact remain relatively stable. However, given that for each set of irradiations the lithium target was replaced, it was still deemed that a constant neutron yield was an unsuitable assumption.

Testing was next performed on the original MCNP5 source cards used. The source cards used were derived from those compiled by Arnold et al. (2000)[45] based on cross section data published by Liskien and Paulsen (1975)[50] and stopping powers from Nuclear Data Tables (1960)[51]. Source cards were available for proton energies 1.95, 2.00, 2.05, 2.10, 2.15, 2.20, and 2.25 MeV. Aslam et al. (2003) also produced MCNP5 source cards for their studies at MAL for near threshold neutron production proton energies (1.88 – 1.93 MeV).[52] Aslam et al. utilized a slightly different algorithm from that used by Arnold et al., in which the Breit-Wigner approximation was used to determine the differential neutron yield. Source cards for 2.00 MeV and 2.25 MeV protons were

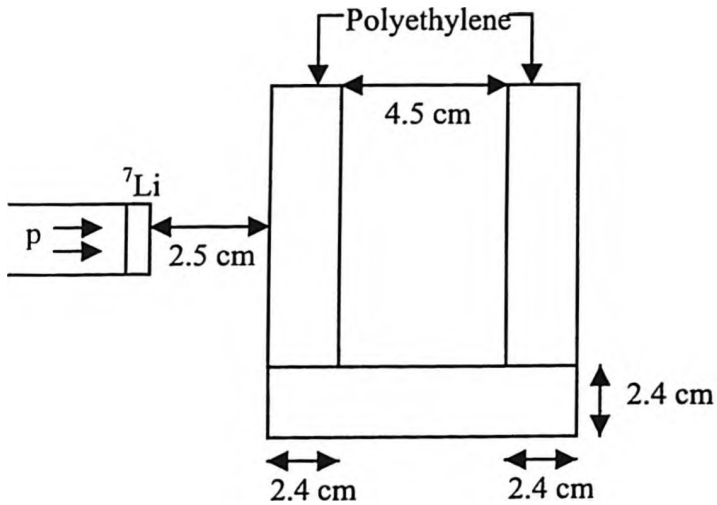

Figure 21 Schematic of hand irradiation cavity for IVNAA at MAL. Inner dimensions of the cavity are 30 x 30 x 4.5 cm. N.B. Diagram not to scale.

obtained from Aslam and compared with those of Arnold et al. MCNP5 output comparisons were carried out for a known hand irradiation cavity geometry developed at MAL.[53] A schematic of this cavity is shown in Fig. 21. MCNP5 spectral output is shown

in Fig. 22 and 23 below for both Arnold and Aslam source cards at 2.00 MeV. MCNP5 spectral output is shown in Fig. 24 and 25 (next page) for both Arnold and Aslam source cards at 2.25 MeV.

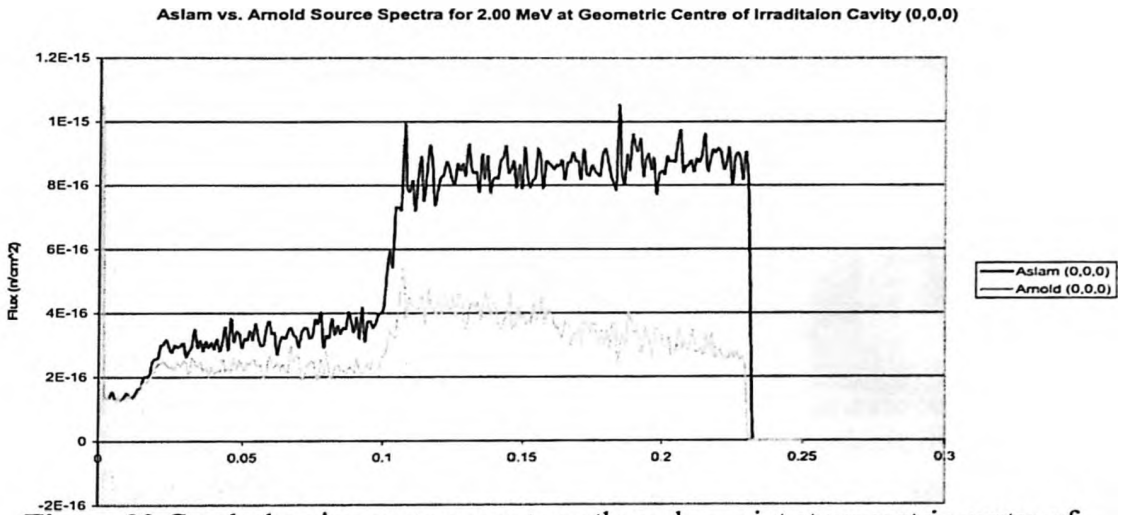

Figure 22 Graph showing neutron spectrum through a point at geometric centre of hand irradiation cavity corresponding to 0° angle relative to the incident proton direction for 2.00 MeV protons on lithium.

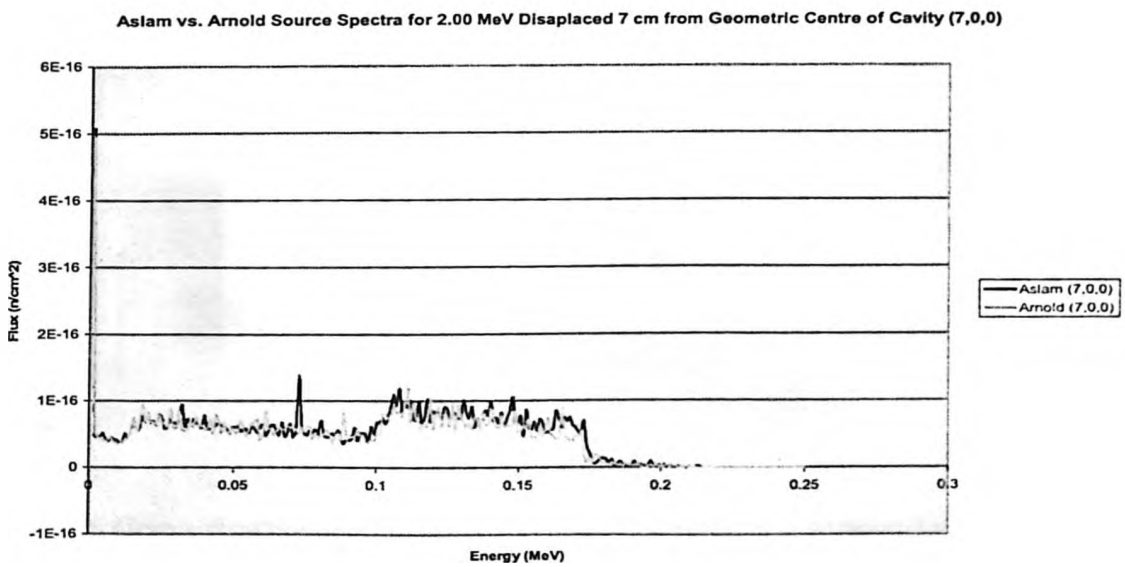

Figure 23 Graph showing neutron spectrum through a point at displaced 7 cm from geometric centre of hand irradiation cavity corresponding to 38.2° angle relative to the incident proton direction for 2.00 MeV protons on lithium.

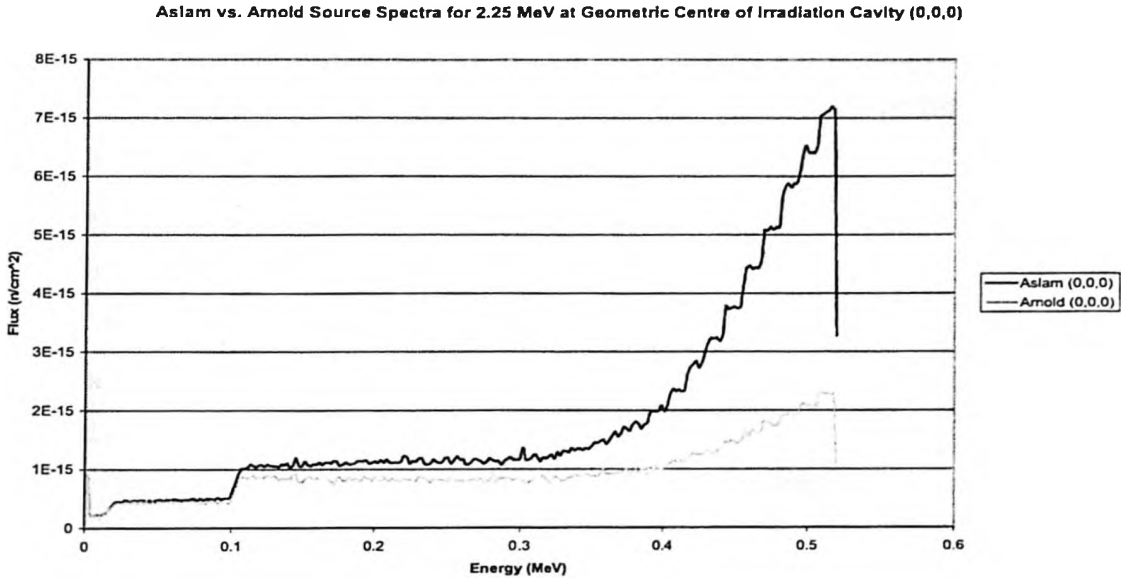

Figure 24 Graph showing neutron spectrum through a point at geometric centre of hand irradiation cavity corresponding to 0° angle relative to the incident proton direction for 2.25 MeV protons on lithium.

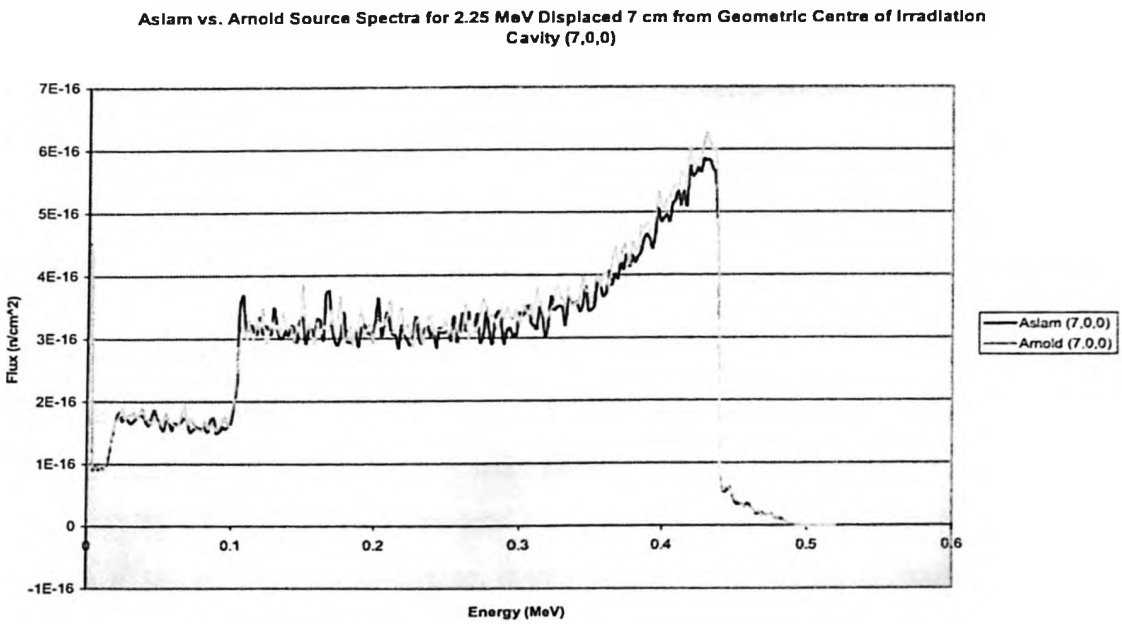

Figure 25 Graph showing neutron spectrum through a point at displaced 7 cm from geometric centre of hand irradiation cavity corresponding to 38.2° angle relative to the incident proton direction for 2.25 MeV protons on lithium.

As can be seen from both Fig. 22 and 24, the 0° spectra, although similar in shape, were different. It should be noted that although the differential neutron angular yield is peaked in the 0° direction, the actual neutron emission in the 0° direction will be zero. This is due to the fact that the angular neutron emission spectrum is derived by multiplying the differential neutron angular yield by the $2\pi \sin\theta$ term from the solid angle differential term.[54] By utilizing the Breit-Wigner approximation Aslam et al. derived source card spectra that differed in the 0° region from those of Arnold et al. However, as can be seen in Fig. 23 and 25, the neutron spectra at 38.2° were virtually identical. It was thus concluded that in order to perform phantom validation the phantom location should be positioned at an angle away from the 0° direction of incident protons. The new phantom position was selected to be at an angle of 45° relative to the incident proton direction. In addition to the repositioning of the phantom, it was also decided to move the SNOOPY remmeter location away from the phantom and HDPE moderator. The SNOOPY was relocated to the opposite 84.47° location (relative to the incident proton direction) of the phantom (i.e. 129.47° relative to the phantom) and 93 cm from the target. Thus the SNOOPY position was far away enough from the phantom and moderator that the SNOOPY response could be maintained constant to ensure a steady neutron production rate. The repositioning of the phantom, moderator, and SNOOPY remmeter now afforded the long counter an unobstructed neutron production solid angle to the long counter.

In addition to the verification of the source cards, the MCNP5 ^{65}Cu (n,γ) cross section data was compared with the ENDF/B-VI (n,γ) cross section data for ^{65}Cu.[55] It has been known throughout the MCNP user community that a shift in the neutron cross section tables of various isotopes has occurred in the material data portion of the program, in the past.[56] This, of course, is understandable given the incredible amount of cross section data stored for use by the code. However, after printing and comparing the cross section graphs from both the MCNP5 material data files and the ENDF/B-VI for the (n,γ) reaction, the two were found to be identical confirming that the material data file for

^{65}Cu was correct within MCNP5. The next step was to test the purity of the copper foils used. The copper foils were run through the PGNAA facility at the McMaster Nuclear Reactor (MNR), along with a copper sample of purity known to be 99.99% natural isotopic copper. The copper foils were confirmed to be 99% pure copper. Finally, the density of HDPE slabs was measured to be 0.979 g/cm^3. This was a slight increase from the original density used in the MCNP5 codes of 0.94 g/cm^3 obtained from the National Institute of Standards and Technology.[57]

After some reevaluation of the MCNP5 codes, the principle cause of the large factor difference between the MCNP5 output and experimental data was found. Originally, the first entry in the FM4 card of the F4 tally was selected as the value 1, which was to indicate to the code that the final tally should be multiplied by a factor of 1 (i.e. no additional factors). It was further discovered that in order to perform this function the input should be -1. Although this adjustment reduced the MCNP5 thermal flux values to a factor of 30 difference, it did not reduce them to the factor of 7 difference that was considered acceptable in the literature. By keeping the first entry of the FM4 card positive indicated to the code that the density of the material was to be multiplied by the given factor in units of atoms/barn-cm. After reviewing several examples in the MCNP5 user manual the final solution became apparent; in order to perform a reaction rate study of an element such as copper, a separate material card was to be created which contained only the ^{65}Cu isotope. In other words, the other major isotope of natural copper, ^{63}Cu, although it emitted no detectable gamma rays of interest, was contributing to the reaction tally. Therefore, in addition to the material card for natural copper (69.17% ^{63}Cu, 0.3083% ^{65}Cu) for purposes of particle transport, a separate material card was created for ^{65}Cu in 100% abundance for purposes of reaction tally (i.e. activity). This was the material for which the F4 tally was to be performed. The abundance was then corrected to its naturally occurring value, 0.025620738 atoms/barn-cm, in the FM4 card entry. This type of study is dubbed a "perturbation" within the code framework.

4.3 Copper Test Geometry

Having made all the corrections discussed above (changes to FM4 card of MCNP5 code, changes to the positions of the phantom, moderator, and SNOOPY, confirmation of cross section data, copper foil purity, HDPE density), the final possible cause of the inconsistencies between the thermal flux trends of MCNP5 and experiments was the phantom composition itself. Since verifying this was the original purpose of study, an initial verification of the MCNP5 output was performed by using a material of known composition. Since the HDPE moderator was widely available, and its composition and density were well established, it was selected as the material of choice. The "copper test geometry", therefore, consisted of an HDPE moderator with a copper foil positioned at the center of the rear face, at the 45° position (relative to the incident proton beam direction). This copper foil was dubbed the "test foil". Although the SNOOPY and long counter readings were now better established, an additional figure of merit was created in the experimental setup by including a slab of HDPE, dubbed the "holder", at the opposing 45° position (relative to the incident proton direction) of the moderator/copper setup. A copper foil, dubbed the "standardizing foil", was positioned at the centre of the front face of the holder. The experiment was repeated with fresh copper foils while increasing the moderator length but maintaining a constant holder thickness. The data derived from the test foils could now be normalized via the standardizing foil data (i.e. flux ratio). By performing this normalization it was expected that any decrease in neutron production throughout the day, which could not be detected by the SNOOPY reading, would be negated. A diagram of the "copper test geometry" is shown in Fig. 26 (next page). Although they have been shown for completeness sake, the SNOOPY and long counter responses were not modeled in the MCNP5 code. The SNOOPY was, however, used as a real time neutron production monitor during irradiations. The SNOOPY dose response was maintained constant to obtain a constant neutron production rate. Also, as can be seen from the diagram, the wooden stands and

wooden tables were omitted from the MCNP5 code. These were found not to affect the neutron flux at the copper foils to any significant respect in MCNP5. The removal of the

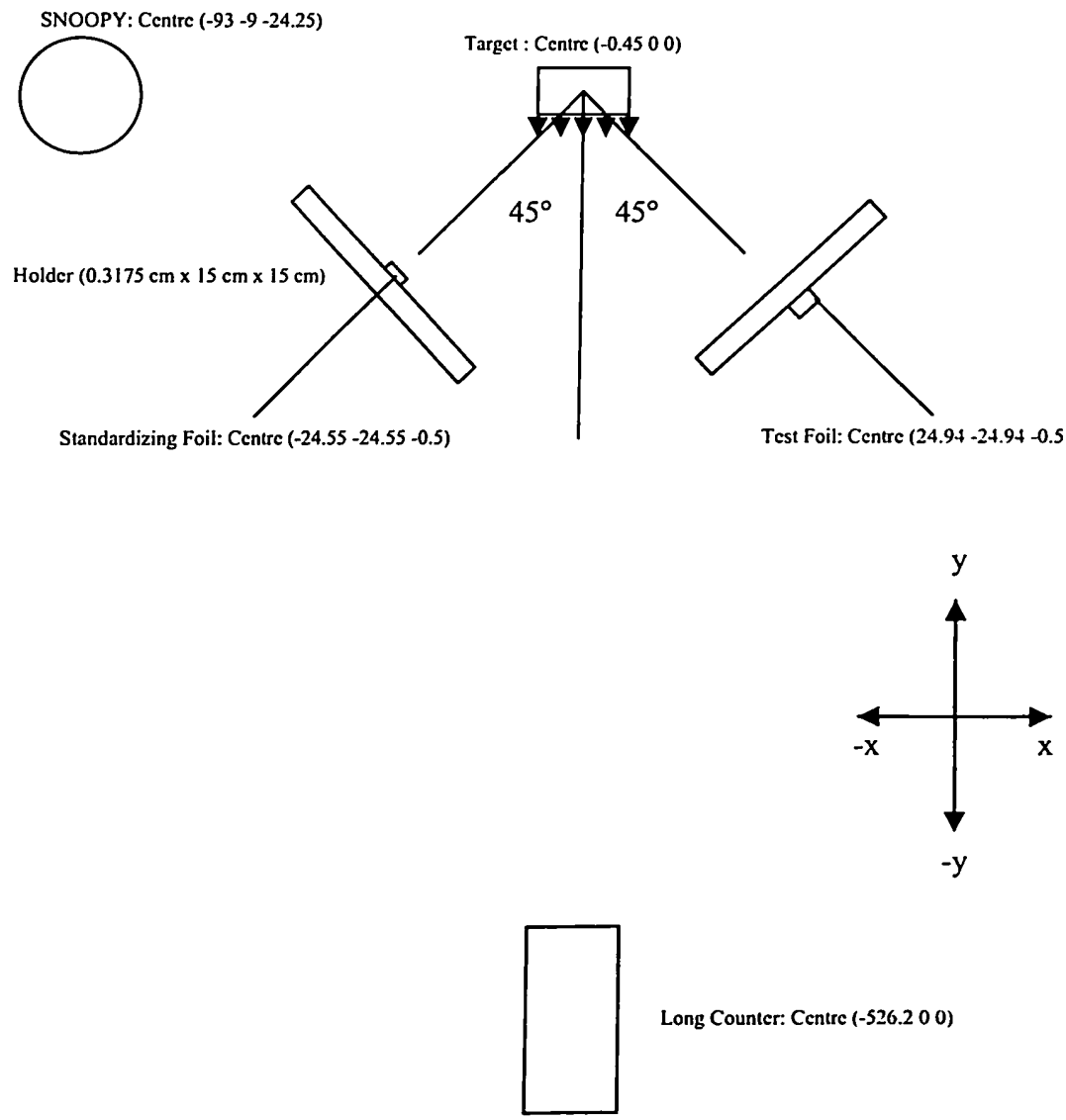

Figure 26 Bird's eye view of experimental irradiation room and setup for Copper Test Geometry. All positions are relative to MCNP coordinate system and are in units of centimeters. N.B. Diagram not to scale.

wooden items allowed for more efficient execution of the transport code. The MCNP5 codes were performed using the source cards provided by Aslam for 2.00 and 2.25 MeV protons on a thick lithium target. The data for the 45° geometry is provided in Fig. 27, 28, and 29 for 2.00 MeV. The data for 2.25 MeV protons on lithium in the 45° geometry are shown in Fig. 30, 31, and 32.

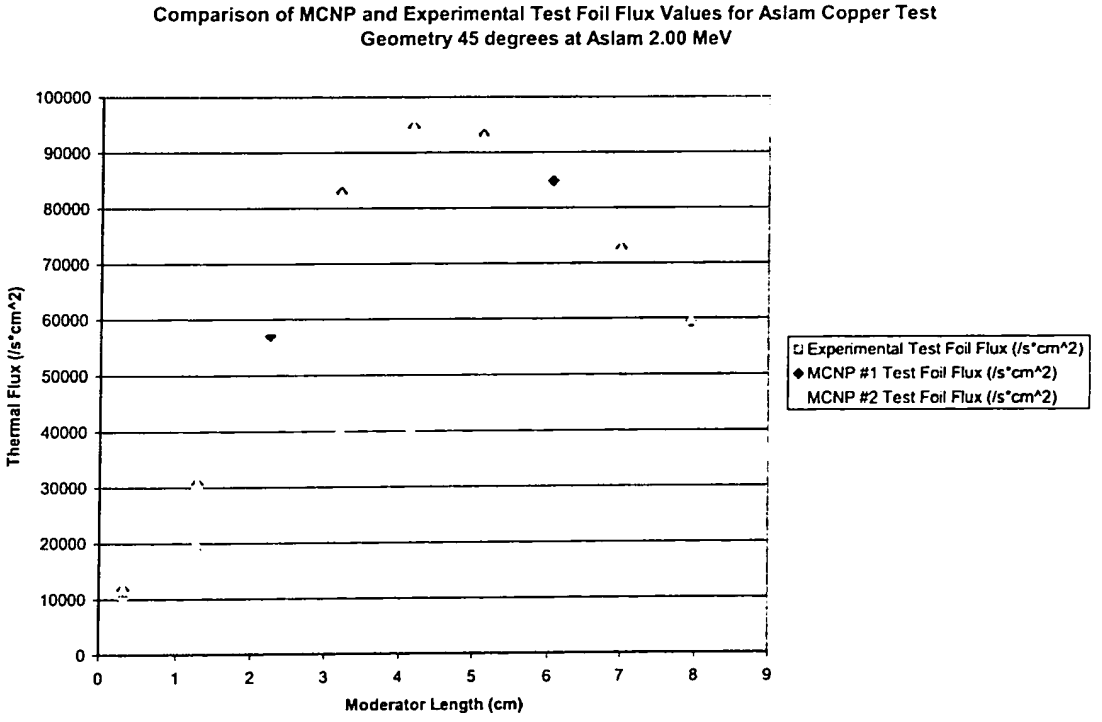

Figure 27 Graph showing experimental and MCNP5 derived test foil thermal neutron flux with increasing moderator length for 2.00 MeV protons on lithium.

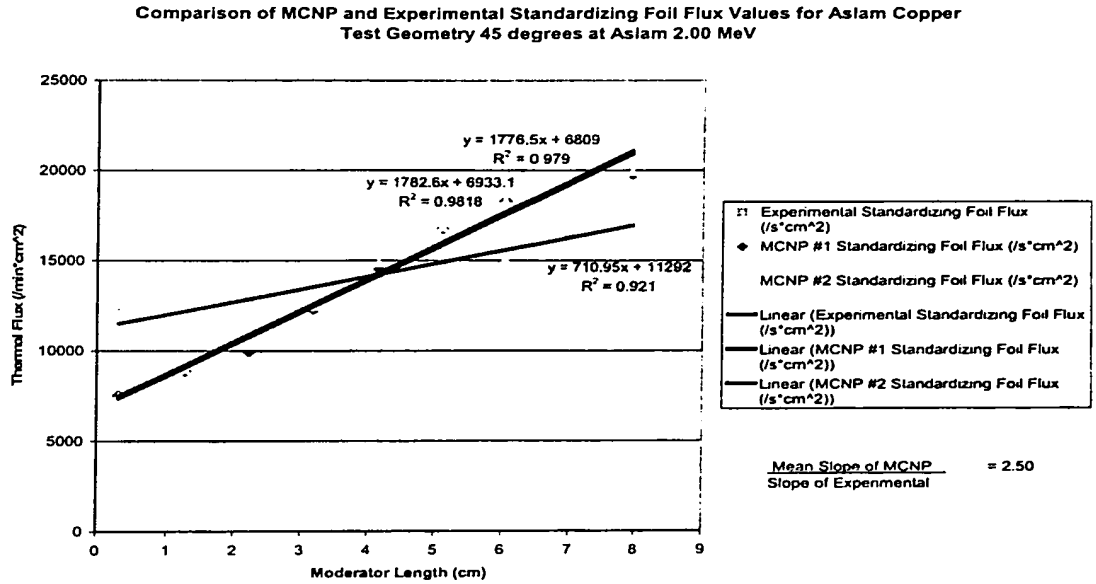

Figure 28 Graph showing experimental and MCNP5 derived standardizing foil thermal neutron flux with increasing moderator length for 2.00 MeV protons on lithium.

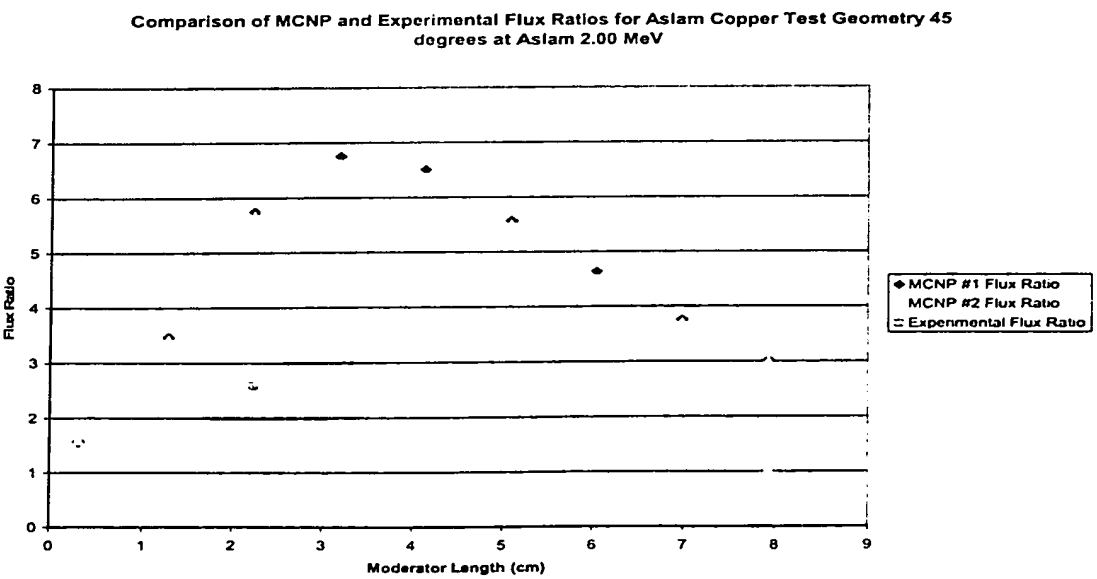

Figure 29 Graph showing experimental and MCNP5 derived test foil to standardizing foil flux ratios with increasing moderator length for 2.00 MeV protons on lithium.

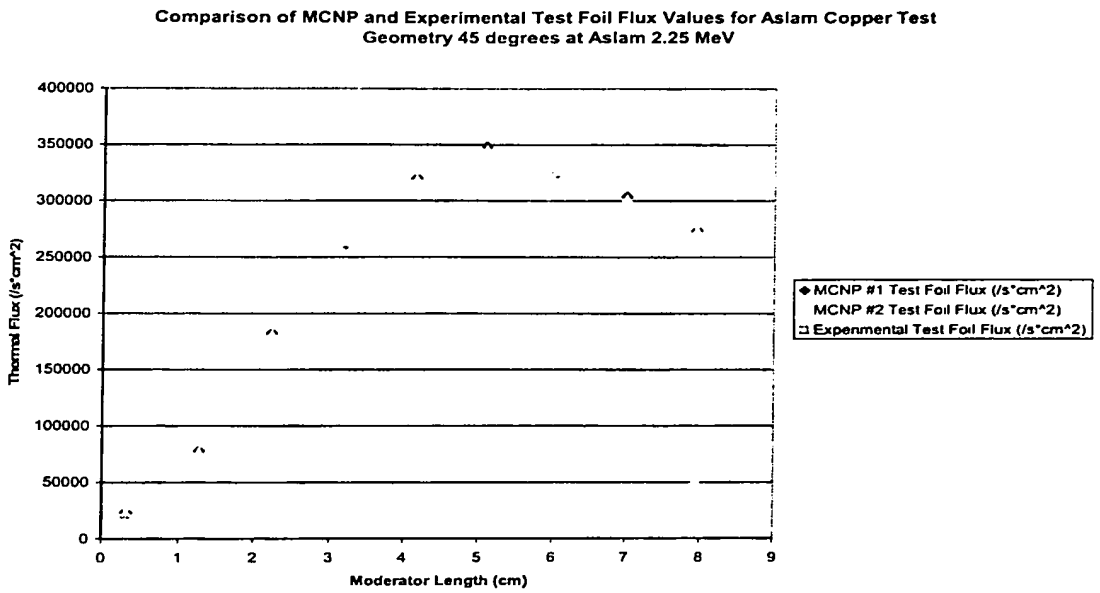

Figure 30 Graph showing experimental and MCNP5 derived test foil thermal neutron flux with increasing moderator length for 2.25 MeV protons on lithium.

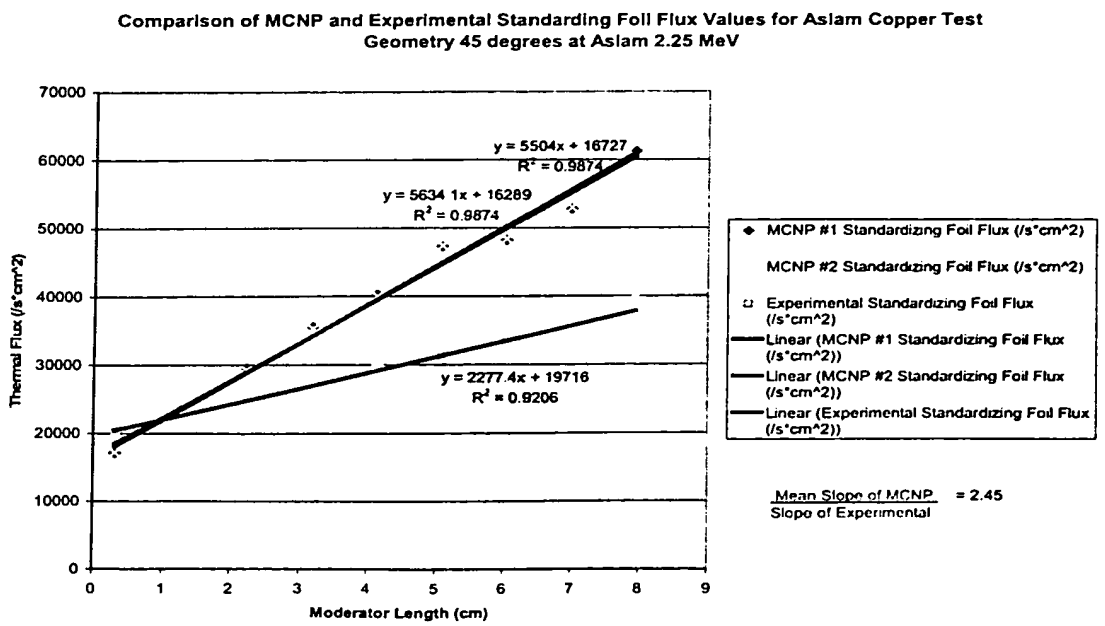

Figure 31 Graph showing experimental and MCNP5 derived standardizing foil thermal neutron flux with increasing moderator length for 2.25 MeV protons on lithium.

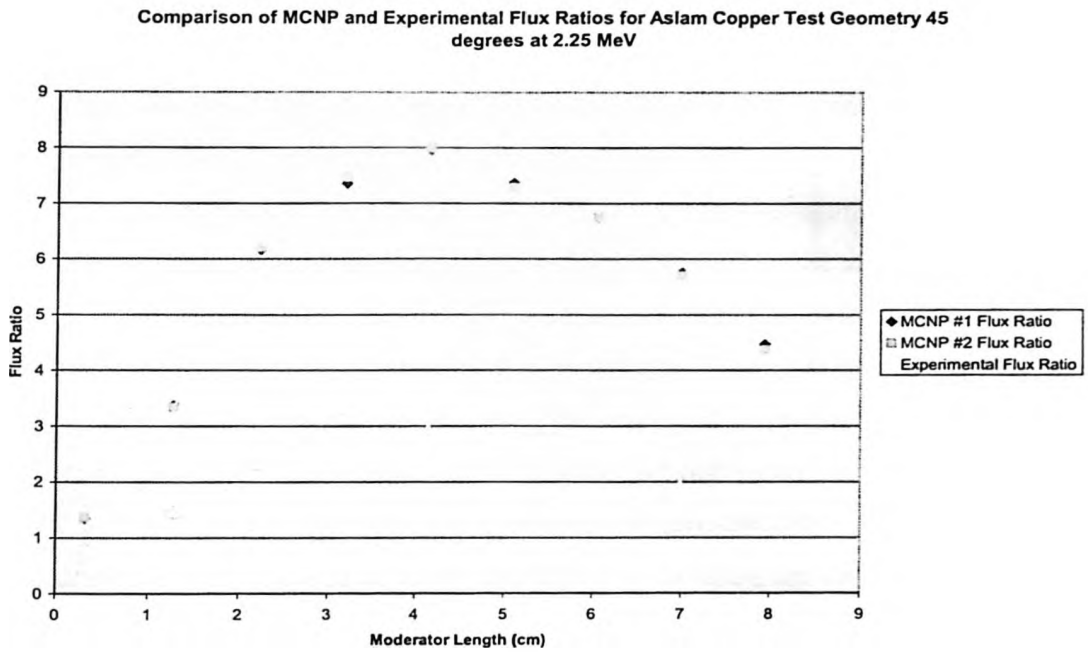

Figure 32 Graph showing experimental and MCNP5 derived test foil to standardizing foil flux ratios with increasing moderator length for 2.25 MeV protons on lithium.

Figure 27 shows that the thermal flux trend with increasing moderator length for the copper test geometry was quite similar and within a factor 3 difference; a significant improvement. The only real discrepancy was the moderator length at which the thermal flux peaked within the test foil, the difference being approximately 0.75 cm of HDPE. Fig 28 shows that both the MCNP5 and experimental standardizing foil trends increased steadily over the range of moderator length studied. This was due to the increased scattered neutron contribution to the standardizing foil with increasing moderator length. However, the slope of each trend differed in a ratio of 2.45:1 for the MCNP5 case to experimental case. The differences in these slopes could not be accounted for. HDPE is made up of principally carbon and hydrogen, whose transport properties have been well established by the Monte Carlo simulation community. Once these data were established,

the flux ratios of test foils to standardizing foils were produced. Figure 29 shows that after normalization the trends, although off by a factor of roughly 2 at the greatest point, were nearly identical. The peak thermal flux ratio occurred at the same moderator length of approximately 3.5 cm. Figures 30 through 32 show the same behavior for the 2.25 MeV neutron spectrum as for that of the 2.00 MeV neutron spectrum. Again the thermal flux peak difference was approximately 0.75 cm and the ratio of the standardizing slopes was 2.42:1 for the MCNP5 case to experimental case. The flux ratio shown in Fig. 32 again had a nearly identical trend where the peak thermal flux ratio occurred at the same moderator length of approximately 4.1 cm. The increase in this value over its 2.00 MeV counterpart of 0.6 cm is consistent with the increased maximum neutron energy of the spectrum at 45° (relative to the incident proton direction). Overall it was concluded that the phantom validation could be accomplished by normalizing the inner and surface foil flux values via a similar standardizing foil procedure. If the MCNP5 and experimental thermal flux ratio trends for both the inner and surface foils of the phantom were equivalent, the phantom composition could be deemed successfully confirmed.

4.4 New Phantom Geometry

In order to perform the phantom validation in the 45° geometry, the copper test foil and moderator (single slab) were replaced with the phantom. The phantom central axis was positioned 34 cm from the target origin (MCNP5 source origin). The standardizing foil arrangement changed slightly. The holder thickness was increased from one 1/8" HDPE slab (0.3175 cm) to four 1/8" HDPE slabs (1.27 cm). The standardizing foil was then positioned to the back face of the holder (relative to the target). The result was an increased standardizing foil activity for experimental statistical purposes, as well as to some extent prevention of low energy neutrons scattered from the phantom from contributing to the standardizing foil activity/tally. Experiments were carried out at 2.00,

2.15, and 2.25 MeV protons on lithium metal for increasing HDPE moderator thickness. Irradiations were carried out for 10 minutes. Surface foil activities were measured after 1 min cooling, followed by inner foil activities after 3.5 min cooling, followed finally by standardizing foil activities after 6 min of cooling. All foils were counted for 120 s. Simulations were carried out for the new phantom geometry as shown in Fig. 33 (next page). Source cards used were those of Arnold et al., since only source cards for 2.00 and 2.25 MeV were available from Aslam et al. Since both source card sources agreed away from the 0° vicinity, it was regarded that the source cards from Arnold et al. would reproduce the copper test geometry results attained using source cards from Aslam et al. MCNP5 geometries modeled included the phantom with copper foils, moderator, holder with standardizing foil, long counter, and SNOOPY remmeter. Also modeled but not shown in Fig. 33 were three walls within the irradiation room. The two concrete walls in proximity to the long counter were modeled, as well as a wall close to the SNOOPY. All walls were modeled to a depth of 150 cm and height of 400 cm. The walls were positioned such that their outer faces distanced the critical targets to the same extent as in reality. Figures 34 through 36 show comparisons for MCNP5 and experimental data for surface, inner, and standardizing foils with increasing moderator length for 2.00 MeV protons. Figures 37 through 39 show the corresponding data for 2.15 MeV protons, while Fig. 40 through 42 shows that of 2.25 MeV protons on lithium.

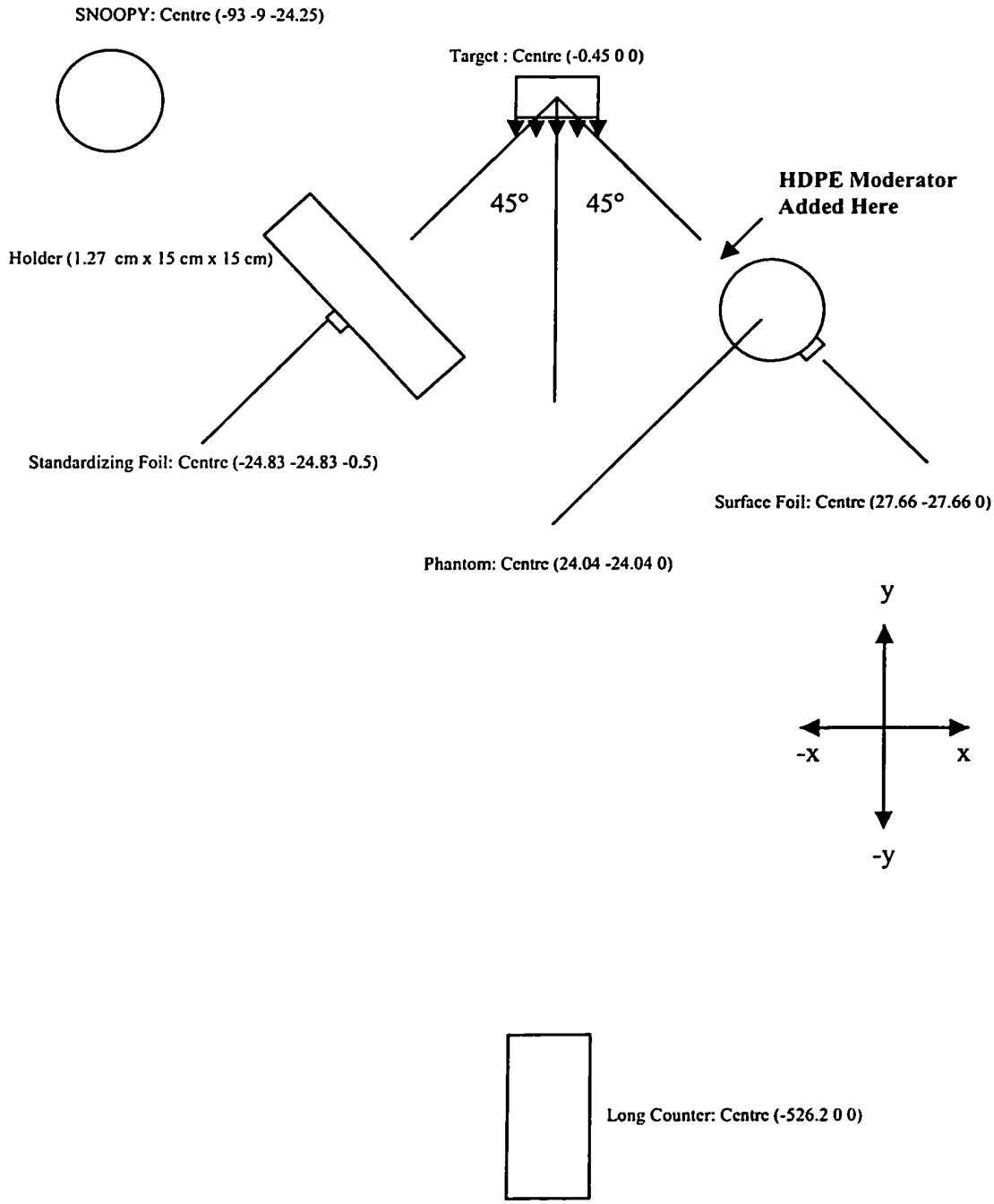

Figure 33 Bird's eye view of experimental irradiation room and setup for New Phantom Geometry. All positions are relative to MCNP coordinate system and are in units of centimeters. N.B. Diagram not to scale.

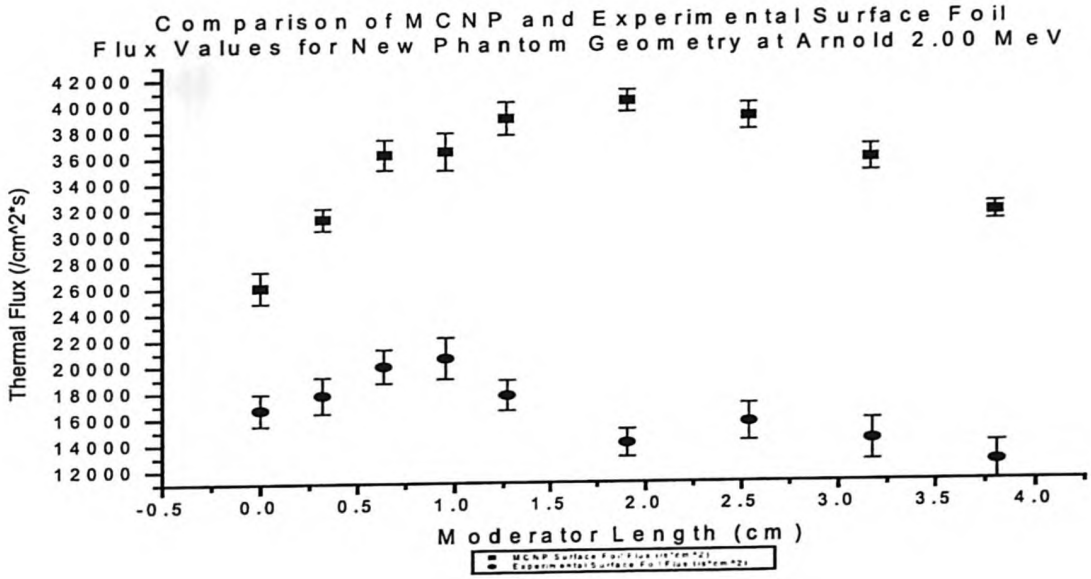

Figure 34 Graph showing experimental and MCNP5 derived surface foil thermal neutron flux with increasing moderator length for 2.00 MeV protons on lithium.

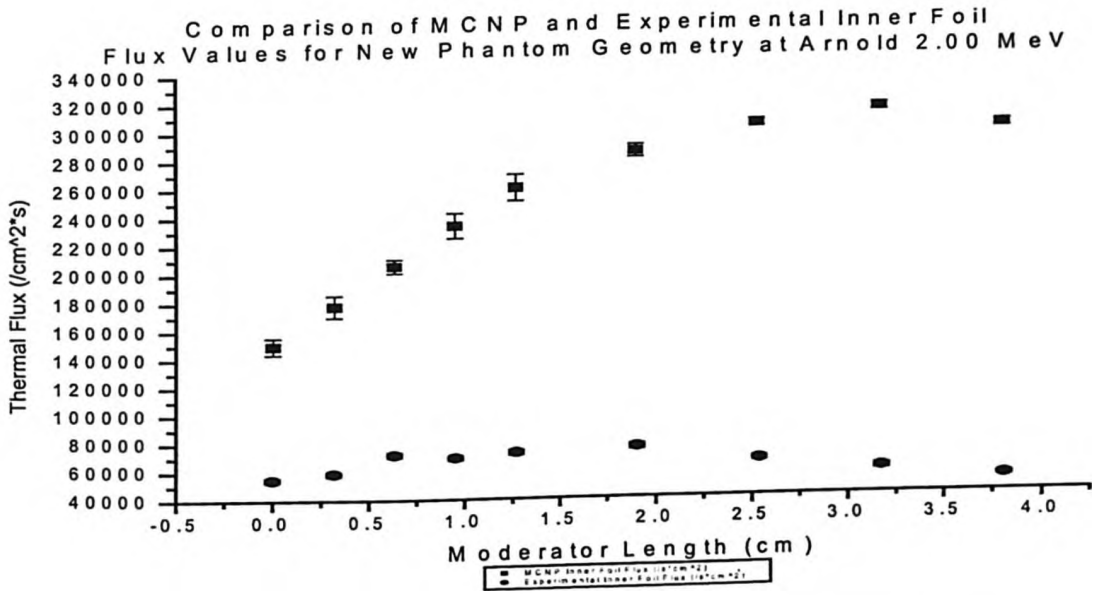

Figure 35 Graph showing experimental and MCNP5 derived inner foil thermal neutron flux with increasing moderator length for 2.00 MeV protons on lithium.

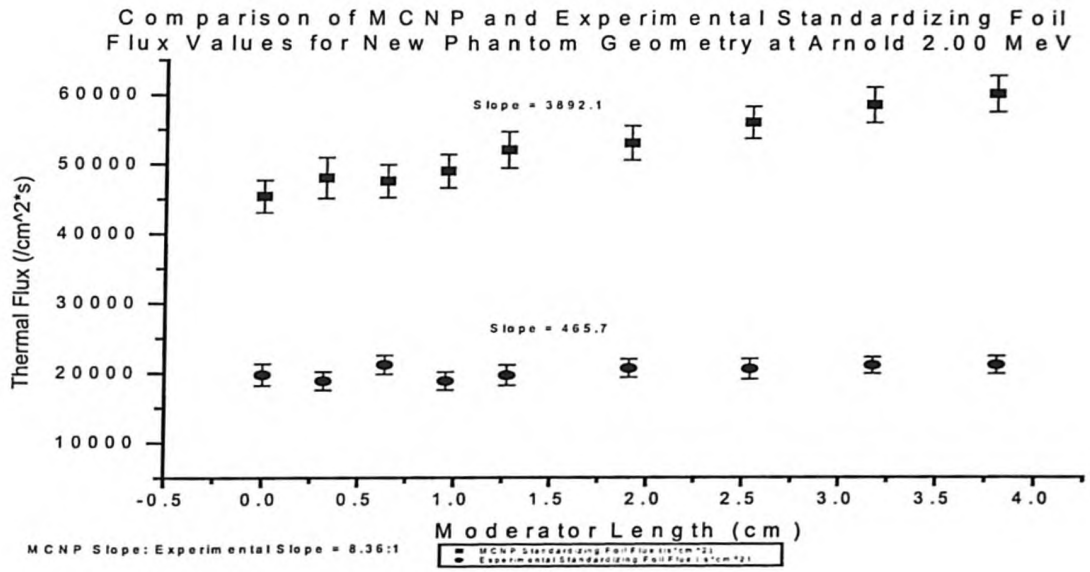

Figure 36 Graph showing experimental and MCNP5 derived standardizing foil thermal neutron flux with increasing moderator length for 2.00 MeV protons on lithium.

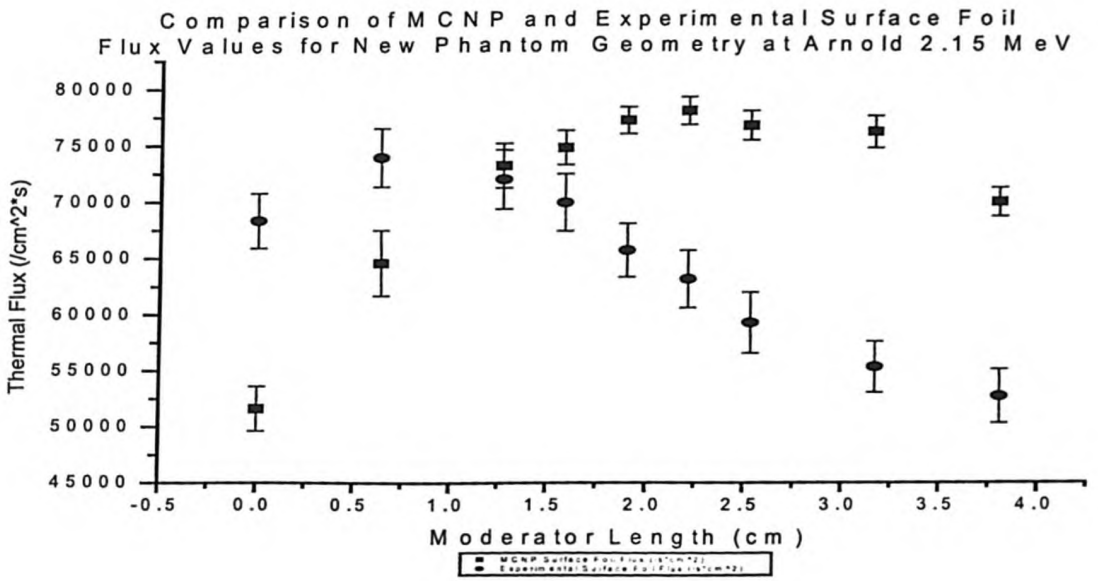

Figure 37 Graph showing experimental and MCNP5 derived surface foil thermal neutron flux with increasing moderator length for 2.15 MeV protons on lithium.

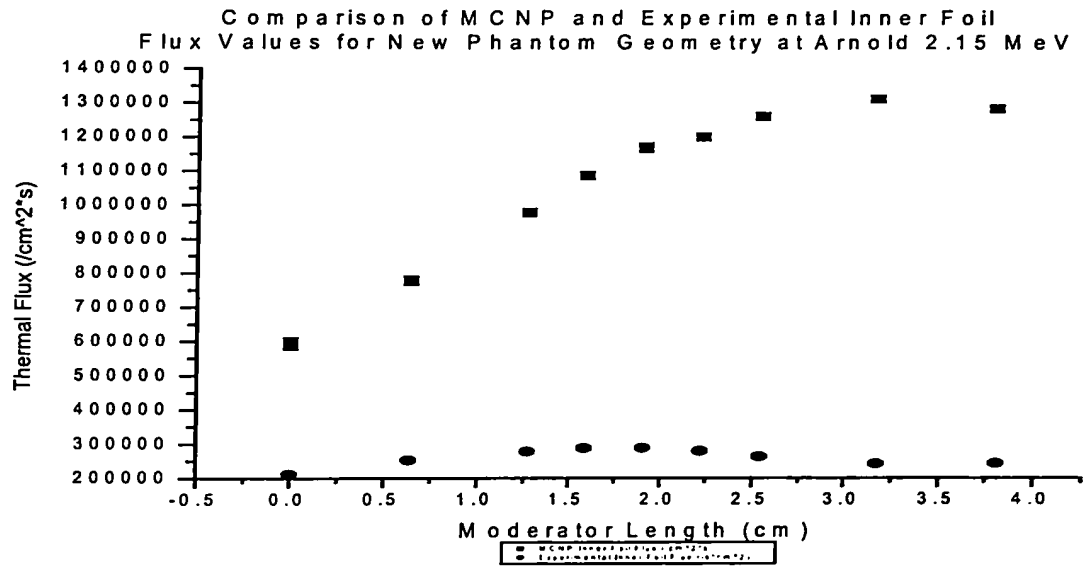

Figure 38 Graph showing experimental and MCNP5 derived inner foil thermal neutron flux with increasing moderator length for 2.15 MeV protons on lithium.

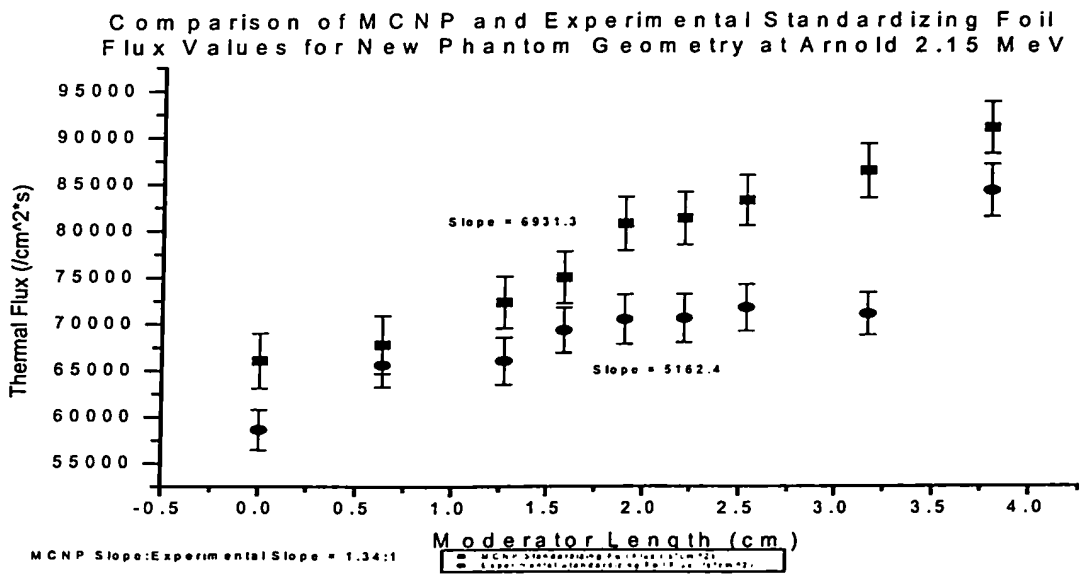

Figure 39 Graph showing experimental and MCNP5 derived standardizing foil thermal neutron flux with increasing moderator length for 2.15 MeV protons on lithium.

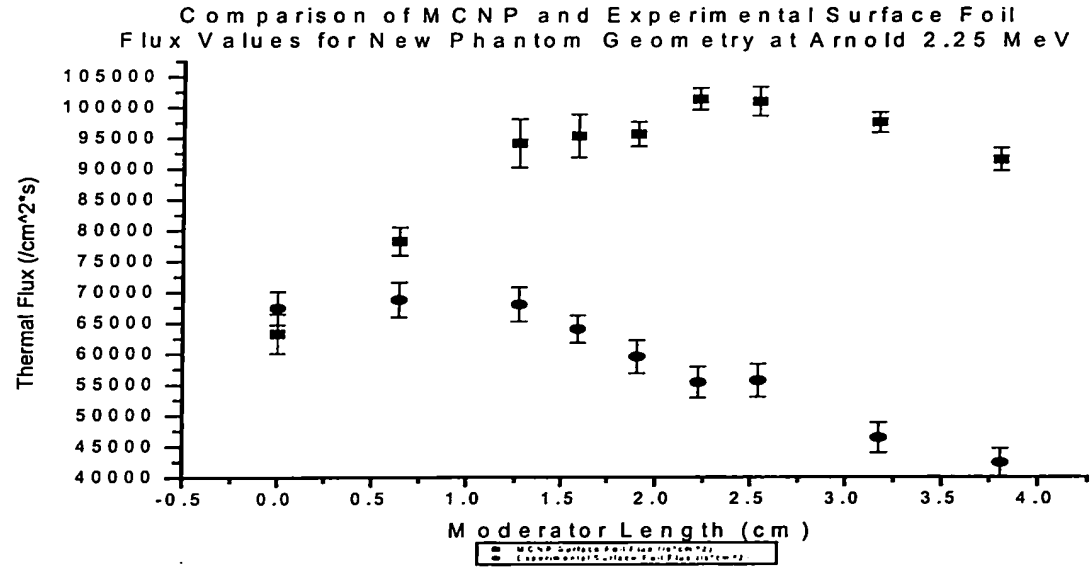

Figure 40 Graph showing experimental and MCNP5 derived surface foil thermal neutron flux with increasing moderator length for 2.25 MeV protons on lithium.

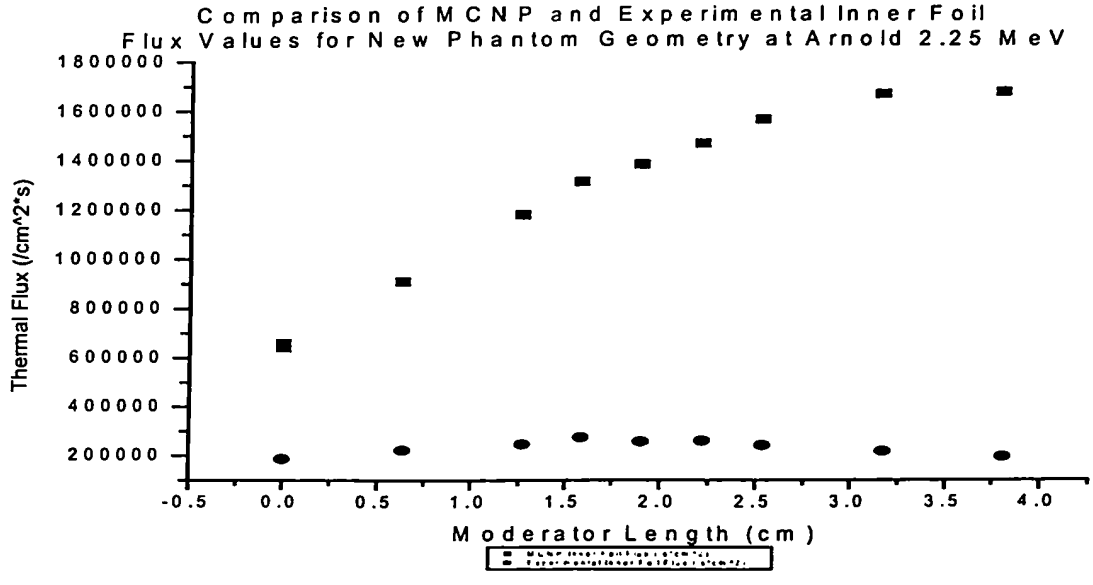

Figure 41 Graph showing experimental and MCNP5 derived inner foil thermal neutron flux with increasing moderator length for 2.25 MeV protons on lithium.

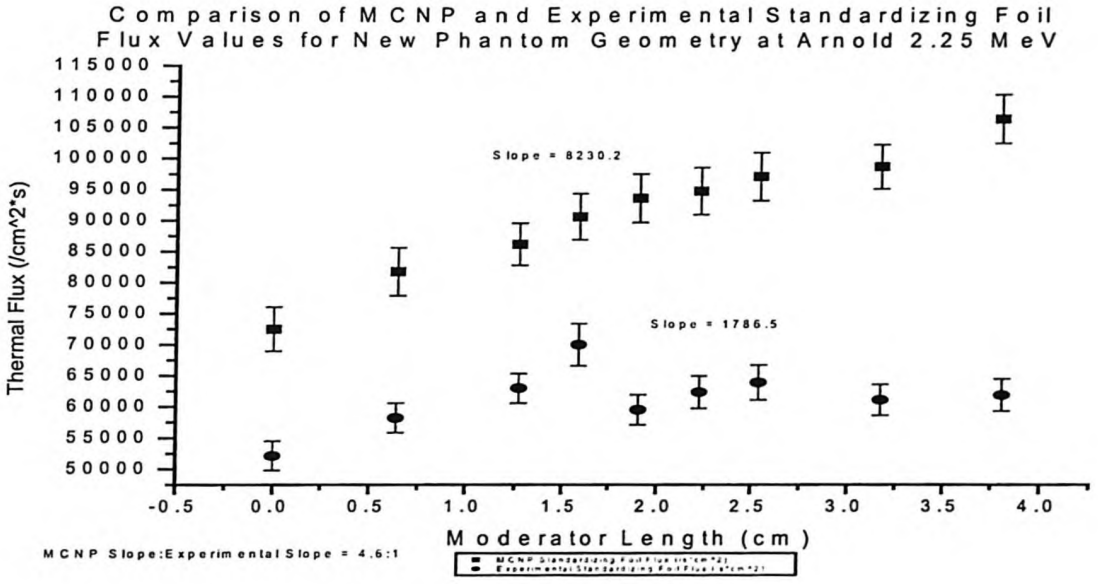

Figure 42 Graph showing experimental and MCNP5 derived standardizing foil thermal neutron flux with increasing moderator length for 2.25 MeV protons on lithium.

Although Fig. 34 shows that the thermal neutron flux at the back surface of the actual phantom exhibits a somewhat similar trend to that modeled, Fig. 35 clearly shows that this is not the case for the thermal neutron flux in the vicinity of the inner cavity. The peak moderator length difference for 2.00 MeV is approximately 0.75 cm for the surface foils and approximately 1.5 cm for the inner foils. The factor difference for the maximum thermal flux values of the surface foils is 1.96. The factor difference for the maximum thermal flux values for the inner foils is 4.17. Both values are within the factor of 7 MCNP to experimental factor difference in the literature. The standardizing foil thermal flux showed the same steadily increasing thermal flux trend with increasing moderator length, as seen in the copper test geometry. This, as for the copper test geometry case, was due to the increased scattered neutron contribution to the standardizing foil activity with added HDPE moderator in front of the phantom. The discrepancy at 2.00 MeV in the ratio of the slope of MCNP5 and experimental trends was greater than for the copper

test geometry at 8.36. Since the holder geometry was changed slightly for the new phantom geometry it was difficult to state clearly whether this increased slope ratio was due to phantom neutron outscatter or whether it was due to significantly different particle transport within the holder itself for the MCNP5 case versus that in reality.

The 2.15 MeV comparisons show somewhat differing trends than for 2.00 MeV. Whereas for 2.00 MeV protons on lithium the surface foil fluxes showed similar trends for MCNP5 and experiment, Fig. 37 shows that this was clearly not the case for 2.15 MeV protons. The 2.15 MeV inner foil and standardizing foil cases did, however, show similar results as their 2.00 MeV counterparts. The ratio of MCNP5 to experimental slopes for the 2.15 MeV standardizing foils was much lower at 1.34. The peak moderator length difference for 2.15 MeV is approximately 1.75 cm for the surface foils and approximately 1.5 cm for the inner foils. The factor difference for the maximum thermal flux values of the surface foils is 1.06. The MCNP5 value range was thus in excellent agreement with the experimental range. However, the factor difference for the maximum thermal flux values for the inner foils is 4.55. This was nearly the same as the for the 2.00 MeV case. The contradiction between the agreement for the surface foils and the discrepancy for the inner foils was attributed to inscattered neutrons from the wide moderator slabs to the surface foils and is discussed in detail below.

Figures 40, 41, and 42 show nearly the same trends and values for the 2.25 MeV case as for the 2.00 MeV case. The discrepancy at 2.25 MeV in the ratio of the slope of MCNP5 and experimental trends was in between that of the 2.00 MeV and 2.25 MeV cases at a value of 4.6. The factor difference for the maximum thermal flux values of the surface foils is 1.47. The factor difference for the maximum thermal flux values for the inner foils is 6.11. The peak moderator length difference for 2.25 MeV is approximately 1.75 cm for the surface foils and approximately 1.75 cm for the inner foils. It is apparent that these peak moderator length differences increased with increasing incident proton energy. Figures 43 and 44 show that theoretically both the total thermal neutron yield and

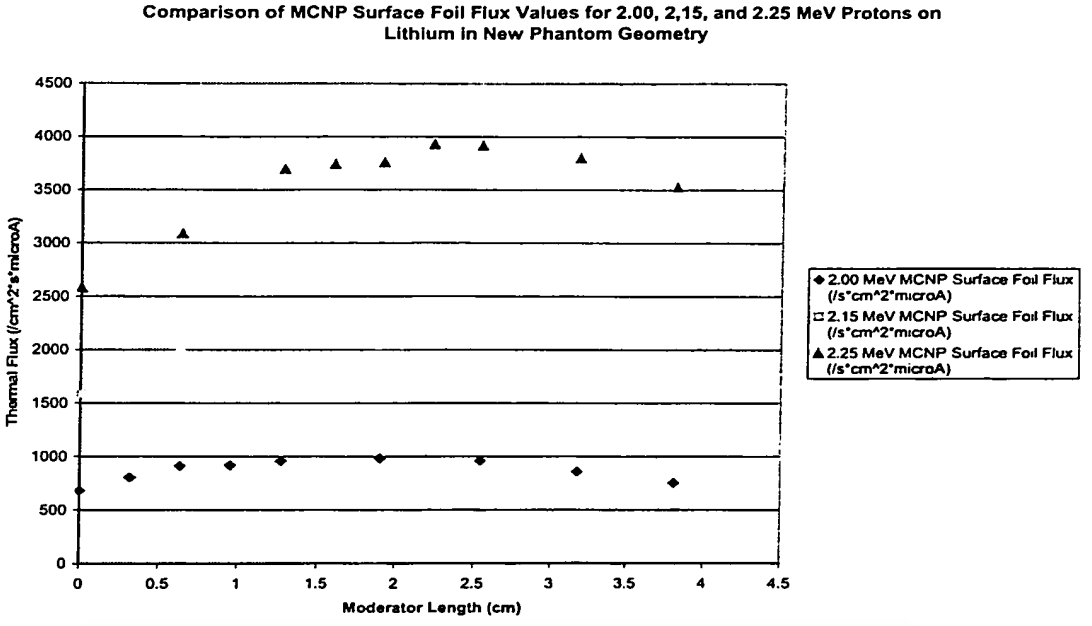

Figure 43 Graph showing MCNP5 surface foil thermal neutron flux with increasing moderator length for 2.00, 2.15, and 2.25 MeV protons on lithium.

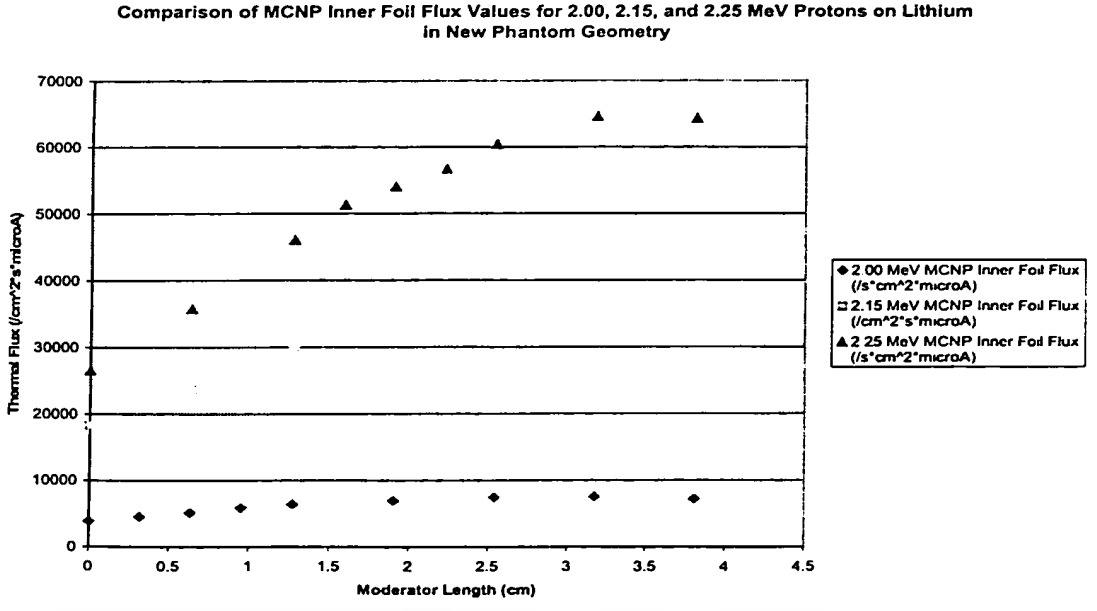

Figure 44 Graph showing MCNP5 inner foil thermal neutron flux with increasing moderator length for 2.00, 2.15, and 2.25 MeV protons on lithium.

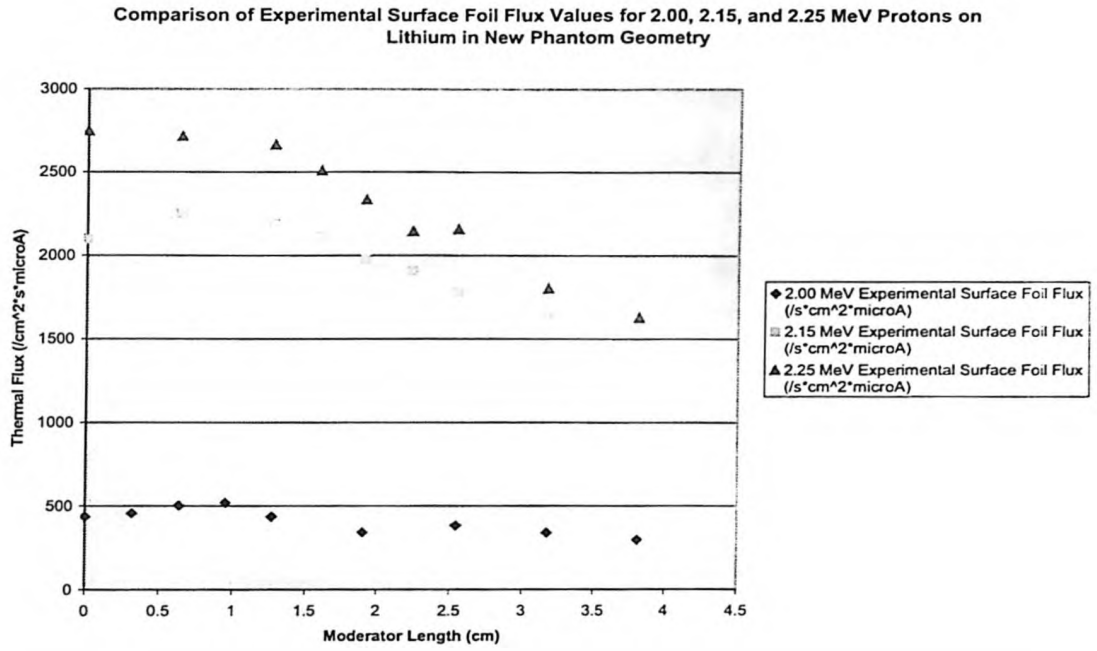

Figure 45 Graph showing experimental surface foil thermal neutron flux with increasing moderator length for 2.00, 2.15, and 2.25 MeV protons on lithium.

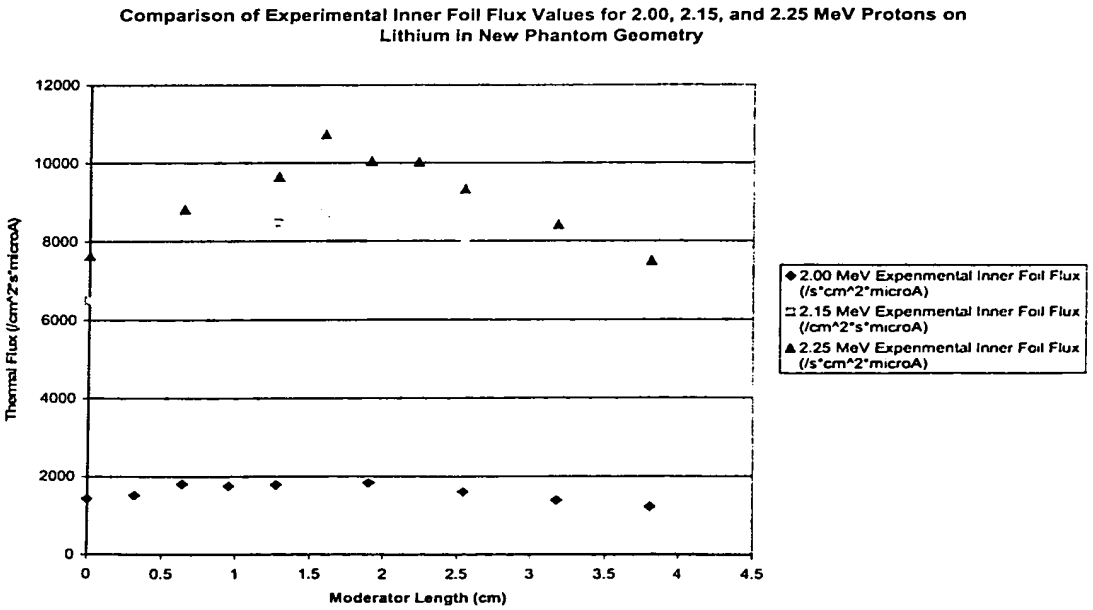

Figure 46 Graph showing experimental inner foil thermal neutron flux with increasing moderator length for 2.00, 2.15, and 2.25 MeV protons on lithium.

thermal neutron peak moderator thickness increase with increasing energy, for both surface and inner cases. Note that the values presented in these graphs have been normalized per microampere. As can be seen from Fig. 45 and 46, experimentally this does not occur. Both the 2.15 and 2.25 MeV cases show similar trends for surface and inner foils. Also, only a slight increase in thermal neutron yield is afforded by increasing the energy from 2.15 to 2.25 MeV protons. Since increasing the incident proton energy in turn increases the maximum neutron energy, if human tissues transport neutrons in a similar manner to the phantom, it would not be desirable to use 2.25 MeV protons over 2.15 MeV protons. The reasoning behind this is that the faster neutrons have a higher LET and, therefore, a higher dose contribution.[53] Such unnecessary dose is to be avoided whenever possible when utilizing ionizing radiation treatments.

As discussed above for the copper test geometry, in order to validate the phantom the inner and surface foil flux ratios (with the standardizing foils) must be compared with those of the MCNP5 simulations. As can be seen from Fig. 47 and 48, neither the inner

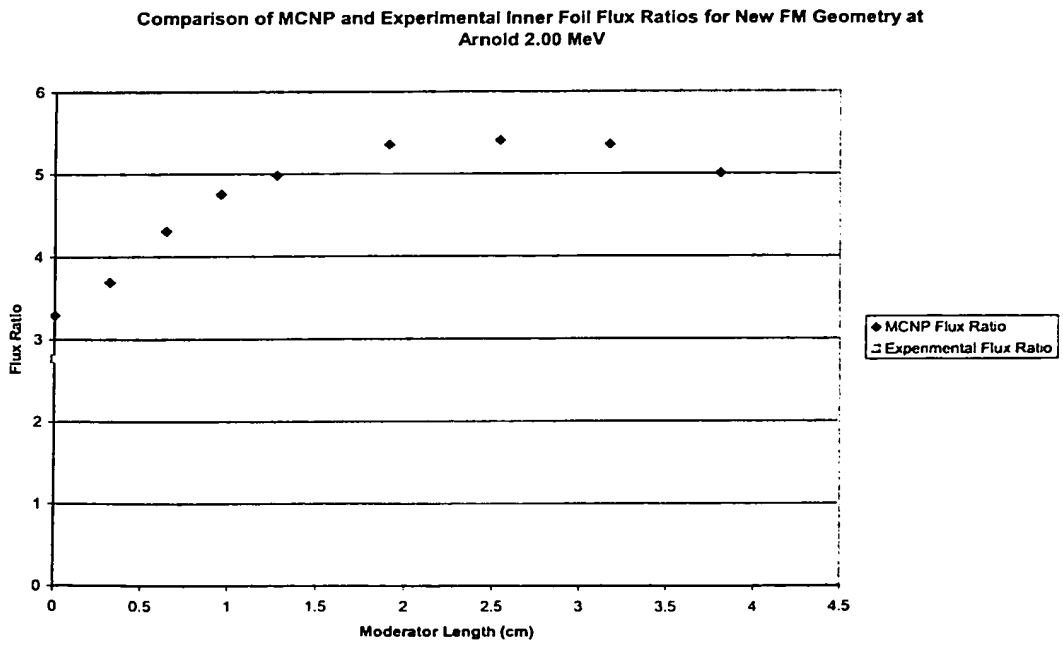

Figure 47 Graph showing MCNP5 and experimental inner foil flux ratios with increasing moderator length for 2.00 MeV protons on lithium.

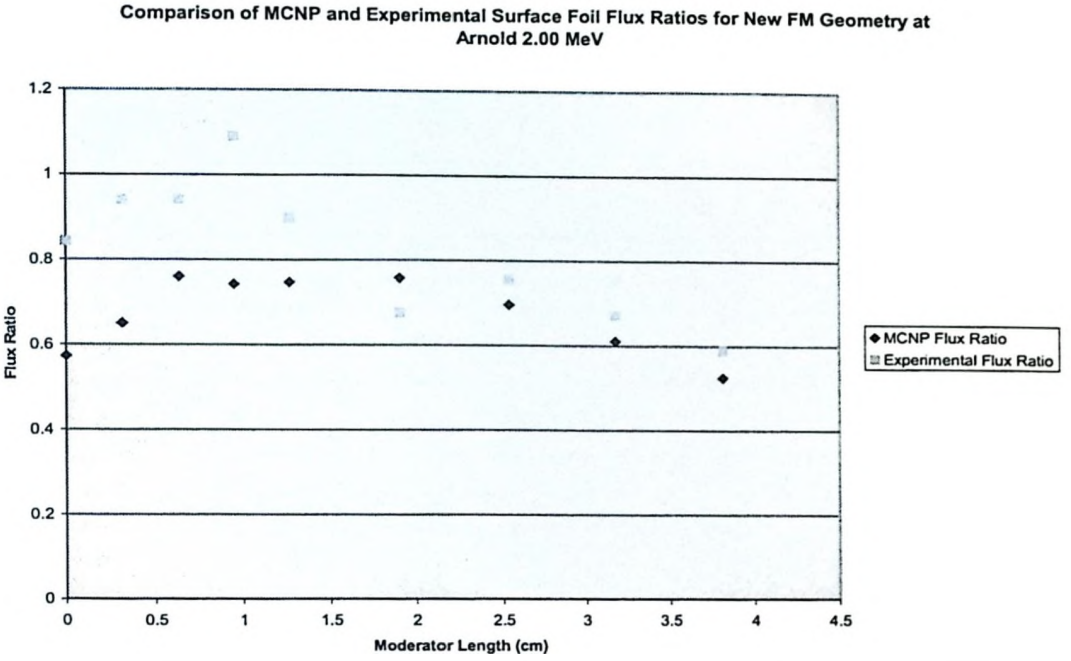

Figure 48 Graph showing MCNP5 and experimental surface foil flux ratios with increasing moderator length for 2.00 MeV protons on lithium.

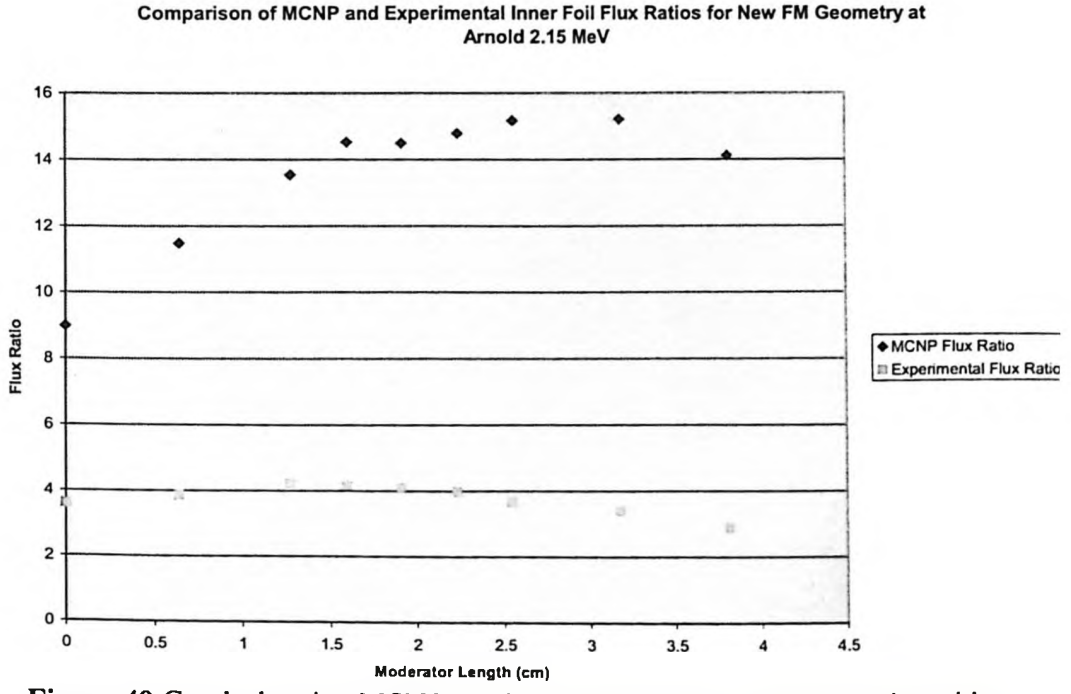

Figure 49 Graph showing MCNP5 and experimental inner foil flux ratios with increasing moderator length for 2.15 MeV protons on lithium.

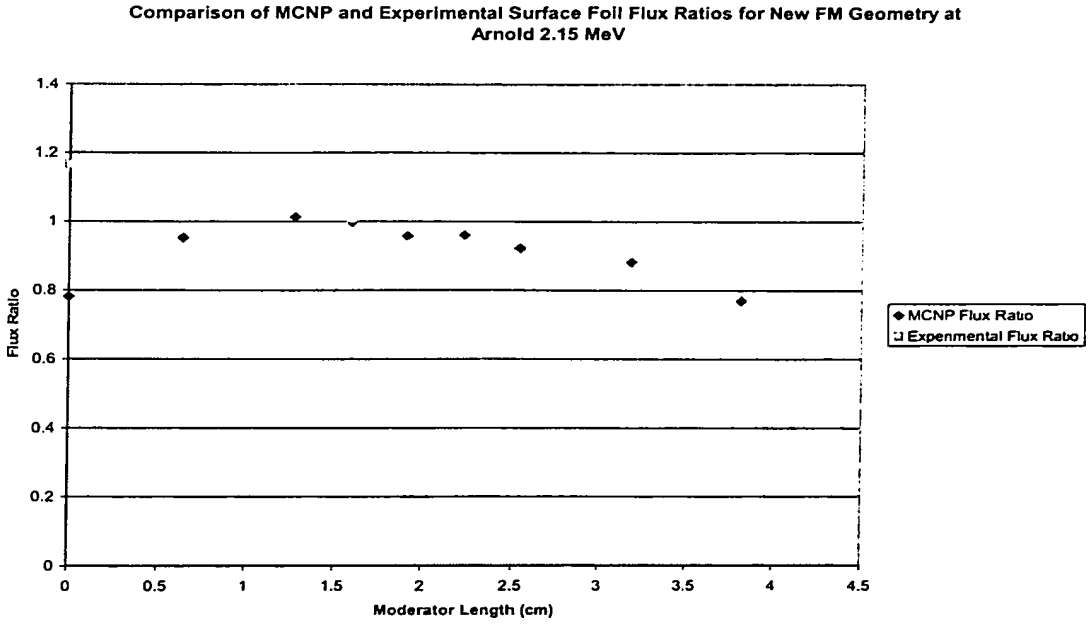

Figure 50 Graph showing MCNP5 and experimental surface foil flux ratios with increasing moderator length for 2.15 MeV protons on lithium.

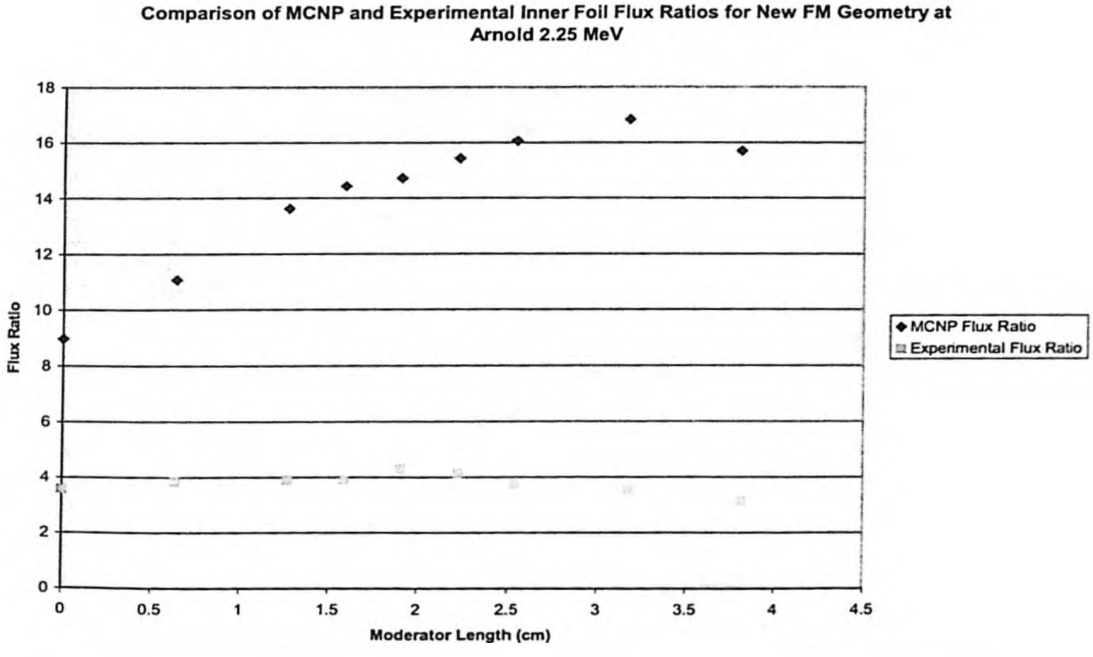

Figure 51 Graph showing MCNP5 and experimental inner foil flux ratios with increasing moderator length for 2.25 MeV protons on lithium.

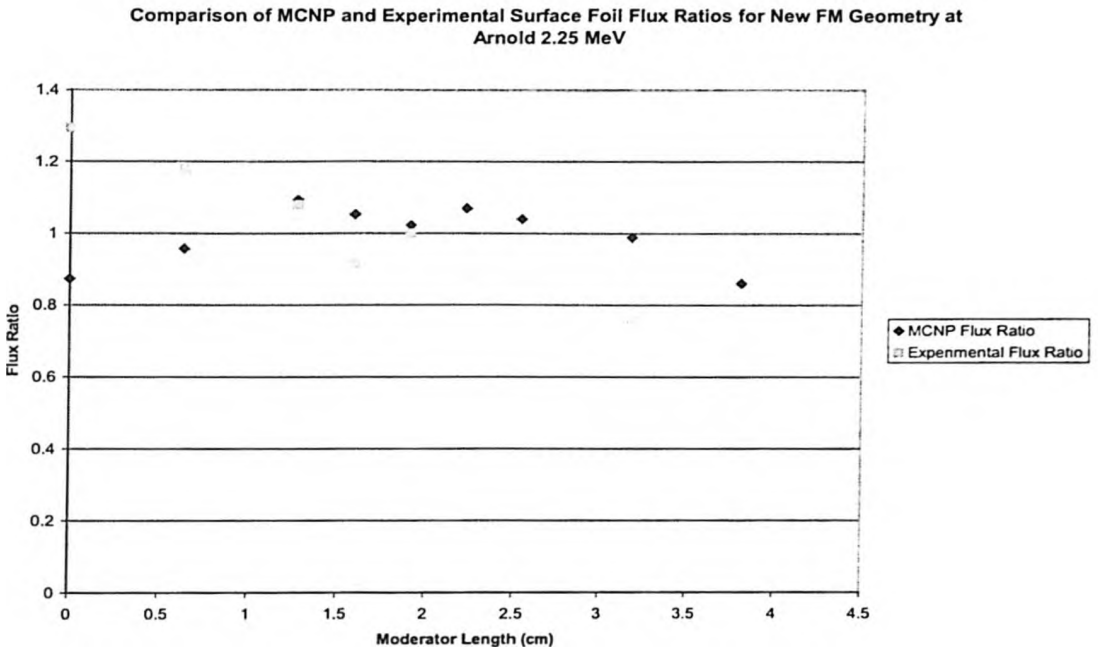

Figure 52 Graph showing MCNP5 and experimental surface foil flux ratios with increasing moderator length for 2.25 MeV protons on lithium.

foil flux ratio nor surface foil flux ratio show the same trends between simulation and experiment at 2.00 MeV. In the case of the surface foil flux ratio graph, Fig. 48, the experimental ratio has higher values than the MCNP5 values for the first half of moderation. The same trends can be seen in Fig. 49 and 50 for 2.15 MeV and Fig. 51 and 52 for 2.25 MeV. The inner foil flux ratios differ to a greater extent than the surface foil flux ratios with increasing proton energy. As can be seen from Fig. 48, 50, and 52 the surface foil flux ratios agree relatively well through all proton energies through the latter half of moderation. This is likely attributed to the scattered neutron component from the wide moderator slabs at high moderator lengths. As the moderator thickness increases to roughly 2 cm, the total moderation length to line-of-sight (directly from the source) neutrons to the surface foil is roughly 12 cm, assuming the HDPE and phantom materials have somewhat similar moderating properties. Such a large amount of moderation may be more than enough to over-moderate the line-of-sight neutrons to a negligible quantity. Due to the cylindrical shape of the phantom, the surface foil can accept neutrons that

have inscattered via the wide moderator slabs with minimal moderation. This is not the case with the inner foils, since only low energy neutrons will be scattered towards the inner foil at such a great angle of scatter. These low energy neutrons scattered toward the inner foils via the wide moderator slabs are likely to be over-moderated and not contribute to the inner foil flux. A diagram of this scenario is presented in Fig. 53 below.

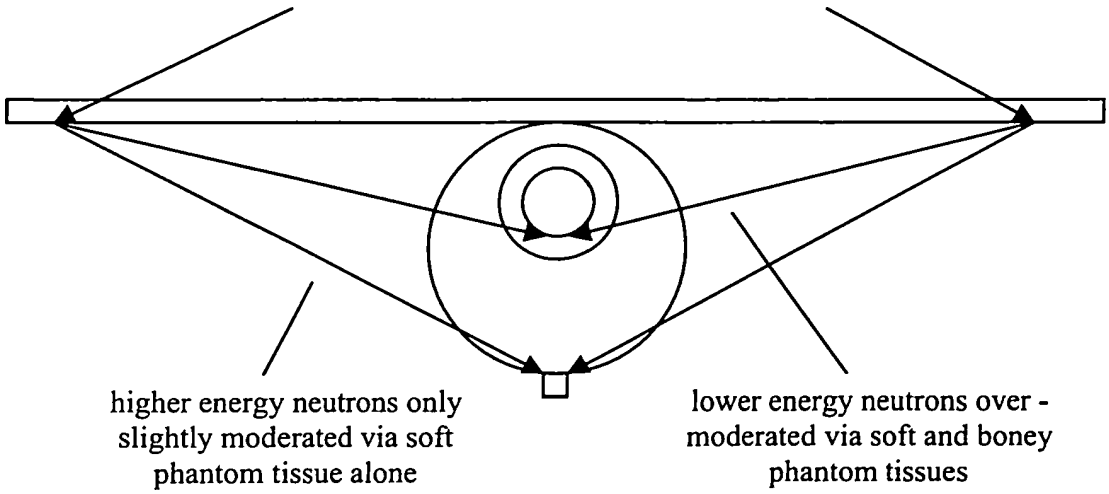

Figure 53 Cross sectional view of phantom at midplane showing the scattered neutron contribution to both inner foil and surface foil from wide HDPE slabs. N.B. Diagram not to scale.

All data presented leads to the conclusion that the simulated phantom does not behave as the actual phantom measured. Several factors could have attributed to the difference, mostly with respect to the phantom manufacture. In all cases the phantom composition inputted into MCNP5 underestimates the moderation of the neutron flux. Despite the apparent homogeneity of the polyester resin/crushed salt combination during mixing; this may not have been the case. Mixing was performed for several minutes with a wooden spoon until the combination appeared homogeneous. Ideally in order to create a homogeneous mixture, a mixing device which creates a vortex, such as a paint mixer,

should be used. As described in Chapter 2, polyester resin is the sole ingredient of the phantom that contains hydrogen in its molecular make up. Since the action of neutron moderation is principally caused by hydrogen, the evidence of a decreased neutron flux in the vicinity of the foils implies that there was a greater abundance of polyester resin versus crushed salt than expected. This may have occurred wherein the crushed salt settled to the bottom of each phantom piece (which would become the distal ends of the phantom relative to the midplane). Another possible cause of inconsistency is the composition of the resin itself. The composition of the resin was derived from the repeating molecular structure as shown in Fig. 6 of Chapter 2. Although assumed negligible, polyester resin contains quantities of styrene and alkyl peroxides which create the branches to the repeating molecular structure, solidifying the resin. Styrene is composed of approximately 92.26% carbon and 7.74% hydrogen by weight. This hydrogen content is nearly 3% greater than that of the repeating polymer molecule. The styrene content of polyester resin can range from 0% to 60%, typically 35-45%.[31] The manufacturer of the resin did not list resin composition on the container as it is likely a proprietary composition. As mentioned in Chapter 2, an excess of peroxide catalyst was added to harden the boney tissue resin mixture, due to the severe alteration of the mixture upon salt addition. If the alkyl group of the peroxide was of significant length, the hydrogen abundance in the phantom would have been greater than expected. Finally, although the density of the phantom was derived from the additions presented in Tables 1 and 2 of Chapter 2, a true mass-volume measure of the phantom tissue densities would need to be performed on samples from the phantom soft and boney tissues, at minimum. Ideally, a pycnometer would be used on the samples to determine the tissue densities, followed by neutron activation analysis at the MNR PGNAA facility to determine a more accurate phantom soft and boney tissue composition.

Chapter 5. Conclusions and Future Considerations

5.1 Conclusions

After rearrangement of the original experimental setup as per Fig. 18 of Chapter 3 to a more suitable one (Fig. 33), phantom validation was undergone. The simulated phantom data deviated from the experimental phantom data for both surface and inner foil cases. The surface foils agreed to some extent, however, this was attributed to contributions from inscattered neutrons from the wide moderator slabs. The inner foil flux ratios with the standardizing foils showed that in the vicinity of the cavity the thermal flux trend with moderator length peaked with less moderation experimentally than simulated. The peak moderator length difference for the inner foils varied from 1.5 cm to 1.75 cm for 2.00 MeV protons to 2.25 MeV protons. This increase was attributed to the increase in maximal neutron energy with increasing incident proton energy. The difference in thermal flux peak moderation showed that the phantom was moderating to a greater extent than expected. Since hydrogen is the most efficient moderating element, the differences between the actual phantom and its simulated counterpart was likely due to a discrepancy in the hydrogen content of either the phantom soft tissue, boney tissue, or both. Several sources for the inconsistencies were cited, from phantom manufacture inadequacies to the unknown polyester resin composition.

Neutron beam line characterization of the 3 MV KN accelerator at MAL was also performed. After comparing two Monte Carlo source card sources, it was determined that a discrepancy was present between the two sources for both 2.00 MeV protons and 2.25 MeV protons in the 0° region relative to the incident proton direction. This difference was attributed to variations between the algorithms used to produce the source cards.

Both Aslam et al. and Arnold et al. showed consistent results at 38.2° relative to the incident proton direction. At 45° (relative to the incident proton direction) the MCNP5 and experimental thermal flux ratio trends of the copper test geometry were similar for both 2.00 MeV and 2.25 MeV protons on lithium. Since the trends followed the same pattern, this geometry was used for the phantom validation. However, there was a factor of greater than 2.4 difference between the thermal flux ratio peak values of the MCNP5 data and the experimental data. This factor difference could not be accounted for.

5.2 Future Considerations

In order to produce a phantom that mimics neutron transport properties of human tissue for the purpose of BNCS studies, materials of well known composition and density should be used. This might be performed successfully with a similar polyester resin as that used in this study, if the composition of the resin is attained and proper preparation techniques used. Although not made specifically for neutron applications, the use of A-150 Soft Tissue Equivalent Plastic and B-100 Bone Tissue Equivalent Plastic as phantom materials should be investigated. A simple Monte Carlo simulation comparison could be performed with a similar phantom geometry for these tissue equivalent plastics and human soft tissue and bone tissue. If the two phantom types correlate well, the use of these materials for a phantom would be warranted. Finally, by combining multiple layers created separately, a phantom made of paraffin wax as the major material component may work well. The advantage of using the paraffin wax would avoid the unnecessary use of excess peroxide catalyst as was the case with the polyester resin.

The experimental and MCNP5 thermal flux values for the new phantom geometry and copper test geometry were within the factor of 7 difference reported in the literature. In order to perform BNCS treatment on humans the difference should ideally be less than 5%. The large difference between the simulated and measured quantities is due to the

difference between the theoretical neutron yields per microampere proton current and the actual neutron yields per microampere proton current. Target oxidation and melting are the primary causes of these inconsistencies. Although it is not possible to directly measure the actual neutron yield, a figure of merit in air may be determined by using the SNOOPY remmeter. By measuring the ^{7}Be activity of the lithium target after short irradiation time, the effective neutron yielding proton current could be determined. The SNOOPY response could be plotted against this data for multiple "effective" proton currents at a given SNOOPY position. During future irradiations the SNOOPY response could then be correlated to the effective proton current. The correlating sets would be arrived at using fresh lithium targets for each proton current used. This procedure would then be repeated for each incident proton energy of interest.

Finally, although the phantom position for this study was selected to be 45° relative to the incident proton direction, ideally irradiations for BNCS should be performed at 0°. The peak neutron yield at the 0° position for the copper test geometry was more than 12 times greater than the peak neutron yield at the 38.2° position. This large increase in yield with respect to position should be exploited to decrease the treatment time for BNCS. However, the discrepancies between the source cards of Aslam et al. and Arnold et al. should be alleviated. Since both source cards are derived from Fortran algorithms using experimental data, an alternative source card set could be created using Monte Carlo simulations. By modeling the target geometry and initializing a unidirectional proton beam, tracking of produced neutrons and tallying at various positions in space could accomplish source card compilation. An advanced charged particle transport code such as MCNPX or GEANT would have to be utilized to perform this task. Comparisons of this data with those of Arnold et al. and Aslam et al. could indicate which set, if either, is a good representation of the actual angular neutron spectrum.

References

1. Gary S. Firestein, "Rheumatoid Arthritis." Kelley's Textbook of Internal Medicine, 4th Ed. edited by David H. Humes et al., Philadelphia: Lippincott, Williams, and Wilkins, p. 1347-1359 (2000)
2. David M. Lee and Michael E. Weinblatt, "Rheumatoid arthritis." The Lancet. Vol. 358, p. 903-911 (2001)
3. Gary S. Firestein, "Rheumatoid Arthritis." Kelley's Textbook of Rheumatology, 7th Ed. edited by E. D. Harris et al, Elsevier Saunders, p. 996-1100 (2005)
4. Ernest H. S. Choy and Gabriel S. Panayi, "Mechanisms of Disease: Cytokine Pathways and Joint Inflammation in Rheumatoid Arthritis." New England Journal of Medicine. Vol. 344, p. 907-916 (2001)
5. J. C. Yanch et al., "Boron neutron capture synovectomy: Treatment of rheumatoid arthritis based on the $^{10}B(n,\alpha)^{7}Li$ nuclear reaction." Medical Physics. Vol. 26, p. 364-375 (1999)
6. Carol Eustice and Richard Eustice, "The Facts of Corticosteroids." Your Guide to Arthritis @ About.com Accessed December 18, 2003 (visit http://arthritis.about.com/cs/steroids/a/corticosteroids.htm)
7. F. Marques et al., "Symposium on radioactive colloids in the treatment of arthritis," Annals of the Rheumatic Diseases. Vol. 32, (suppl.):3-9 (1973)
8. M. Oka, "Radiation synovectomy of the rheumatoid knee with Yttrium 90." Annals of Clinical Research. Vol. 7, p. 205-210 (1975)
9. H. Deckart et al., "Radiosynovectomy of the knee-joint with ^{198}Aucolloid, ^{90}Y-ferric hydrate colloid, and ^{186}Re-sulphide colloid." Radiobiologia, Radiotherapia. Vol. 2, p. 363-370 (1979)
10. D. P. Gierga, J. C. Yanch, and R E. Shefer, "Development and construction of a neutron beam line for accelerator-based boron neutron capture synovectomy." Medical Physics. Vol. 27, p. 203-214 (2000)
11. "Current status of neutron capture therapy." International Atomic Energy Agency IAEA-TECDOC-1223. Austria, May (2001)
12. Neil A. Campbell, "The Cell." Biology, 4th Ed. edited by Don O'Neal et al., New York: Benjamin/Cummings Publishing Company, Inc. p. 108-221 (1996)
13. John F. Valliant, Personal Communication, valliant@mcmaster.ca, December (2003)
14. "Potassium dodecahydrododecaborate hydrate, min. 98%." Material Safety Data Sheet. Product No. 19-1800, CAS No. 12008-77-4, Strem Chemicals, Inc., Newburyport, MA, Revised December 15, 2003 (visit http://www.strem.com/code/index.ghc)
15. John F. Valliant et al., "The synthesis of corticosteroid-carborane esters for the treatment of rheumatoid arthritis via boron neutron capture synovectomy." Tetrahedron Letters. Vol. 41, p. 1355-1358 (2000)

16. M. L. Arnold, "Development of an accelerator based system for in-vivo neutron activation analysis measurements of manganese in humans." Ph.D. Thesis. McMaster University, Hamilton, ON, Canada (2000)
17. M. L. Arnold, F. E. McNeill, and D. R. Chettle, "The feasibility of measuring manganese concentrations in human liver using neutron activation analysis." NeuroToxicology. Vol. 20 (2-3) p. 407-412 (1999)
18. M. L. Arnold et al., "System design for in-vivo neutron activation analysis measurements of manganese in the human brain: based on Monte Carlo modeling." Applied Radiation and Isotopes. Vol. 53, p. 651-656 (2000)
19. M. L. Arnold et al., "An accelerator based system for in-vivo neutron activation analysis measurements of manganese in human hand bones." Medical Physics. Vol. 29 (11), p. 2718-2724 (2002)
20. Aslam et al., "Spectrometry and dosimetry for low energy accelerator based in-vivo measurements." Annual Report McMaster Accelerator Laboratory. McMaster University, Hamilton, ON, Canada (2001)
21. Aslam, W. V. Prestwich, and F. E. McNeill, "Thin target $^{7}Li(p,p'\gamma)^{7}Li$ inelastic gamma ray yield measurements." Journal of Radioanalytical Nuclear Chemistry. Vol. 254 (3) p. 533-544 (2002)
22. MCNP – A General Monte Carlo N-Particle Transport Code, Version 5. edited by Thomas E. Booth et al., LA-UR-03-1987, Los Alamos National Laboratory, April 24 (2003)
23. S. Giani et al., GEANT4: An object-oriented toolkit for simulation in HEP. CERN/LHCC 98-44 (1998) (visit http://cern.ch/geant4)
24. "ICRP Publication 60: 1990 Recommendations of the International Commission of Radiological Protection, 60." Annals of the ICRP Vol. 21/1-3 Elsevier (1991)
25. R. G. Butler, Personal Communication, butlerr@mcmaster.ca, January (2004)
26. J. D. Adachi, Personal Communication, St. Joseph's Hospital, 25 Charlton Ave. E., Hamilton, ON, Canada, January (2004)
27. Doug R. Boreham, Personal Communication, boreham@mcmaster.ca, January (2004)
28. "Report of the Task Group on Reference Man." International Commission on Radiological Protection No. 23. edited by W. S. Snyder et al., Toronto: Pergamon Press (1975)
29. Colin E. Webber, Personal Communication, webber@hhsc.ca, January (2004)
30. SYNBONE AG, Neugutstrasse 4, 7208 Malans, Switzerland (visit http://www.synbone.ch)
31. Douglas J. Gardner, "Polyester and Vinyl Ester Resins" @ UMaine.edu. Accessed December 12, 2003 (visit http://www.umaine.edu/adhesion/gardner/5502002/polyester%20resins.pdf)
32. S. H. Byun, "Estimation of the BF_3 long counter response using the thermal equivalent neutron flux determined by Cu activation." Personal Reference Notes, Revised May 28, 2003, soohyun@mcmaster.ca
33. T. B. Coplen, "Atomic Weights of the Elements 1999, IUPAC Technical Report." Pure and Applied Chemistry. Vol. 73 (4) p. 667-683 (2001); data taken from the National Institute for Standards and Technology, Physical Reference Data, Atomic

Weights and Compositions, February 2005, (visit http://physics.nist.gov/PhysRefData/Compositions/)
34. Evaluated Nuclear Structure Data File, National Nuclear Data Center, Brookhaven National Laboratory (visit http://www.nndc.bnl.gov/ensdf/)
35. Decay Radiation Search, National Nuclear Data Center, Brookhaven National Laboratory (visit http://www.nndc.bnl.gov/nudat2/)
36. G. Bengua et al., "Evaluation of the characteristics of boron-dose enhancer (BDE) materials for BNCT using near threshold ^{7}Li(p,n)^{7}Be direct neutrons." Physics in Medicine and Biology. Vol. 49, p. 819-831 (2004)
37. S. H. Byun et al., "Efficiency calibration and coincidence summing correction for a 4π NaI(Tl) detector array." Nuclear Instruments and Methods in Physics Research A. Vol. 535, p. 674-685 (2004)
38. S. H. Byun, Personal Communication, soohyun@mcmaster.ca, December (2003)
39. Microcal ™ Origin ® Version 6.0, Microcal Software, Inc. Northampton, MA (1999) (visit http://www.microcal.com)
40. P.R. Bevington and D.K. Robinson, Data Reduction and Error Analysis for the Physical Sciences, 2nd Ed. Toronto: McGraw-Hill, Inc. (1992)
41. Glenn F. Knoll, Radiation Detection and Measurement, 3rd Ed. Toronto: John Wiley and Sons, Inc. (2000)
42. "Operating and Maintenance Instructions." NP-1 Portable Neutron Monitor. Part No. A245890, Tracerlab, Richmond, California, September (1966)
43. Aslam, W V. Prestwich, and F. E. McNeill, "Lithium target performance evaluation for low-energy accelerator-based in vivo measurements using gamma spectroscopy." Applied Radiation Isotopes. Vol. 58, p. 321-331 (2003)
44. MCNP – A General Monte Carlo N-Particle Transport Code, Version 5. edited by Thomas E. Booth et al., LA-UR-03-1987, Los Alamos National Laboratory, April 24 (2003)
45. M. L. Arnold et al., "System design for in-vivo neutron activation analysis measurements of manganese in the human brain: based on Monte Carlo modeling." Applied Radiation and Isotopes. Vol. 53, p. 651-656 (2000)
46. W. S. Snyder et al., "Estimates of Absorbed Fractions for monoenergetic phantom sources uniformly distributed in various organs of a heterogeneous phantom." MIRD Pamphlet No. 5 Supplement 3, Journal of Nuclear Medicine. Vol. 10, p. 46-52 (1969)
47. W. Lorensen, "Marching through the visible man." Proceedings of the Visualization '95. IEEE Press, October (1995)
48. M. J. Berger, J. S. Coursey, and M. A. Zucker, "Stopping-Power and Range Tables for Electrons, Protons, and Helium Ions: Material composition data." Physical Reference Data, National Institute of Standards and Technology NISTIR 4999. April 2000 (visit http://physics.nist.gov/cgi-bin/Star/compos.pl)
49. Douglas J. Gardner, "Polyester and Vinyl Ester Resins" @ UMaine.edu. Accessed December 12, 2003 (visit http://www.umaine.edu/adhesion/gardner/5502002/polyester%20resins.pdf)

50. H. Liskien and A. Paulsen, "Neutron production cross sections and energies for the reactions ^{7}Li(p,n)^{7}Be and ^{7}Li(p,n)^{7}Be*." Atomic Data and Nuclear Tables. Vol. 15 (1), p. 57-84 (1975)
51. "Nuclear Data Tables, Part 3." Nuclear Data Tables. National Academy of Science, Washington, D.C. (1960)
52. Aslam et al., "Development of a low-energy monoenergetic neutron source for applications in low-dose radiobiological and radiochemical research." Applied Radiation and Isotopes. Vol. 58, p. 629-642 (2003)
53. Aslam et al., "Monte Carlo Simulation of Neutron Irradiation Facility Developed for Accelerator Based In-Vivo Neutron Activation Measurements in Human Hand Bones." Ph.D. Thesis, Paper 6. McMaster University, Hamilton, ON, Canada (2003)
54. C. L. Lee and X. L. Zhou, "Thick target neutron yields for the ^{7}Li(p,n)^{7}Be reaction near threshold." Nuclear Instruments and Methods in Physics Research B. Vol. 152, p. 1-11 (1999)
55. Evaluated Nuclear Structure Data File, National Nuclear Data Center, Brookhaven National Laboratory (visit http://www.nndc.bnl.gov/ensdf/)
56. F. E. McNeill, Personal Communication, fmcneill@mcmaster.ca, September (2004)
57. M. J. Berger, J. S. Coursey, and M. A. Zucker, "Stopping-Power and Range Tables for Electrons, Protons, and Helium Ions: Material composition data." Physical Reference Data, National Institute of Standards and Technology NISTIR 4999. April 2000 (visit http://physics.nist.gov/cgi-bin/Star/compos.pl)
58. Reprinted from Applied Radiation and Isotopes, Vol. 53, p. 651-656 Copyright (2000), M. L. Arnold et al., "System design for in-vivo neutron activation analysis measurements of manganese in the human brain: based on Monte Carlo modeling", with permission from Elsevier.

ELSEVIER

8 August 2005

Our Ref: HG/jj/Aug05/J140

Victor Kreft
M.Sc. Candidate, TAB 203
Department of Medical Physics
McMaster University
1280 Main St. W.
Hamilton, ON
Canada L8S 4L8

Dear Victor Kreft

APPLIED RADIATION AND ISOTOPES, Vol 53, 2000, pp 651-656, Arnold et al, figure 1

As per your letter dated 2 August 2005, we hereby grant you permission to reprint the aforementioned material at no charge **in your thesis** subject to the following conditions:

1. If any part of the material to be used (for example, figures) has appeared in our publication with credit or acknowledgement to another source, permission must also be sought from that source. If such permission is not obtained then that material may not be included in your publication/copies.

2. Suitable acknowledgment to the source must be made, either as a footnote or in a reference list at the end of your publication, as follows:

   "Reprinted from Publication title, Vol number, Author(s), Title of article, Pages No., Copyright (Year), with permission from Elsevier".

3. Reproduction of this material is confined to the purpose for which permission is hereby given.

4. This permission is granted for non-exclusive world **English** rights only. For other languages please reapply separately for each one required. Permission excludes use in an electronic form. Should you have a specific electronic project in mind please reapply for permission.

5. This includes permission for the National Library of Canada to supply single copies, on demand, of the complete thesis. Should your thesis be published commercially, please reapply for permission.

Yours sincerely

H Gainford

Helen Gainford
Rights Manager

Your future requests will be handled more quickly if you complete the online form at www.elsevier.com/wps/find/obtainpermissionform.cws_home/obtainpermissionform

Elsevier, Global Rights Department, PO Box 800, Oxford OX5 1DX, UK
Tel +44 (0)1865 843830 | Fax +44 (0)1865 853333 | www.elsevier.com
vat no. 494 6272 12